Studies of Climate Dynamics with Innovative Global-Model Simulations

Xiaoming Shi

A dissertation
submitted in partial fulfillment of the
requirements for the degree of

Doctor of Philosophy

University of Washington

2015

Reading Committee:

Dale R. Durran, Chair

John M. Wallace

Dennis L. Hartmann

Program Authorized to Offer Degree:
Atmospheric Sciences

University of Washington

Abstract

Studies of Climate Dynamics with Innovative Global-Model Simulations

Xiaoming Shi

Chair of the Supervisory Committee:
Prof. Dale R. Durran
Atmospheric Sciences

Climate simulations with different degrees of idealization are essential for the development of our understanding of the climate system. Studies in this dissertation employ carefully designed global-model simulations for the goal of gaining theoretical and conceptual insights into some problems of climate dynamics.

Firstly, global warming-induced changes in extreme precipitation are investigated using a global climate model with idealized geography. The precipitation changes over an idealized north-south mid-latitude mountain barrier at the western margin of an otherwise flat continent are studied. The intensity of the 40 most intense events on the western slopes increases by ~4 % per °C of surface warming. In contrast, the intensity of the top 40 events on the eastern mountain slopes increases at ~6 % per °C. This higher sensitivity is due to enhanced ascent during the eastern-slope events, which can be explained in terms of linear mountain-wave theory relating to global warming-induced changes in the upper-tropospheric static stability and the tropopause level.

Dominated by different dynamical factors, changes in the intensity of extreme precipitation events over plains and oceans might differ from changes over mountains. So the response of extreme precipitation over mountains and flat areas are further compared using larger data sets of simulated extreme events over the two types of surfaces. It is found that the sensitivity of extreme precipitation to increases in global mean surface temperature is 3 %

per °C lower over mountains than over the oceans or the plains. The difference in sensitivity among these regions is not due to thermodynamic effects, but rather to differences between the gravity-wave dynamics governing vertical velocities over the mountains and the cyclone dynamics governing vertical motions over the oceans and plains. The strengthening of latent heating in the storms over oceans and plains leads to stronger ascent in the warming climate.

Motivated by the fact that natural variability of the atmosphere could obscure the signal of anthropogenic warming on time scales of years to decades, the large scale variability of the atmosphere is also studied. Analysis using simulations in the Community Earth System Model Large Ensemble project reveals that the Northern Annular Mode (NAM) does not have a stable spatial pattern when 50-year long segments of data are used to calculate it. Some segments of data result in NAM-like variability with a very strong North Pacific center of action, while in some others it exhibits a more symmetric structure, with North Pacific and Euro-Atlantic centers of comparable strength. Perhaps somewhat puzzling, the NAM's North Pacific center of action is found to have a strengthening trend under anthropogenic warming.

Lastly, the large-scale character of an atmosphere in rotating Radiative-Convective Equilibrium (RCE) is studied, using a global atmospheric model with prescribed globally uniform sea surface temperature and no insolation. In such an equilibrium state, numerous tropical cyclone-like vortices develop in the extratropics, which move slowly poleward and westward. The typical spacing of simulated tropical cyclone-like vortices is comparable to the Rossby radius of deformation, while the production of available potential energy is at a scale slightly smaller than that of the vortices. It is hypothesized that the growth of tropical cyclone-like vortices is driven by the self-aggregation of convection, while baroclinic instability destabilizes any vortices that grow significantly larger than the deformation radius. A weak Hadley circulation dominates in the deep tropics, and an eastward-propagating wavenumber one MJO-like mode with a period of 30 to 40 days develops along the equator.

Table of Contents

List of Figures

Acknowledgments

First and foremost, I would like to thank my advisor, Dale Durran, who shaped my research with an artist's pursuit of perfection. Not did he only influence my work, but also my attitude to life. His happy smiles often remind me that troubles will eventually go away. I am grateful to Mike Wallace and Chris Bretherton for advising my studies on large scale dynamics of the atmosphere. Their patient guidance and deep insights have important influence on the way in which I think about science. I also thank Daehyun Kim for advising me on another very interesting paper on tropical dynamics, which is not included in this dissertation due to the limit of time. I wish to express my appreciation of Dennis Hartmann, Dargan Frierson and David Battisti who served in my committee and gave numerous constructive discussions on my work. Finally, I am deeply indebted to my wife, Ruixue Yin, who has stood by me and supported me through this long five-year journey, bringing me joy and inspiration constantly.

Dedication

to my parents, Yuliang Shi and Yufang Hao.

Chapter 1

Introduction and Overview

The first problem studied in this dissertation is the response of extreme precipitation to global warming. Considerable progress has been made in understanding the change in global mean precipitation that will occur as the climate warms. Global climate models suggest the relative humidity will remain roughly constant, implying through the Clausius-Clapeyron (CC) equation, an increase in atmospheric water vapor of about $7\,\%\,\mathrm{K}^{-1}$ of surface warming. The strength of the hydrological cycle is not, however, constrained simply by the water vapor content of the air, but by the need to balance the latent heating accompanying increased precipitation with additional long-wave radiative cooling (Allen and Ingram, 2002; Takahashi, 2009; O'Gorman et al., 2012). Global climate models suggest this energetic constraint will limit increases in global mean precipitation to roughly $2\,\%\,\mathrm{K}^{-1}$ of surface warming (Held and Soden, 2006; Liepert and Previdi, 2009).

In contrast to the global-warming-induced changes in mean precipitation predicted by climate models, extratropical precipitation extremes in climate simulations increase at about $6\,\%\mathrm{K}^{-1}$ of globally averaged surface warming. This rate of increase is close to the 'thermodynamic' sensitivity of condensation to warming, which is produced by temperature increases at fixed relative humidity when vertical motions stay almost constant (O'Gorman and Schneider, 2009a). The simulated sensitivity of tropical precipitation extremes differs substantially between climate models. Nevertheless, by applying observational constraints to climate simulations and exploiting the relationship between the simulated responses to interannual variability and climate change, O'Gorman (2012) estimated a sensitivity of the 99.9th percentile of daily tropical precipitation to climate change at $10\,\%\,\mathrm{K}^{-1}$.

The preceding large-scale averages are not necessarily representative of the high-impact changes that may occur in extreme precipitation over local regions, because of the influence of fine-scale processes, such as orographic and snow albedo effects, on climate change (Diffenbaugh et al., 2005). In Chapter 2, I investigated the response of extreme precipitation over an idealized mountain range, and examine the detailed difference between the response over its western and eastern slopes. Chapter 3 compares the differences in the response of extreme precipitation over mountains and other areas, and explains the underlying physical mechanisms. The simple idealized shapes of the mountains and the continents used in the simulations facilitates the comparison of extreme events across different latitudes, and makes the analysis of underlying dynamics easier to generalize than the results of real-world simulations.

Besides the spatial heterogeneity of the response of climate to global warming, another source of uncertainty in the projection of future climate stems from the natural variability of the atmospheric circulation. Natural variability in the atmosphere could easily obscure the signal from anthropogenic warming on timescales of a few decades and spatial scales smaller than continental (Deser et al., 2012a; Hawkins and Sutton, 2012). Deser et al. (2012b) compared individual members of a 40-member ensemble, and found that the dominant source of uncertainty in the simulated climate response at middle and high latitudes is internal atmospheric variability associated with the annular modes.

Quadrelli and Wallace (2002) showed that the observed structure of NAM is significantly different during warm and cold winters of the ENSO cycle in the historical record. The Community Earth System Model (CESM) Large Ensemble (CESM-LE) project (Kay et al., 2014) provides a unique opportunity to quantify the variability in NAM's structure under the same historical or anthropogenic warming forcings, using a much larger dataset. As will be demonstrated in Chapter 4, the NAM's centers of action and the coupling between them exhibit significant variations among the individual realizations in CESM-LE. The variations are partly a manifestation of natural variability on the multidecadal time scale and partly due to external forcings.

The last chapter describes the characteristics of an atmosphere in rotating Radiative-Convective Equilibrium (RCE). As stated by Bretherton et al. (2005), RCE in a non-rotating, horizontally homogeneous environment is a time-honored idealization for understanding the tropical atmosphere and its sensitivity to relevant forcings. Its history can be traced back to the early work by Manabe and Strickler (1964) with single column models. Modern RCE simulations employ cloud-resolving models to study a diverse array of issues, including controls on the hydrological cycle (Romps, 2011), the distribution of convective mass fluxes (Tompkins and Craig, 1998), scaling laws for moist convection (Robe and Emanuel, 1996), etc.

Recently, Held and Zhao (2008) proposed that RCE in a rotating environment as simulated using general circulation models could serve as a useful framework for studying the tropical cyclones (TCs) produced by global models, and for illuminating the influence of external parameters and model assumptions on TC simulations. The simulation documented in Chapter 5 is based on a model similar to that of Held and Zhao (2008), but on a spherical earth. Such experiments help bridge between the TCs in even more idealized simulations and real world simulations. The analysis and discussion in Chapter 5 primarily focus on the dynamical processes associated with TC-like vortices in rotating RCE. Planetary-scale features of the tropical circulation are also discussed and compared with their counterparts previous literature, so as to provide a comprehensive picture of the atmospheric motions in rotating RCE on a sphere.

Chapter 2

Response of Extreme Precipitation over Mid-latitude Mountains to Global Warming

2.1 Introduction

In contrast to the global-warming-induced changes in mean precipitation predicted by climate models, which decrease in certain regions such as the subtropics, precipitation extremes are expected to increase in almost all areas of the globe (Emori and Brown, 2005; Kharin et al., 2007). Extratropical precipitation extremes in climate simulations increase at about $6\,\%\mathrm{K}^{-1}$ of globally averaged surface warming. This rate of increase is close to the 'thermodynamic' sensitivity of condensation to warming, which is produced by temperature increases at fixed relative humidity when vertical motions stay almost constant (O'Gorman and Schneider, 2009a). The simulated sensitivity of tropical precipitation extremes differs substantially between climate models. Nevertheless, by applying observational constraints to climate simulations and exploiting the relationship between the simulated responses to interannual variability and climate change, O'Gorman (2012) estimated a sensitivity of the 99.9th percentile of daily tropical precipitation to climate change at $10\,\%\,\mathrm{K}^{-1}$.

With 26% of the world's population living within mountains or their foothills, and over 40% living in river basins originating in mountainous regions (Beniston, 2005), understanding the response of orographic precipitation extremes to global warming is important for anticipating societal impacts such as flooding and landslides (Maddox et al., 1978; Lin et al., 2001;

Rasmussen and Houze, 2012). Yet only a few previous studies have reported on warming-induced precipitation extremes over mountains as part of more widely targeted numerical simulations. These studies (Diffenbaugh et al., 2005; Singh et al., 2013; Wehner, 2013) suggest that precipitation extremes will increase in frequency and intensity over the high elevations and rain-shadowed regions of the Pacific Northwest portion of the United States.

Here I use a combination of global-climate and mesoscale-weather-forecast models, together with a linear mountain wave model, to develop a more complete physical understanding of the processes governing changes in extreme precipitation over simplified topography representative of one of the north-south mountain ranges along the west coast of North America. The mesoscale model is used to provide more detailed simulations of the response of mid-latitude orographic precipitation extremes to global warming in the different environmental parameter regimes produced by the global climate model. The changes on both the the windward (western) side of the mountains, and on their leeward (eastern) side are partitioned into the contributions from thermodynamics and from dynamics in the spirit of O'Gorman and Schneider (2009a,b). The linear mountain wave model is used to explore the physical principles governing the dynamical response.

This chapter is organized as follows. Section 2 describes the numerical models used in our idealized experiments. Section 3 documents responses of the climatological means of orographic precipitation to doubled CO_2. Section 4 examines the distribution and synoptic-scale structure of the extreme events. The relative contributions of thermodynamics and dynamics to the changes in extreme-event intensity are explored in Section 5. Section 6 examines the elevational dependence of the changes in extreme precipitation. The conclusions are presented in Section 7.

2.2 Models and methods

The numerical models used in our study are the Geophysical Fluid Dynamics Laboratory (GFDL) global HIgh Resolution Atmospheric Model (HiRAM) (Zhao et al., 2009) and the Weather Research and Forecasting (WRF) model Version 3.5.1 (Skamarock et al., 2008).

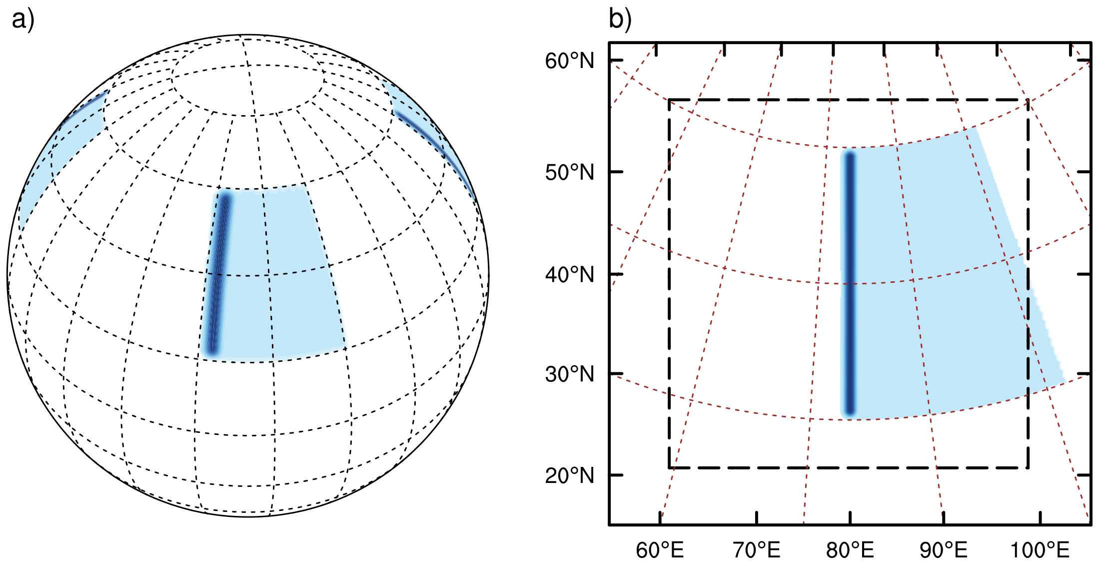

Figure 2.1: Horizontal domains for the a) HiRAM and b) WRF simulations. In both panels, the blue shaded regions represent the continents, with the mountain ridge in darker blue. The dash-line box in b) is the lateral boundary of the inner (12-km) nested domain. Cross-sections of the mountain ridge are shown in Fig. 2.10.

The HiRAM model is run at approximately 50 km horizontal resolution to effectively create a multidecadal data set for both a control and a globally warmed climate. The most extreme orographic precipitation events from this larger sample are dynamically downscaled using the WRF model at 12-km horizontal resolution.

To isolate the dynamic and thermodynamic processes governing the changes in extreme orographic precipitation, I consider an idealization of the mountainous terrain in north America, along with the drier plains to their east. Four copies of these prototypical north-American continents are distributed at 90° intervals around the northern mid-latitudes (Fig. 2.1a). The remainder of the planet is covered with a 24-m deep mixed layer ocean. The continents extend 30° east-west in longitude and span the latitude band 30°–60°N. They are flat except on their west coasts, where a single smooth mountain ridge runs north-south just inland from the coast. The surface elevation z_s of each ridge is determined by

$$z_s(x,y) = \frac{h_m}{2} \begin{cases} 1 + \cos(\pi r) \ , & \text{if } |r| < 1 \, , \\ 0 \, , & \text{otherwise} \, , \end{cases} \tag{2.1}$$

where $h_m = 2.5\,\mathrm{km}$ is the height of the ridge[1], and $r(x,y)$ is defined as:

$$r(x,y) = \begin{cases} \sqrt{\dfrac{(x-x_0)^2}{a^2}} \, , & \text{if } |y-y_0| < b-a, \\ \sqrt{\dfrac{(x-x_0)^2 + \left[|y-y_0| - (b-a)\right]^2}{a^2}} \, , & \text{otherwise;} \end{cases} \tag{2.2}$$

here a is the east-west half width of the ridge (set to 240 km in the HiRAM and 120 km in the WRF simulations); b is the north-south half width (taken as 1675 km, corresponding to 15° in latitude, in all simulations) and x_0 and y_0 are the coordinates of the center of the ridge.

HiRAM has a finite-volume dynamical core using a cubed-sphere grid topology and sophisticated physics modules for simulating processes such as in cloud microphysics, moist convection and land surface exchanges. The same model parameters and resolution ($\approx 50\,\mathrm{km}$ horizontally, 32 vertical levels) as those specified in Zhao et al. (2009) are adopted in our simulations. I run HiRAM with modern (330 ppm) and doubled (660 ppm) CO_2 concentrations and daily averaged solar insolation for 20 years, and retain 6-hourly data from the last 10 years for analysis. Since four identical continents are symmetrically distributed around a latitude circle, I treat the 10 years of global analysis data as a 40-year data set over a single continent. Our focus is precipitation on each side of the ridge on the western edge of this continent. The sensitivity of precipitation to global warming, for both time means and extremes, is defined as the percentage change in precipitation rate divided by the global-mean surface temperature increase, which is 5 K is our simulations.

To select a group of extreme events over the mountains from each simulation, I need first identify individual precipitation events and define their intensities. Different events can be

[1]This is roughly the average height of Rocky Mountains, see Fig. 2.8a.

separated based on connectivity in latitude-time plots of the zonally averaged precipitation rate over each east-west segment of grid cells ascending the western or descending the eastern slopes. The latitude-time plots are smoothed by applying a 4-point (24 h) running average in time and a 3-point (150 km) running average in latitude before measuring connectivity. Each event identified in this way corresponds to an individual weather system passing over the mountains, and its intensity is defined as the mean precipitation rate in the 24-hours and the 150-km north-south wide latitude band on the eastern or western slope receiving the most precipitation during that event. Finally, all precipitation events over the eastern and over the western mountain slopes are ranked based on their intensities, and for each side of the ridge, the top 40 events in the control and $2 \times CO_2$ simulations are selected for further analysis. Since a significant fraction of the air is diverted laterally around northern and southern ends of mountains, leading to different dynamical regimes in those regions, our analysis is restricted the segment of mountains between 32.5° and 57.5°N.

To attain a more robust evaluation of the changes in extreme events, the top 10 events in each 40-event set of HiRAM extremes are re-simulated with WRF using higher resolution and

Table 2.1: List of WRF physics schemes. Detailed descriptions of the schemes listed here are provided in Skamarock et al. (2008). Note that Singh and O'Gorman (2014) found the choice of microphysics scheme can affect the changes in precipitation extremes with warming.

Microphysics	WSM5
Longwave radiation	CAM
Shortwave radiation	CAM
Surface layer	MM5
Land surface	Noah
Planetary boundary layer	YSU
Cumulus parameterization	Kain-Fritsch

narrower mountains whose slopes better approximate average slopes in the real world. The WRF simulations also use 18 more vertical levels than in HiRAM. In the WRF simulations, a 12-km resolution domain is one-way nested in a 36-km domain, whose initial and lateral boundary conditions are provided by the HiRAM data (Fig. 2.1b). The diurnal cycle is included in the WRF simulations, with the insolation determined by the calendar date of each individual event. The HiRAM fields are computed using daily averaged solar insolation; since the boundary of the outer WRF domain is entirely over the ocean, this did not lead to any incompatibilities. A list of the WRF physics schemes used in our simulations is provided in Table 2.1. The WRF simulations run for 5-6 days centered around the time of the HiRAM event. The time, location, and intensity of the most intense 24-hour period in the fine-scale WRF run is determined in a manner similar to that for the parent HiRAM event except that the event precipitation is meridionally averaged over a 108-km (9-cell) latitude band.

Because of its higher resolution and superior microphysical parameterization, the WRF simulations provide better dynamical details of the extreme events than do HiRAM results. Nevertheless, the response of the extreme events to warming are quantitatively consistent in all major aspects in the WRF and HiRAM simulations. Unless otherwise stated, I use data from WRF simulations for the discussion about extreme events in sections 4 to 6.

2.3 Responses of climatological means

Before examining the extremes, the annual mean and seasonal mean orographic precipitation is briefly considered here, and its response to increased CO_2 in the full HiRAM dataset. For both the eastern and western slopes (halves) of the mountains, the annual and the seasonal mean precipitation are greatest over the center section of the ridge, and decrease to the north and south. Over the western slopes, the mean wintertime precipitation (December, January, February) is roughly twice that in summer (June, July, August), whereas the opposite is true over the eastern slopes.

Figure 2.2 shows the sensitivity to doubled CO_2 of the annual-, summer-, and winter-mean precipitation over the western and eastern slopes of the mountains. The annual- and

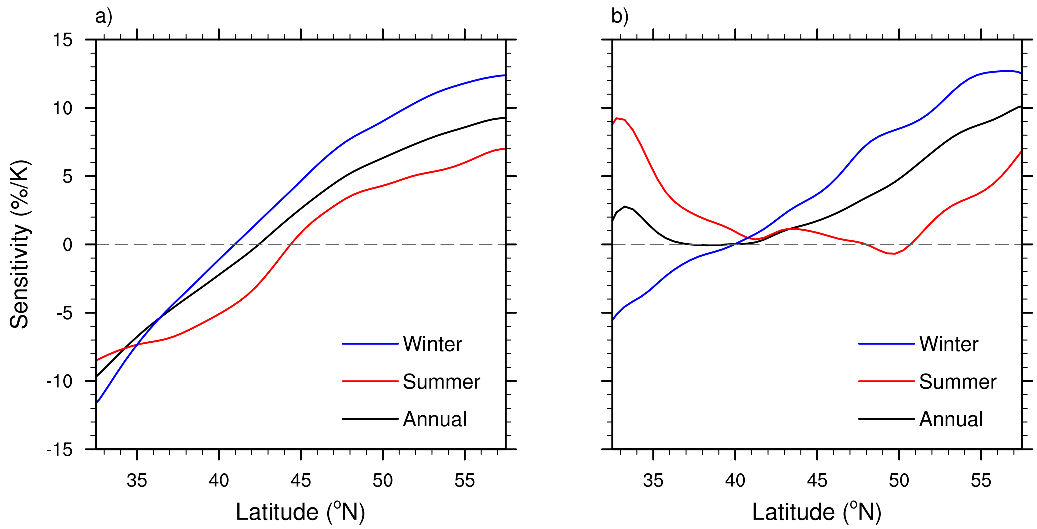

Figure 2.2: Sensitivity of annual/summer/winter mean precipitation over a) western slopes and b) eastern slopes of the mountains.

seasonal-mean western-slope precipitation sensitivities increase near the northern end of the mountains, decrease near the southern end, and vary smoothly with latitude in between (Fig. 2.2a). The wintertime western-slope sensitivities are more positive than those for the summertime and the annual mean, except near the southern end of the range. Shi and Durran (2014) conducted similar GCM simulations with annual mean insolation and a shallower slab ocean, and they found the sensitivity of western-slope orographic precipitation varies from -9 to $13\,\%\,\mathrm{K}^{-1}$ between 35 to 60°N, which is very close to the sensitivity of wintertime western-slope precipitation in our current simulations. Their analysis showed that the changes in the western-slope precipitation are produced by an almost spatially uniform thermodynamic increase due to the change in the lapse rate of saturation specific humidity and by a north-south asymmetry in dynamical changes produced by the poleward shift of storm tracks.

The sensitivity of the eastern-slope precipitation differs from that for the western-slope in that there is increasing summertime precipitation over the southern part of the mountain

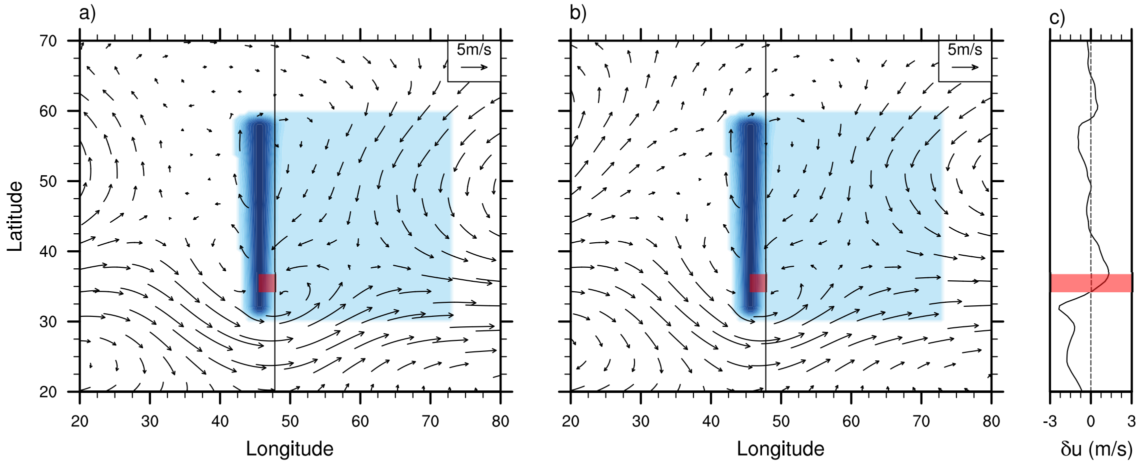

Figure 2.3: Mean summertime 850 hPa level wind fields for “significant” precipitation events in the red box (see text) in the a) control b) doubled-CO_2 climates. c) shows the change in zonal wind due to warming at the longitude indicated by vertical black lines in a) and b). Blue shaded region shows the continent, with the mountain ridge in darker blue.

despite the poleward shift of storm track. Since significant precipitation is likely associated with some sort of eddy, one might expect the eastern-slope precipitation to respond to warming in a manner similar to the summertime pattern over the western slope , because both of them are affected by the same storm track shift.

To understand why the sensitivity of the eastern-slope precipitation in summer does not have the expected north-south asymmetry, I composite the 850 hPa level wind fields for significant summer precipitation events over the eastern slope within the red square at 35°N shown in Fig. 2.3. Here ‘significant events’ are taken as those times when 6-hour precipitation rates averaged within the square are greater than 0.2 mm h^{-1}. About 9% of the total summertime period is taken up by these events, and they produce nearly 3/4 of the total summertime rainfall.

Figure 2.3 compares the composite flow pattern for significant eastern-slope summertime events in the control and doubled CO_2 simulations. Unlike wintertime, when significant eastern-slope precipitation occurs downstream of the axis of an open trough, significant summertime precipitation events occur when a small low to the south produces easterly upslope flow into the target area. This easterly upslope flow at 35°N is weaker in the doubled CO_2 composite. As a consequence, the thermodynamic tendency toward increased precipitation is almost canceled by weaker dynamical forcing, and the net sensitivity *per significant event* only increases by 0.8%/K. The actual increase in significant event precipitation is primarily due to a 3.3%/K increase in the frequency of these events, which results from the weakening of climatological mean westerlies as the storm track shift poleward. The remainder of the weaker summertime events behave in a similar way, with the sensitivities produced by changes in frequency and intensity for all events adding up to give a total sensitivity of about 6%/K at 35°N. In contrast the frequency of significant eastern-slope wintertime events is reduced by -5.8%/K, consistent with a northward shift in storminess. This reduction is a major factor, but not the only contributor to the net climatological decrease of about -3%/K in the wintertime precipitation over the eastern slope in the south.

2.4 Distribution and synoptic structure of the extreme events

I now return the focus to extreme events, beginning with the four sets of top 40 events (western side, eastern side, control and doubled CO_2) from the HiRAM simulations.

2.4.1 Location and frequency

The north-south distribution of 40 most extreme (99.75 percentile) west-side and east-side events from the HiRAM simulation are shown in Fig. 2.4, in which the latitude of the row of grid cells along the mountain slope receiving the maximum 24-hour precipitation is binned in 2.5°-wide latitude bands along the length of the topography. Extreme events occur most frequently over the central part of the mountain range.

The mean latitude at which the western-slope extremes occur shifts northward by 0.9° in the doubled CO_2 simulation, while the mean latitude for the eastern-slope extremes shifts southward by 1.1°. The northward shift in the western slope events might be linked to the

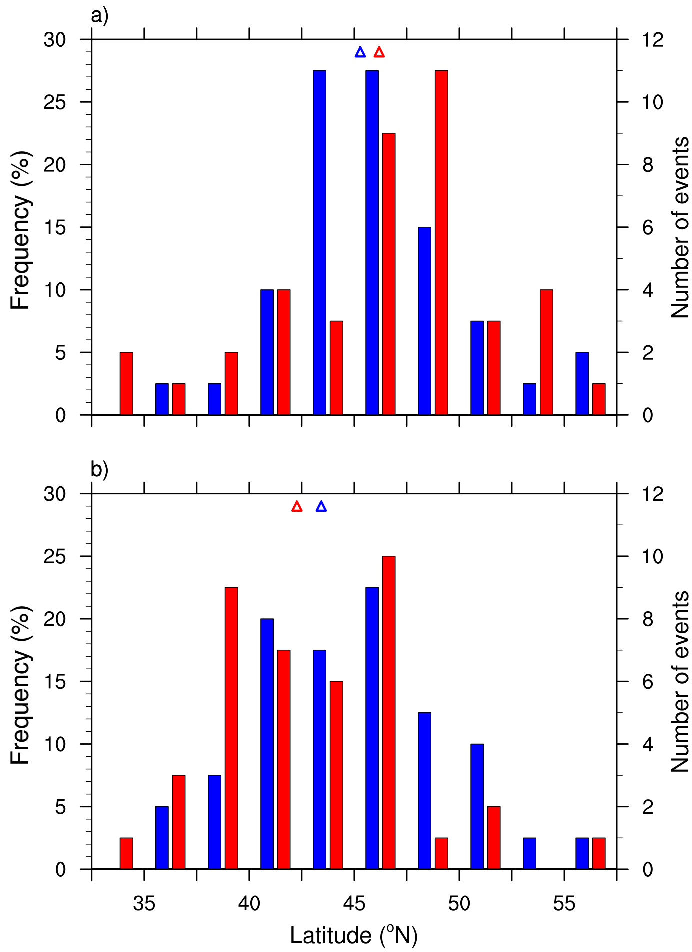

Figure 2.4: Histograms of top 40 extreme events in HiRAM simulations on the a) western and b) eastern slopes as functions of latitude in the control (blue bars) and 2 $\times$ CO_2 (red bars) simulations. Blue and red triangles indicate the mean latitudes of extreme events in the control and 2 $\times$ CO_2 climates, respectively.

northward shift in the storm track in the warmer world (Yin, 2005). Nevertheless, with only 40 events in our sample, the north-south distribution of these events is noisy. Applying the Kolmogorov-Smirnov test (Miller, 1956; Marsaglia et al., 2003) to a null hypothesis that the latitudinal distribution of extremes shown in Fig. 2.4 does not change in the warmer climate, I found the hypothesis of no change could not be rejected at the 5% significance level.

Table 2.2: Thresholds of 24-hour accumulated precipitation (mm) that select the 10 and the 40 most extreme events in the HiRAM control simulation over the western and eastern slopes. Also listed are the number of events in the $2 \times CO_2$ simulation that exceed those threshold values.

	Western		Eastern	
	Control	$2 \times CO_2$	Control	$2 \times CO_2$
Threshold	105.1 mm		70.6 mm	
# of events	40	128	40	116
Threshold	124.8 mm		86.4 mm	
# of events	10	42	10	47

The precipitation thresholds that distinguish the 10 and the 40 most extreme events in the control climate are exceeded far more frequently in the doubled CO_2 simulation. Table 2.2 shows that on both the western and eastern slopes, the number of events that exceed the control-climate 40-event threshold increases by about a factor of 3 in the doubled CO_2 simulations. For just those events above the top-10 threshold, the increase in the warmer climate is more than a factor of 4.

2.4.2 Synoptic-scale structure

Western-slope and eastern-slope precipitation extremes tend to occur at different times in a year. As shown in Fig. 2.5, western-slope extremes mostly occur in winter months, whereas eastern-slope extremes are more likely to occur in the warm season. Fig. 2.6 shows snapshots of Water Vapor Path (WVP, the column integrated water vapor) and geopotential height at 500 hPa in a western-slope and an eastern-slope event. Though they are from individual cases, the synoptic patterns in Fig. 2.6 are very typical of the most extreme events in both the control and doubled-CO_2 climates. Unless specified otherwise, the data for this and the subsequent discussions are taken from the sets of top-ten events simulated with the WRF

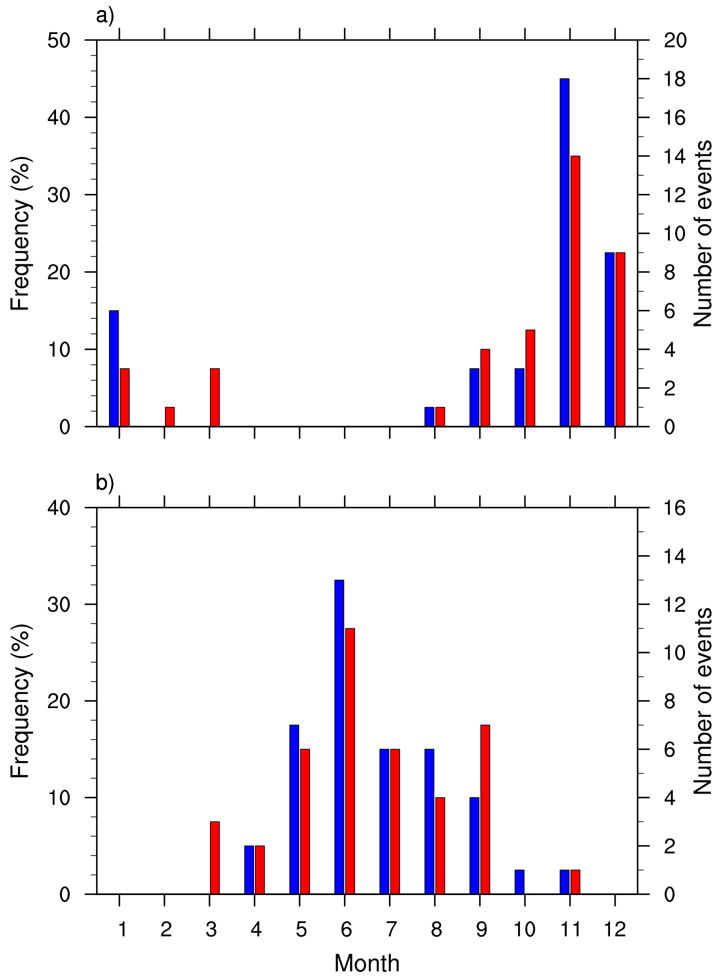

Figure 2.5: Histograms of top 40 extreme events in HiRAM simulations on the a) western and b) eastern slopes as functions of *calendar month* in the control (blue bars) and $2 \times CO_2$ (red bars) simulations.

model on the 12-km fine mesh.

The western-slope extreme event is produced by a so-called "atmospheric river," a narrow filament of concentrated moisture carried poleward from the sub-tropics (Zhu and Newell, 1994). Recent studies based on observational data from Western Europe and along the West Coast of the United States, show atmospheric rivers are often responsible for heavy and

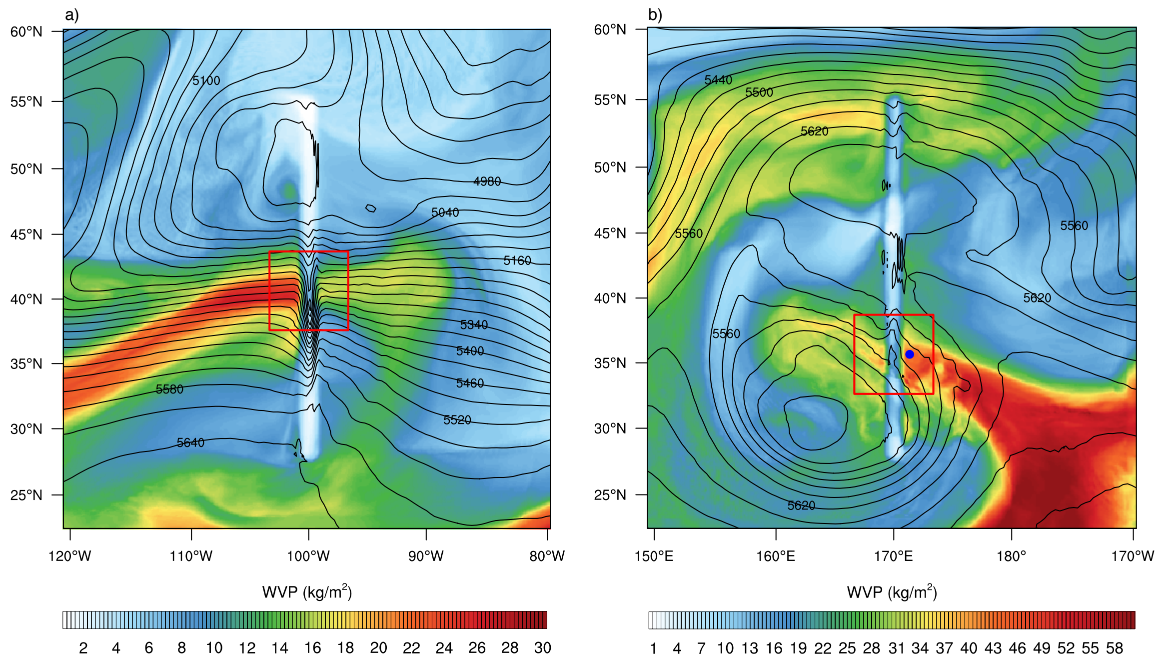

Figure 2.6: Snapshots of WVP and 500 hPa geopotential height (black contours) in a) one western-slope extreme event and b) one eastern-slope extreme event. The interval between geopotential height contours is 30 m. a) is an event in the control climate, and b) is an event in the $2 \times CO_2$ world. Red boxes indicate the north-south extent of the mountainous region receiving intense rainfall. The mountain coincides with the north-south zone of reduced WVP in the center of each panel.

extreme precipitation (Ralph et al., 2006; Warner et al., 2012; Lavers et al., 2012; Lavers and Villarini, 2013). As apparent in Fig. 2.6a, the axis of the atmospheric river is nearly perpendicular to the mountain, and it coincides with a jet of strong cross-mountain flow as evident from the strong gradient in the geopotential height field. Strong orographic lifting condenses large amounts of water vapor that precipitates out over the mountain. The contrast between the atmospheric river's WVP to east and west of the mountain clearly shows this drying.

The eastern-slope extreme event in Fig. 2.6b is caused by a cut-off low to the southwest

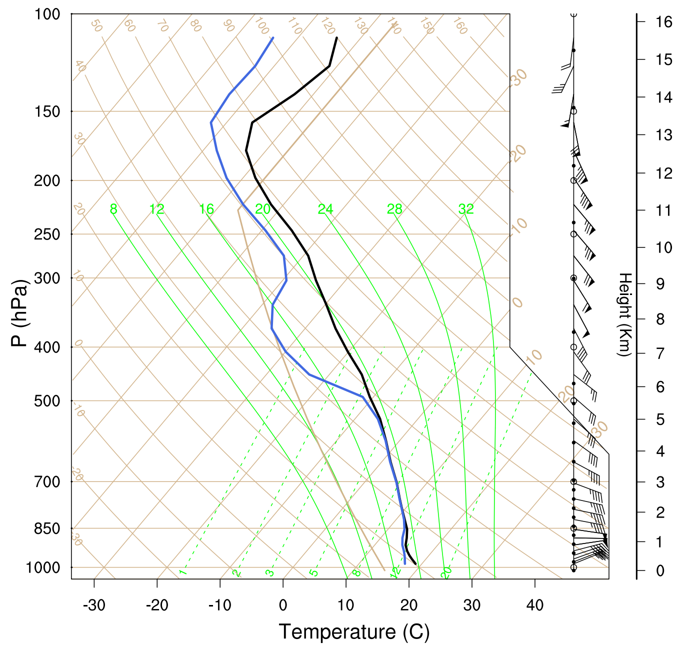

Figure 2.7: The sounding and winds in an extreme event plotted on a Skew-T Log-P chart. The sounding is taken at a location upstream of the mountain, indicated by the blue dot within the red box in Fig. 2.6b. It is at the same simulation time as Fig. 2.6b. The black curve is temperature and the blue is dew point temperature.

of the precipitation site, which produces strong southeasterlies over the eastern slope of the mountain. A plume of concentrated moisture is embedded in the southeasterly flow. A very high-amplitude ridge keeps the main jet stream well to the north of the cut-off low. Fig. 2.7 shows a sounding from the location of the blue dot in Fig. 2.6b, upstream of the eastern slope. The atmosphere between 850 and 500 hPa is completely saturated and nearly moist neutral; the upslope easterly winds in this layer are roughly 18 m s^{-1} (35 kn).

While flow patterns like that shown in Fig. 2.6b are less common in the real world than western-slope atmospheric river events, close atmospheric analogs do occasionally occur. For example, the record-breaking rainfall across the Colorado Front Range between September 11th and 13th in 2013 (Schwartz, 2014) occurred in a synoptic setting resembling that in

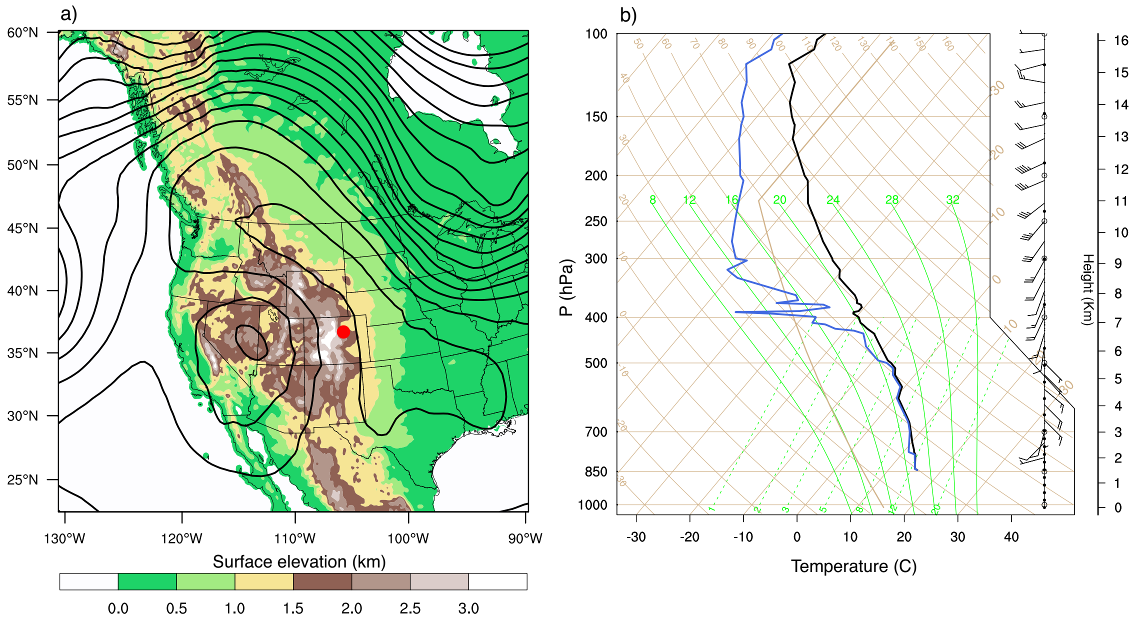

Figure 2.8: a) 500 hPa level geopotential (height contoured at 30 m intervals) for 1200 UTC 12 September 2013 and b) the sounding from Denver in Colorado at the same time. Red dot in a) indicates the geographic location of Denver. Data of a) is from the National Centers for Environmental Prediction (NCEP) FNL Operational Global Analysis.

Fig. 2.6b. The basic structure of the geopotential height field for the Colorado event, shown in Fig. 2.8a is similar to that in Fig. 2.6b, with a cut-off low south of a high-amplitude ridge. The 1200 UTC sounding from Denver, CO on 12 September 2013 (Fig. 2.8b) also shows a similar deep layer of saturated, neutrally stratified flow, although the easterly winds in that layer are somewhat weaker than those in Fig. 2.7.

2.5 Changes in extreme-event intensity

Perhaps surprisingly, the mean sensitivity of the precipitation in the top 10 events to global warming is about $2\,\%\mathrm{K}^{-1}$ higher on the eastern side (where it is $5.9\,\%\mathrm{K}^{-1}$) than on the west side (where it is 4.2 $\%\mathrm{K}^{-1}$).[2] These values are comparable to the sensitivities for the vertically integrated condensation rate in the air columns at the same time and location of each of the extreme events, which are 6.5 $\%\mathrm{K}^{-1}$ and 4.7 $\%\mathrm{K}^{-1}$ for the eastern and western sides, respectively.

The differences between the sensitivities in precipitation and condensation are due to changes in the precipitation efficiency, defined as the event-integrated precipitation divided by the event-integrated condensation. The precipitation efficiencies in these extreme events over our 120-km half-width mountains are relatively high, ranging from an average of 0.82 for the 10-western slope events in the doubled-CO_2 climate to 0.96 over the eastern slope in the control climate. These precipitation efficiencies are likely high because of the broad width of our mountains and to the absence of embedded convection (Cannon et al., 2011). On both sides of the mountain, the precipitation efficiency decreases modestly as the planet warms; the sensitivities of precipitation efficiency being $-0.7\,\%\mathrm{K}^{-1}$ and $-0.4\,\%\mathrm{K}^{-1}$ over the eastern and western sides, respectively. These sensitivities are qualitatively consistent with the findings in Kirshbaum and Smith (2008) that precipitation efficiency decreases with increases in the local temperature upstream of idealized horizontally-uniform moist flow over a three-dimensional ridge.

2.5.1 Partitioning the sensitivities into thermodynamic and dynamic contributions

In our simulations, the sensitivity of the precipitation to changes in global mean temperature are dominated by the sensitivity of the event-integrated condensation. I therefore focus further analysis on those factors responsible for the changes in condensation, separating the effects of thermodynamic and dynamical changes in the condensation during those events. The local condensation rate c in the extreme precipitation events may be estimated by assuming moist adiabatic lifting maintains the water vapor content of the rising air at

[2] Top 40 events from the HiRAM simulations show similar sensitivities: 6.3 $\%\mathrm{K}^{-1}$ over the eastern slopes and 3.9 $\%\mathrm{K}^{-1}$ in the west.

saturation, i.e.

$$c = -w\frac{dq_s}{dz} = w\gamma_s\,, \tag{2.3}$$

where w is vertical velocity, q_s is saturation specific humidity, and $\gamma_s = -dq_s/dz$ is the lapse rate of saturation specific humidity[3]. Over 95% of the precipitation in the extreme orographic precipitation events in the 12-km WRF simulations is produced by grid-resolved physical processes; the remainder (less than 5%) is from parameterized convection. Thus (2.3) can be applied directly to the archived model data to approximate the condensation rate in each saturated grid cell. Integrating (2.3) vertically, one gets the total condensation in an air column,

$$C = \sum_k s_k\, c_k, \tag{2.4}$$

where the summation is limited to saturated grid cells by defining

$$s_k = \begin{cases} 0 & \text{if unsaturated,} \\ \Delta p_k/g & \text{otherwise,} \end{cases} \tag{2.5}$$

here Δp_k is the pressure thickness of layer k and g is the gravitational constant. One can further average C over time and area for each extreme event (the 24 hours and the 108×108-km square on the mountain slope receiving most precipitation—denoted by a overbar), and then average results of the 10 events in either the control or the doubled-CO_2 climate (denoted by angle brackets) to obtain the mean condensation rate for the extremes

$$\langle\overline{C}\rangle = \langle\overline{\sum_k s_k c_k}\rangle. \tag{2.6}$$

Letting subscripts 'w' and 'c' denote the doubled-CO_2 and control climates, the change in mean condensation due to warming is

$$\delta\langle\overline{C}\rangle = \langle\overline{C}\rangle_{\mathrm{w}} - \langle\overline{C}\rangle_{\mathrm{c}} \tag{2.7}$$

[3] An analytic expression for γ_s as a function of temperature and pressure is provided in Shi and Durran (2014)

If one could pair the precipitating columns in a control climate event with the columns in a warmed climate event so that each pair of columns have the same saturated levels and the same time and space distribution, one could separate $\delta\langle\overline{C}\rangle$ into two contributions

$$\begin{aligned}\langle\overline{\sum_k s_k[(c_k)_{\mathrm{w}} - (c_k)_{\mathrm{c}}]}\rangle &= \langle\overline{\sum_k s_k \delta(w\gamma_s)_k}\rangle \\ &\approx \sum_k s_k \left[\overline{(w\delta\gamma_s)_k} + \overline{(\gamma_s \delta w)_k}\right],\end{aligned} \tag{2.8}$$

where δ again denotes the change between warm- and control-climate values. In (2.8), the terms involving $w\delta\gamma_s$ and $\gamma_s\delta w$ would estimate the contributions from thermodynamical and dynamical changes, respectively. Such pairing is, however, not possible because the number of saturated layers is typically greater in the warmer climate.

Nevertheless, I can still estimate the two terms on the right side of (2.8) as follows. The thermodynamic contribution is evaluated as

$$\delta\langle\overline{C}\rangle_{\mathrm{thrm}} = \frac{\sum_k \overline{(s_k w_k)}_{\mathrm{w}} \delta\langle\overline{\gamma_s}\rangle_k + \sum_k \overline{(s_k w_k)}_{\mathrm{c}} \delta\langle\overline{\gamma_s}\rangle_k}{2}. \tag{2.9}$$

During these extreme events, the lapse rate of saturation specific humidity varies with height, but is almost uniform in the horizontal over each 108×108-km square and 24 hour period, so its change is well captured by $\delta\langle\overline{\gamma_s}\rangle_k$. The same is not true for the vertical velocity, which varies systematically in the cross mountain direction and also exhibits substantial fluctuations in the along-slope direction. Within each 108 km north-south strip, the extreme precipitation is dominated by the cells with the strongest vertical velocities. Therefore, in estimating the dynamic contribution to (2.8), the simple time and space average used to obtain $\delta\langle\overline{\gamma_s}\rangle_k$ is replaced by $\delta\langle\tilde{w}_i\rangle_k$, where i indexes the cells in the cross-ridge direction, and for any given i, $\tilde{w}_i$ denotes the time average of the maximum w in the along-ridge direction. The dynamic contribution is then computed as

$$\delta\langle\overline{C}\rangle_{\mathrm{dyn}} = \frac{\sum_{i,k} \overline{(s_{i,k}\gamma_{s_{i,k}})}^{y,t}_{\mathrm{w}} \delta\langle\tilde{w}_i\rangle_k + \sum_{i,k} \overline{(s_{i,k}\gamma_{s_{i,k}})}^{y,t}_{\mathrm{c}} \delta\langle\tilde{w}_i\rangle_k}{2N_i}, \tag{2.10}$$

where $N_i = 9$ is the number of cells in the east-west direction included in the event average, and the y, t notation at the end of the overbar denotes event averages taken in the 108 km north-south direction and over the 24-hour time period.

Over the eastern slopes, $\delta\langle\overline{C}\rangle_{\text{thrm}}/\langle\overline{C}\rangle_c = 3.9\,\%\,\text{K}^{-1}$, $\delta\langle\overline{C}\rangle_{\text{dyn}}/\langle\overline{C}\rangle_c = 3.2\,\%\,\text{K}^{-1}$, and their sum provides a good approximation to the true value of $\delta\langle\overline{C}\rangle/\langle\overline{C}\rangle_c = 6.5\,\%\,\text{K}^{-1}$ (exceeding it by 9%). Over the western slope the same thermodynamic and dynamic sensitivities are $5.0\,\%\,\text{K}^{-1}$ and $0.03\,\%\,\text{K}^{-1}$, whose sum differs from the total sensitivity $4.7\,\%\,\text{K}^{-1}$ by just 6%. The thermodynamic sensitivity is somewhat stronger over the western slopes of the mountains than over the eastern slopes, which might be expected because most western-slope extreme events occur during winter while the eastern-slope extremes are mostly summertime phenomena, and $\partial(\ln\gamma_s)/\partial T$ is larger at colder temperatures (Shi and Durran, 2014; Siler and Roe, 2014).

By far the largest east-west contrast in sensitivities is in the dynamical contribution. The large eastern-slope dynamic sensitivity more than compensates for its weaker thermodynamic sensitivity and is responsible for the eastern side having a much larger value of $\delta\langle\overline{C}\rangle/\langle\overline{C}\rangle_c$ than the western side. A closer look at this dynamical enhancement is provided in the next section.

2.5.2 Source of the dynamical enhancement

The dynamical contribution to the changes in extreme events arises from the differences between $\tilde{w}_i$ in the control and warmer climates. These differences are illustrated by the vertical profiles of $\tilde{w}_i$ in Fig. 2.9 for three different cross-ridge locations above the eastern and the western slopes. Consistent with the negligible value of $\delta\langle\overline{C}\rangle_{\text{dyn}}/\langle\overline{C}\rangle$ over the western slopes, Fig. 2.9a-c shows almost no change in the vertical velocity profiles between the control and the warmer climates. In contrast, on the eastern side, $\tilde{w}_i$ increases significantly as the climate warms at the lower and mid-slope elevations (Fig. 2.9d,e).

The vertical motions in extreme precipitation events over mountains are governed by mountain wave dynamics, as illustrated by the vertical-velocity cross-sections passing through the updraft cores for four representative events plotted in Fig. 2.10. In these moist events,

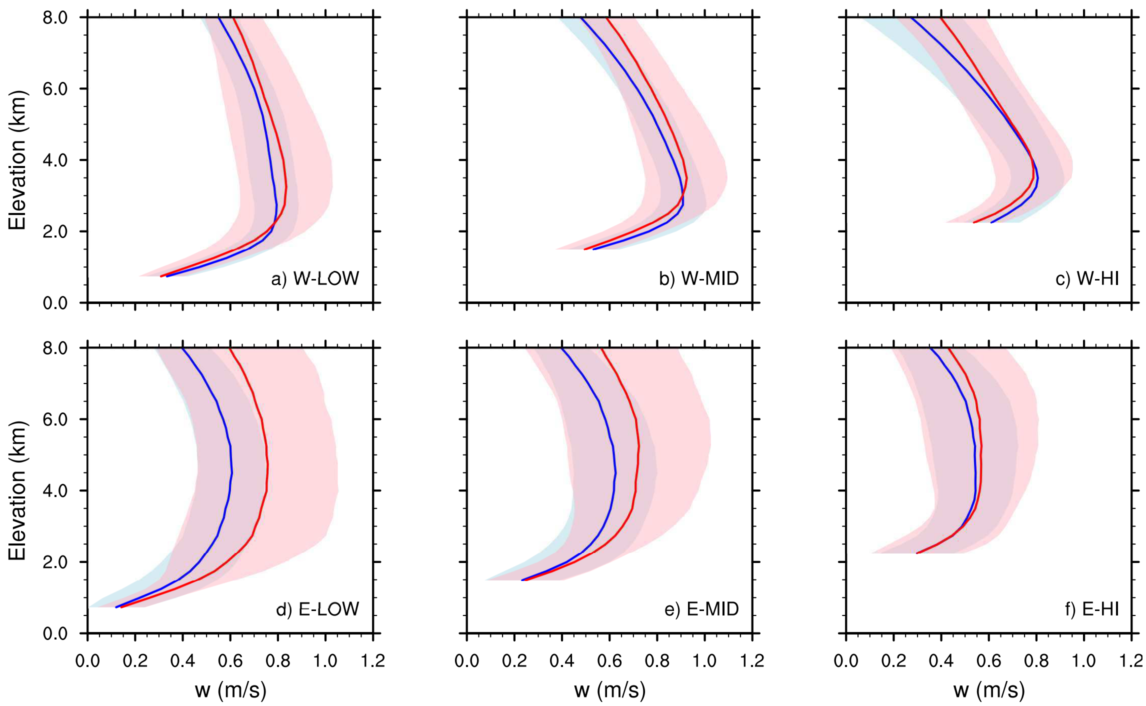

Figure 2.9: Profiles of mean $\tilde{w}_i$ over the western (upper row, a–c) and eastern slopes (lower row, d–f). The left, middle, right columns of panels show $\tilde{w}_i$ over low (LOW; 0.75 km), middle (MID; 1.5 km), high (HI; 2.25 km) surface elevations of the mountains, respectively. Blue curves are profiles in the control climate, and red curves are profiles in the $2 \times CO_2$ climate. Event scatter in the control and $2 \times CO_2$ climate is shown by light blue and light pink shading, using one standard deviation of $\tilde{w}_i$ in each ten-event set.

the effective stability in the middle and lower troposphere is weak, so the vertical wavelength of the waves is long and the axes of their updrafts and downdrafts extend almost straight upward to a height around 7 km. The upstream tilt with height of the phase lines in these waves is more pronounced in the stratosphere and upper troposphere. As indicated by the green contours, most of the condensation responsible for the precipitation extremes occurs at low levels in the updrafts above windward slopes.

The depth and intensity of this windward ascent depends on the propagation and re-

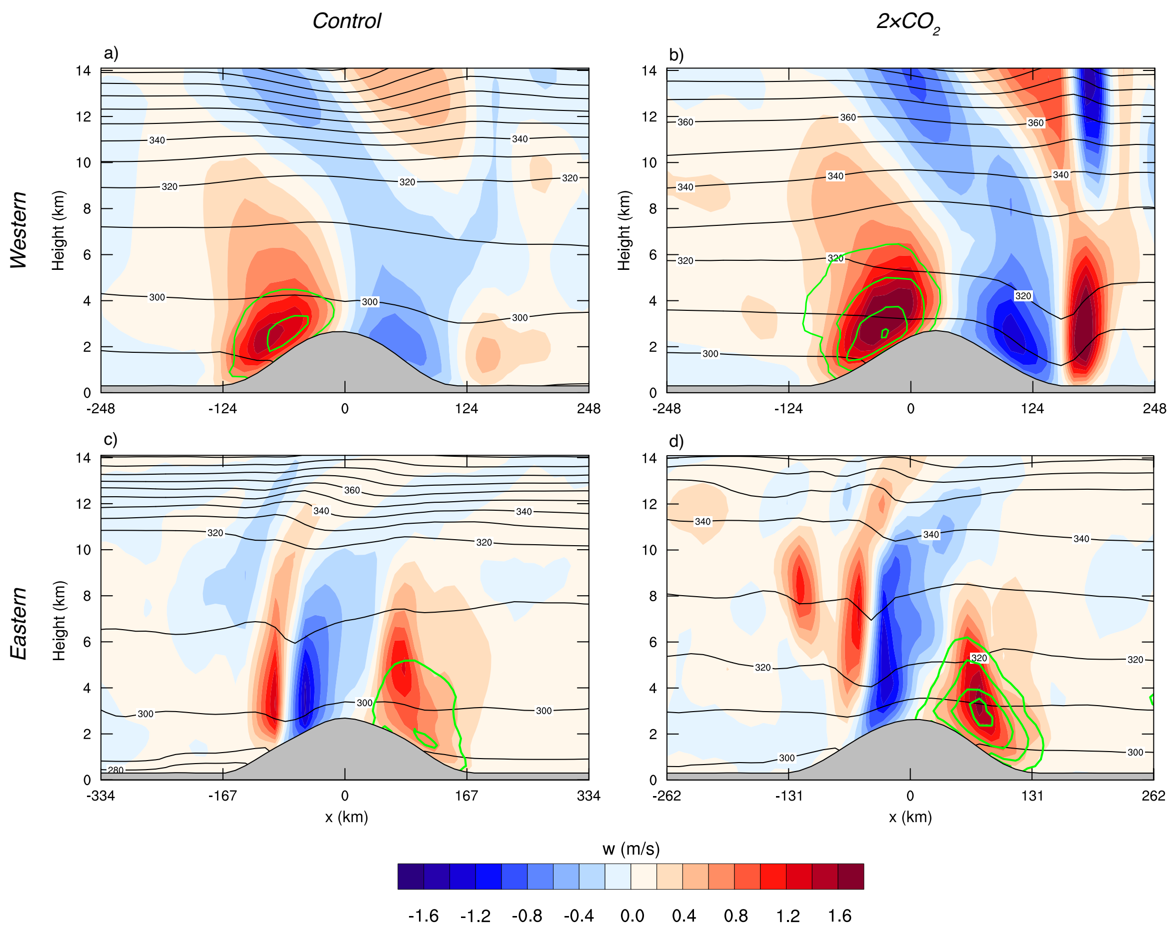

Figure 2.10: Snapshots of vertical velocity (color shading) and potential temperature (black contours) field on cross-sections through the centers of precipitation maxima over the western slopes (upper row) and the eastern slopes (lower row). a) and c) are for extreme events in the control climate. b) and d) are for the $2 \times CO_2$ climate. Also shown in green are contours of the condensation rate at intervals of 2, 4, 6 and 8 g kg^{-1} h^{-1}. These cross-sections are taken parallel to the mean wind direction in the lower troposphere. For a) and b), the winds are nearly from due west, and for c) and d), the winds are from the southwest.

flection of mountain waves. In particular, Siler and Durran (2015), using linear theory and numerical simulations, showed that the partial reflection of mountain waves at the tropopause can have an important impact on the vertical motions over mountains and the resulting precipitation. Here I compare the lower-tropospheric vertical velocities forced by the mean background atmospheric structures during the extreme events in the control and warmer climates. I compute these velocities using the linear hydrostatic mountain-wave model of Klemp and Lilly (1975), which assumes the atmosphere is incompressible and consists of three layers with constant static stabilities N and constant wind shear in each layer.

For the eastern-slope means, I neglect the vertical variations of the winds with height, which is a reasonable approximation to the actual average upstream flow. Those relatively uniform easterly winds extend up through troposphere until finally encountering a critical level (where the cross-mountain easterlies drop to zero) in the lower stratosphere.[4] In the context of the linear model, wave absorption at the critical level is represented by an upper boundary condition requiring all wave energy propagation be upward.

Assuming a vertically uniform mean cross-mountain wind U, the steady-state two-dimensional solution in the lowest layer for a single Fourier component $w_L = \Re\{\hat{w}_1(z)e^{ikx}\}$ is

$$\hat{w}_1 = ikUh_m \left[\cos\left(\frac{N_1}{U}z\right) + \alpha \sin\left(\frac{N_1}{U}z\right)\right], \tag{2.11}$$

where

$$\alpha = \frac{N_1 \sin\phi_1 + N_2\beta\cos\phi_1}{N_1\cos\phi_1 - N_2\beta\sin\phi_1}, \; \beta = \frac{N_2\sin\phi_2 + iN_3\cos\phi_2}{N_2\cos\phi_2 - iN_3\sin\phi_2},$$

and

$$\phi_j = \frac{N_j}{U}(z_j - z_{j-1}) \quad (j = 1, 2).$$

The subscripts in the above expressions denote the respective layers; h_m is the mountain height (2.5 km); z_j is the elevation of the top of layer j, and $z_0 = 0$. The solution for a single wave number k that matches the mountain width ($2a = 240\,\mathrm{km}$) in our WRF simulations is considered, though the solution for a particular mountain shape can be readily constructed using Fourier transforms.

During extreme precipitation events the atmosphere has a three-layer structure formed by a saturated and moist nearly neutral lower troposphere, topped by the dry upper troposphere

[4] As an example, see the winds for one specific event in Fig. 2.7.

and the stratosphere, with the stratosphere having the largest stability. The air in the lowest layer may become unsaturated on the lee side of mountains due to descent, but previous studies suggest that despite the presence of such unsaturated regions, the effective bulk static stability of the lowest layer N_1 is very close to the moist Brunt-Väisälä frequency (Jiang, 2003; Siler and Durran, 2015). In addition, for our specific application, there was little sensitivity to doubling or halving N_1.

Following Durran (1992), who suggested the linear tropopause tuning criteria of Klemp and Lilly (1975) works best when adjusted for finite-amplitude mountains by setting z_2 equal to the actual tropopause height minus $3h_m/2$, in the control and warmer climates, z_2 is specified as 8.0 and 8.5 km, respectively. The mean upper tropospheric moist static stability gives N_2^2 as 0.94×10^{-4} and 1.15×10^{-4} s^{-2} in the control and warmer climates. Increases in mid-latitude static stability are a robust response to global warming in climate simulations (Frierson, 2006), and the rise in tropopause height due to CO_2 increases has been seen in both observations and climate model simulations (Kushner et al., 2001; Santer et al., 2003). The depth of the saturated layer is well approximated as $z_1 = z_2 - 5$ km. The other parameters required to evaluate (2.11) remain almost the same in the control and warmer climates; we estimate these values as $N_1^2 = 2.5 \times 10^{-5}\,\mathrm{s}^{-2}$, $N_3^2 = 4.0 \times 10^{-4}\,\mathrm{s}^{-2}$ and $U = 15\,\mathrm{m\,s}^{-1}$.

Although the warming-induced increase in z_1 is comparable to that for z_2, the windward ascent in the three-layer model turns out to be insensitive to that change over the parameter regime of interest. Figure 2.11 shows the dependence of w_L at 1.5 km above the center of the windward slope (near the region of maximum orographic condensation) on the other two key parameters, z_2 and N_2. The extreme-event mean values for the control and the warmer climate are indicated by the green and red dots, respectively. Despite its limited dynamics, the linear model provides a good estimate of the mean vertical velocity over the eastern slope (compare Fig. 2.9e and Fig. 2.11b). Moreover, the $2.3\,\%\,\mathrm{K}^{-1}$ sensitivity of $\delta w_L/w_L$ reasonably approximates the $2.8\,\%\,\mathrm{K}^{-1}$ sensitivity of then extreme-event averaged vertical velocity $\delta\tilde{w}/\tilde{w}$ at the same 1.5 km level above the center of the windward slope.

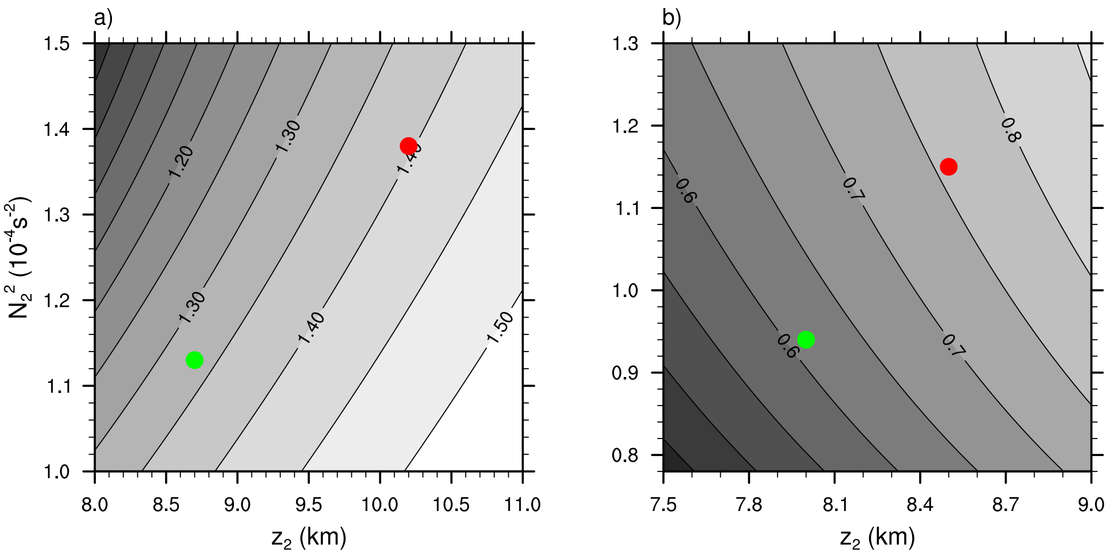

Figure 2.11: Vertical velocities w_L in linear mountain waves a at height 1.5 km above the middle point of a) the western and b) the eastern slope as a function of tropopause height z_2 and the static stability of upper troposphere N_2. Green and red dots indicate the extreme-event mean values in the control and doubled-CO_2 simulations respectively. Contour interval is $0.05\,\mathrm{m\,s^{-1}}$,

Therefore, the enhanced vertical motion in eastern-slope extreme events occurs because the atmosphere has become better tuned to produce strong mountain waves. One may ask why the western-slope extreme events do not have significant dynamical enhancement. The answer is that the background wind speeds during western-slope events make it much more difficult to produce a similar degree of mountain-wave enhancement. The changes in tropopause height and upper tropospheric static stability for the western-slope events are actually somewhat larger than those for the eastern-slope cases. As the climate warms, z_2 increases from 8.7 to 10.2 km, and N_2 increases from 1.13×10^{-4} and 1.38×10^{-4} s^{-2}. The sensitivity of w_L to these changes is, nevertheless, much reduced because the cross-mountain winds are much stronger during the western-slope events. The average extreme-event winds are a roughly uniform $15\,\mathrm{m\,s^{-1}}$ in the east, whereas they range from about $20\,\mathrm{m\,s^{-1}}$ at the top of boundary layer to $60\,\mathrm{m\,s^{-1}}$ near the tropopause in the west. Fig. 2.11a shows how this change in the upstream winds modifies the changes in w_L. The computation in Fig. 2.11a uses the full Klemp and Lilly (1975) linear model including shear such that the winds vary linearly from 20 to 60 m s^{-1} between the ground and the tropopause. The vertical velocities in Fig. 2.11a are roughly 50% larger than the average values for a point 1.5 km above the surface in Fig. 2.9b, presumably due to the simplified dynamics in the linear model (neglect of finite-amplitude and three-dimensional effects, no boundary layer or moisture). Nevertheless, they both exhibit almost negligible sensitivities to warming ($\delta w_L/w_L = 0.01\,\%\,\mathrm{K^{-1}}$, $\delta\tilde{w}/\tilde{w} = -0.05\,\%\,\mathrm{K^{-1}}$).

2.6 Elevational dependence

Extreme orographic precipitation and its sensitivity to global warming both vary with elevation. The fraction of precipitation that falls as snow and its vertical distribution can have a major impact on runoff and flooding (Hamlet and Lettenmaier, 2007). For example, hydrological model forecasts for several California watersheds suggest that a 660 m increase in the elevation of the melting level can triple the runoff during 24-hour rainfall events (White et al., 2002).

As shown by the black curves in Fig. 2.12, the 24-hour extreme-event-averaged precipitation rate P in the control climate increases with elevation until about $0.8h_m$ (a height of 2 km), and the elevation dependence is more pronounced over the western slopes than in the east. Also plotted in Fig. 2.12 are the column-integrated individual terms in the surface precipitation budget: the condensation rate C, the horizontal flux convergence of rain and snow $Q_{\mathrm{r/s}}$, and the convergence of cloud water and cloud ice $Q_{\mathrm{w/i}}$. When integrated over a 24-hour period, the sources and sinks of the hydrometeors in a column extending from the Earth's surface to the top of the atmosphere should balance such that

$$P = C + Q_{\mathrm{w/i}} + Q_{\mathrm{r/s}}. \tag{2.12}$$

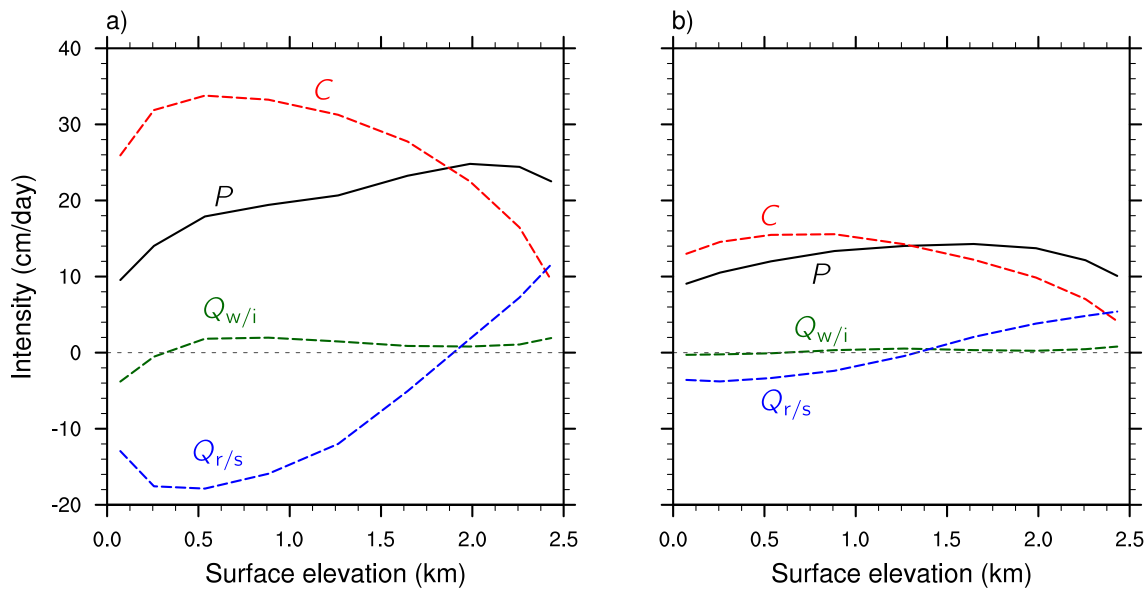

Figure 2.12: The 24-hour mean intensity of surface precipitation (P), column integrated condensation (C), column integrated convergence of rain and snow ($Q_{\mathrm{r/s}}$) and of cloud water and ice ($Q_{\mathrm{w/i}}$) in the control climate a) western-slope extreme events and b) eastern-slope extreme events. Negative values indicate divergence.

In contrast to the precipitation, as shown in Fig. 2.12, the column integrated condensation is maximized over the lower part of the mountain and decreases as the surface elevation rises. The difference between P and C is almost completely accounted for by $Q_{\mathrm{r/s}}$ due to the variations in the downwind transport of rain drops and snow . The magnitude and variation in $Q_{\mathrm{r/s}}$ is greater over the western slopes than in the east because, in the west, more extreme precipitation events occur in wintertime when the upslope westerlies are stronger and there are more slowly falling snow particles available for advection. In contrast to C and $Q_{\mathrm{r/s}}$, $Q_{\mathrm{w/i}}$ makes only a small contribution to the precipitation budget.

Neglecting the small contribution from $Q_{\mathrm{w/i}}$, (2.12), the sensitivity of the mean column-

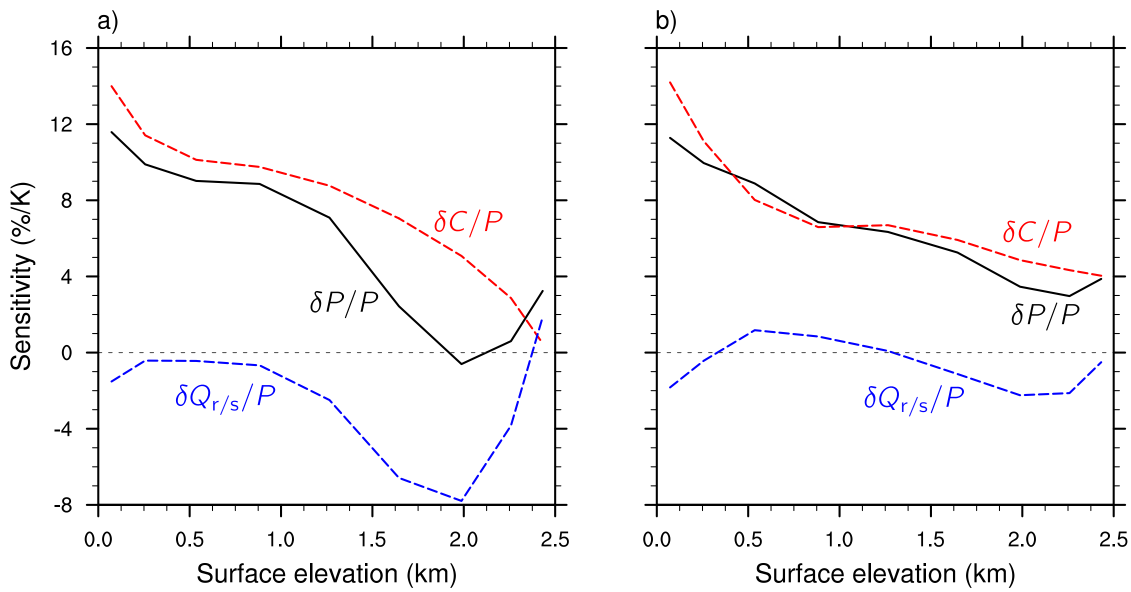

Figure 2.13: Contributions of the changes in the column integrated condensation ($\delta C/P$) and the column integrated rain-snow convergence ($\delta Q_{\mathrm{r/s}}/P$) to the elevational dependence of the sensitivity of precipitation extremes ($\delta P/P$) in a) western-slope events and b) eastern-slope events.

integrated precipitation rate to increased CO_2 satisfies

$$\frac{\delta P}{P} = \frac{\delta C}{P} + \frac{\delta Q_{\mathrm{r/s}}}{P}\,. \tag{2.13}$$

The amplitude of each term in (2.13) is shown in Fig. 2.13. While the sensitivity of condensation ($\delta C/C$) shows little dependence on surface elevation (not shown), the sensitivity of precipitation ($\delta P/P$) and the contribution of condensation ($\delta C/P$) generally decrease with elevation. This is primarily because the factor $1/P$ decreases with elevation (Fig. 2.12). For the eastern-slope events, the normalized changes in condensation $\delta C/P$ account for most of the precipitation sensitivity, but over the upper part the western slope events (between elevations of 1.4 and 2.2 km), $\delta P/P$ is much smaller than $\delta C/P$. This difference between $\delta P/P$ and $\delta C/P$ is associated with large negative values of $\delta Q_{\mathrm{r/s}}/P$ over the same upper

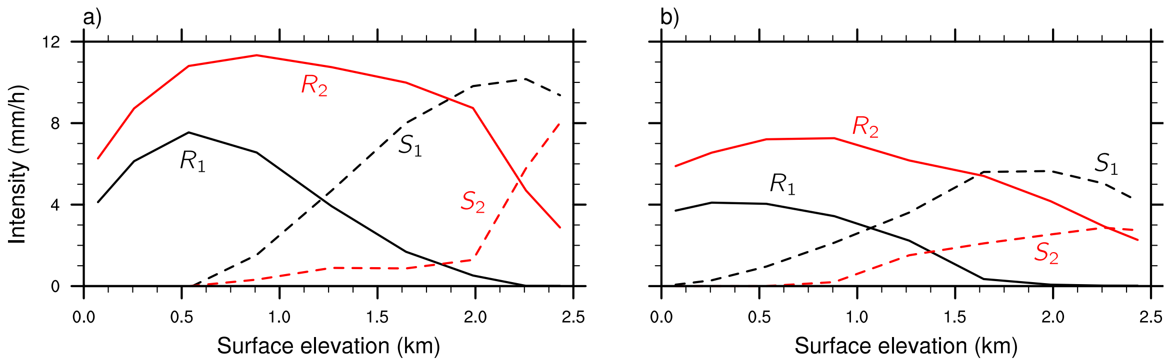

Figure 2.14: The 24-hour mean intensity of surface rain (R) and snow (S) of a) western-slope and b) eastern-slope extreme events in the control (black) and warmed (red) climate. The subscripts "1" and "2" indicate values for the $1 \times CO_2$ and $2 \times CO_2$ climates, respectively.

part of the western slope. These negative values of $\delta Q_{\mathrm{r/s}}/P$ arise almost entirely because the column integrated horizontal flux of snow becomes more divergent above the upper slopes of the mountain in the warmer climate.

Separating the detailed factors responsible for the increased divergence of $Q_{\mathrm{r/s}}$ in the warmer climate is rather involved, but the common denominator is the rise in the melting level. In those extreme events, the melting level in the warmer climate rises by about 1 km in our simulations via processes detailed in Minder et al. (2011). As a consequence, most of the surface precipitation above a height of 500 m switches from snow to rain (Fig. 2.14), which as noted previously, could produce more runoff and flooding during these extreme events.

2.7 Summary and discussion

The processes responsible for changes in mid-latitude extreme orographic precipitation in a warmer world have been examined using a hierarchy of models to effectively simulate 40 years of weather over an idealized north-south ridge on the western margin of a continent very roughly representative of western North American. Control and doubled-CO_2 climates were computed using the GFDL global HiRAM model, and the top ten 24-hour precipitation events on the western and eastern mountain slopes in both climates were re-simulated at higher resolution with the WRF weather prediction model.

The extreme precipitation events on the western and eastern slopes of the idealized mountains tend to occur in different seasons and under different weather patterns. The western-slope events mostly occur in winter months, when a strong atmospheric river embedded in a westerly jet impinges on the western side of the mountains. The eastern-slope events occur most frequently in summertime, when a cyclone to the south produces southeasterly winds and an intense plume of moisture impinges on the slopes of the region experiencing heavy rainfall. Several of the eastern-slope extreme events exhibited synoptic weather patterns strikingly similar to the September 11-13, 2013 floods along the Colorado Front Range.

The 24-hour precipitation intensities for the top-10-event WRF simulations increased on the eastern side by 5.9 $\%K^{-1}$ of global-averaged surface temperature increase, and by a somewhat smaller 4.2 $\%K^{-1}$ on the western side. Similar values of 6.3 $\%K^{-1}$ over the eastern slopes and 3.9 $\%K^{-1}$ in the west were obtained for the top 40 events in the HiRAM simulations. The vertically-integrated condensation rate for the top-10-event WRF simulations gave a good approximation to the sensitivity of the precipitation to global warming, including the roughly 2 $\%K^{-1}$ difference in the sensitivity between the eastern and western slopes.

The of thermodynamic sensitivity of condensation in eastern-slope and western-slope precipitation extremes is estimated as 3.9 $\%\,K^{-1}$ and 5.0 $\%\,K^{-1}$. These values are close to previous estimates by Shi and Durran (2014) for general orographic precipitation on the windward side of midlatitude mountains under the assumption that the incoming flow is saturated (as in these extreme events). Under these conditions, the thermodynamic sensitivity ranged between 4 and 5$\%K^{-1}$ ($\delta \dot{\Gamma}_s/M$ in their Fig. 11). The thermodynamic sensitivity for the western-slope extreme events here is about 1 $\%K^{-1}$ greater than that for the warmer summertime events over the eastern slope. This is consistent with their wintertime occurrence at colder temperatures.

The difference between the thermodynamic sensitivity of eastern and western slope extremes was overshadowed by a 3 $\%K^{-1}$ greater dynamical contribution to precipitation sensitivity in the east than in the west due to differences in the vertical velocity. The sensitivity of the vertical velocities driving the eastern- and western-slope events was well approximated by a three-layer linear mountain wave model and is due to warming induced increases in upper tropospheric static stability and the tropopause height. The difference in sensitivity for the eastern- and western-slope vertical velocities is primarily due to differences in the strength of the mean cross-mountain flow, with much weaker winds occurring during the eastern-slope events. Higher precipitation sensitivities might have been expected to occur on the eastern side through an alternate thermodynamic mechanism proposed by Siler and Roe (2014). They noted that under moist saturated conditions, increases in surface temperature produce relatively more condensation aloft, which is more easily advected downwind of the crest to fall on the lee-slope. None of the extreme eastern-slope events in our simulations involve significant westerly flow at the mountain crest, and as a consequence, their downwind-advection mechanism is not active.

Although the precipitation thresholds defining our extreme events shift with the climate to remain "once-per-year" and "once-per-four-year" events, the number of events exceeding the control-climate thresholds increases dramatically in the warmer world. On both sides of the mountain, once-per-year events in the control climate occur on average three times per year in the warmer world. Once-per-four-year events shift, on average, to once every year.

The sensitivity of the precipitation to warming generally decreases with altitude in the WRF simulations, although much of this change is simply due to the way the baseline control-climate precipitation increases with elevation. An exception occurs over the western-slopes on the upper portion of the mountain, where the precipitation sensitivity is further reduced by an increase in the column-averaged divergence of snow and rain. This increased divergence is related to an increase in the height of the melting level in the warmer climate. The most important impact of the change in melting level, however, is to produce a major shift from snow to rain over much of the mountain slope. Such shifts during extreme events have the potential to produce much more runoff and flooding over mountain slopes.

Clearly one must expect quantitative differences between these idealized simulations and climate-model simulations of extreme precipitation over any actual mid-latitude mountain range, and further study is required to determine specific real-world responses. Nevertheless, the general physical basis for the changes in mid-latitude orographic precipitation extremes revealed by our idealized simulations may have widespread applicability. One piece of evidence supporting this comes from Diffenbaugh et al. (2005) and Singh et al. (2013) who, consistent with our result that eastern-slope extreme precipitation increases more rapidly than in the west, found a weakening of the orographic rain shadow in the warmer climate over the north-western United States that was largely due to changes in extreme precipitation.

Chapter 3

Rapid Strengthening of Extreme Precipitation over Oceans and Plains

3.1 Introduction

Although the global mean precipitation increases at only $\sim$2% K^{-1} in response to global warming due to energetic constraints on the atmosphere (Held and Soden, 2006; Allen and Ingram, 2002; Takahashi, 2009), simulated precipitation extremes increase much faster over many regions of the world (Emori and Brown, 2005; Kharin et al., 2007; O'Gorman, 2012), strongly impacting natural disasters such as flooding and landslides (Pall et al., 2011; Rasmussen and Houze, 2012). In the tropics, climate-model results constrained by observation suggest extreme precipitation (99.9th percentile of daily precipitation) increases at $\sim$10% K^{-1} of increase in the global mean surface temperature (O'Gorman, 2012). In the extratropics, simulations suggest extreme precipitation will increase at roughly the 'thermodynamic' rate of $\sim$6% K^{-1}, which is the rate that would be produced by temperature increases at fixed relative humidity when vertical motions stay constant (O'Gorman and Schneider, 2009a). Yet the preceding large-scale averages are not necessarily representative of the high-impact changes that may occur in extreme precipitation over local regions (Diffenbaugh et al., 2005). Recent studies based on regional climate simulations suggest that in some mid-latitude regions, such as the Netherlands and the western United States, extreme precipitation could increase at rates of 9% K^{-1} or higher (Dominguez et al., 2012; Attema et al., 2014).

Here I use the idealized setting to explore fundamental physical factors tending to produce systematic variations in extreme precipitation over three mid-latitude regions: mountains, oceans and plains. Over mid-latitude mountains, deviations in the sensitivity of extreme precipitation from the thermodynamic rate of 6% K^{-1} have been linked through mountain-wave dynamics to warming-induced changes in tropopause height and static stability (Frierson, 2006; Vallis et al., 2014; Siler and Durran, 2015; Shi and Durran, 2015). Extreme precipitation over the mid-latitude oceans and plains, on the other hand, is governed by the dynamics of mid-latitude cyclones, and responds differently.

3.2 Models and methods

To assess the potentially different response of extreme precipitation over mid-latitude mountains, oceans and plains, I analyzed 10 years of data for a pair of climate simulations with reference (330 ppm) and doubled (660 ppm) CO_2 concentrations. I use idealized topography, with four north-south mountain barriers at the western margin of otherwise flat continents symmetrically distributed about the pole in the latitude band between 30 to 60°N; the remainder of the planet is covered with a mixed-layer ocean (Fig. 3.1).

The simulations were again conducted with the Geophysical Fluid Dynamics Laboratory (GFDL) global High Resolution Atmospheric Model (Zhao et al., 2009), run at ∼50 km horizontal resolution, with 32 vertical levels, and a 24-m deep mixed-layer ocean. Vegetation on the continents in the LM2 land-surface model was set to "broadleaf/needleleaf trees" on the western slopes of the mountains and to "grasslands" on the eastern slopes and plains. The annual cycle was included using daily averaged insolation. Twenty-year simulations were conducted with control (330 ppm) and doubled-CO_2 (660 ppm) concentrations. Six-hourly data from the last 10 years were retained for analysis. The global-mean surface temperature increase due to doubling CO_2 was 5 K.

The idealized mountains are well-resolved by the model and their simple geometry facilitates the comparison of extreme events across different latitudes. The original data on cubed-sphere grids were interpolated onto a 0.5° latitude by 0.625° longitude grid. I di-

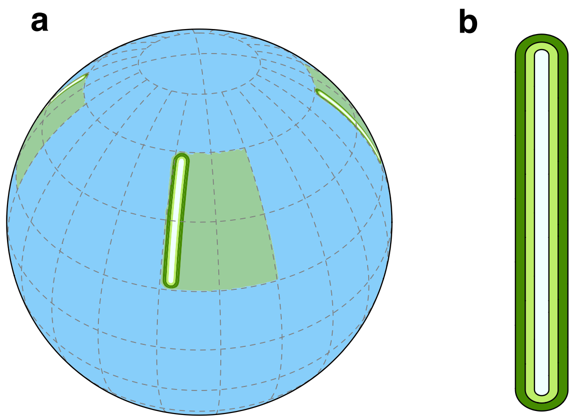

Figure 3.1: Shape of the idealized mountains and continents. a, distribution of the mountains (white), continents (green), oceans (blue). b, detail of the mountain located at the western margin of each continent (elevations contoured at 0, 1 and 2 km).

vide the mid-latitudes into 2.5°-wide bands. Within each band, 6-hourly precipitation is accumulated at each grid cell at all times and longitudes and aggregated for each of three surface types: oceans, plains, or mountains. The precipitation accumulated over each 6-hour period at each grid point is flagged as extreme if it exceeds the 99.9th percentile value in its respective dataset. That means each 6-hour period at each grid cell constituted a single event, and extreme precipitation events are defined as the top 0.1% of all precipitation events over a given type of surface. In each 2.5° latitude band between 32.5° and 57.5° N, there were roughly 27,000 extreme events over the oceans, 11,000 over the plains, and 4,000 over the mountains. The bands 30° to 32.5° N and 57.5° to 60° N, which contain the ends of the mountains, were neglected. The relatively short 6-hour interval is chosen to allow us to connect the heavy precipitation events with instantaneous atmospheric fields archived at the middle time of each interval. Over oceans and plains, most of the extremes are in summer and autumn. Over mountains, most of the extremes occur over the western slopes in autumn and winter.

3.3 Comparing thermodynamic and dynamic sensitivities

Figure 3.2a compares the sensitivities of extreme precipitation (defined as the percentage change in mean intensity divided by the global-mean surface temperature increase) over the oceans, plains, and mountains in each latitude band. The sensitivity of extreme precipitation over the oceans is similar to that over the plains, about 8% K^{-1}. In contrast, the sensitivity of extreme precipitation over the mountains is lower, just 5% K^{-1}. The average overall sensitivity of our simulated midlatitude extreme events, computed without differentiating between the regions, is about 7% K^{-1}, which is similar to previous estimates of midlatitude sensitivities from the Coupled Model Intercomparison Project phase 3 (CMIP3) archive(O'Gorman and Schneider, 2009a). The sensitivity of extreme precipitation over the Southern Hemisphere mid-latitude oceans is similar to its Northern Hemisphere counterpart. As apparent in Fig. 3.2a, the dependence of all of these sensitivities on latitude is relatively weak.

These sensitivities are primarily due to changes in the grid-resolved fields, since over 98% of the precipitation in the extreme events in Fig. 3.2 is generated by grid-resolved process, rather than parameterized convection. Parameterized convection does produce 40–50% of the total July precipitation along the southern margins of the continents and is more active further south over the tropical oceans, but typical static stabilities during the extreme midlatitude events are approximately neutral to moist adiabatic ascent (rather than convectively unstable), as was observed, for example, during the extreme Colorado flooding of September, 2013 (Shi and Durran, 2015; Gochis et al., 2015).

The sensitivity of the extreme precipitation at each surface grid point is well approximated by the sensitivity of the vertically integrated condensation rate above that point C, because changes in precipitation efficiency (the ratio of surface precipitation to the vertical integral of condensation aloft) are small enough to be neglected. The condensation rate in a saturated grid cell may be estimated by assuming adiabatic lifting maintains the water vapor content of the rising air at saturation, and the condensation in each cell can be summed

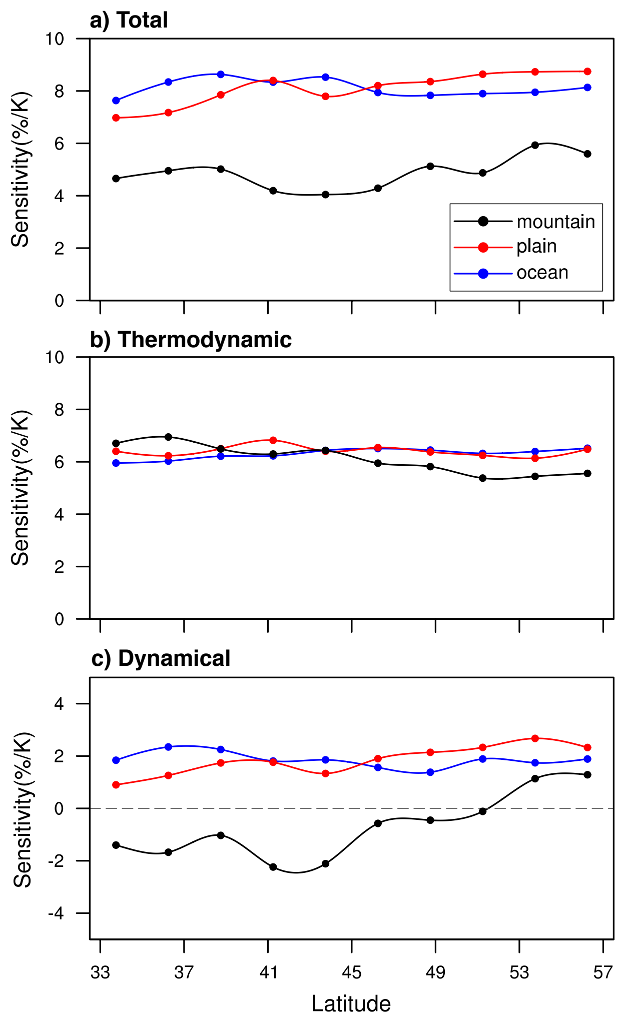

Figure 3.2: Sensitivity of a) precipitation rate, b) thermodynamic response, c) and dynamical response of extreme events, plotted for each latitude band (solid dots) over the mountains, oceans and plains.

through the vertical column to estimate C. Letting δ denote the change in the extreme-event averages between the warmer and control climates, the change in precipitation δP can then be estimated from two contributions. One contribution is from the dynamics and arises from changes in the vertical velocities δw. The second contribution is from thermodynamics and arises from changes in the adiabatic lapse rate of the saturation specific humidity of water vapor $\delta\gamma_s$. This partition is done as follows. Let w be the vertical velocity and $\gamma_s = -\mathrm{d}q_s/\mathrm{d}z$ is the adiabatic lapse rate of the saturation specific humidity of water vapor (q_s). Neglecting precipitation efficiency, which will factor out of our final expression if I ignore its small variations, the precipitation at the surface equals the column integrated condensation aloft $C = \sum_k s_k w_k (\gamma_s)_k$, where k indexes the vertical level and $s_k = \Delta p_k/g$ in saturated grid cells, but is zero otherwise. Here Δp_k is the pressure thickness of layer k and g is the gravitational constant. Denoting extreme-event averaging in the control and warmer climates by $\overline{(\ \ )}^c$ and $\overline{(\ \ )}^w$ respectively, the change in the extreme-event averaged column integrated condensation is

$$\delta C = \overline{C}^w - \overline{C}^c = \sum_k \overline{(s_k w_k (\gamma_s)_k)}^w - \sum_k \overline{(s_k w_k (\gamma_s)_k)}^c. \tag{3.1}$$

The preceding is approximated as

$$\delta C \approx \sum_k \overline{\overline{(s_k w_k)}}\,(\delta\gamma_s)_k + \sum_k \overline{\overline{(s_k (\gamma_s)_k)}}\,\delta w_k, \tag{3.2}$$

where the double overbar denotes the average over extreme events in both climates. The two terms on the right-hand side are the dynamic and thermodynamic response, respectively. Instantaneous values of the fields at the middle of each 6-hour precipitation period were used to evaluate these expressions.

Panels b and c in Fig. 3.2 compare the thermodynamic and dynamic sensitivity of extreme precipitation over the oceans, mountains, and plains in each latitude band. Thermodynamic sensitivities are similar, around 6% K^{-1}, in all latitude bands with less than a 1% K^{-1} variation between them. In contrast, there is a significant difference in the dynamic sensitivities between the mountains and the flat areas in all except the two northernmost latitude bands. The dynamic sensitivities over mountains are near zero or negative in most bands, while over the oceans and plains, the dynamic sensitivities are positive. Except in the northernmost two bands, the differences between the dynamic sensitivities over flat areas and mountains explain most of the differences in the sensitivities of extreme precipitation over those regions.

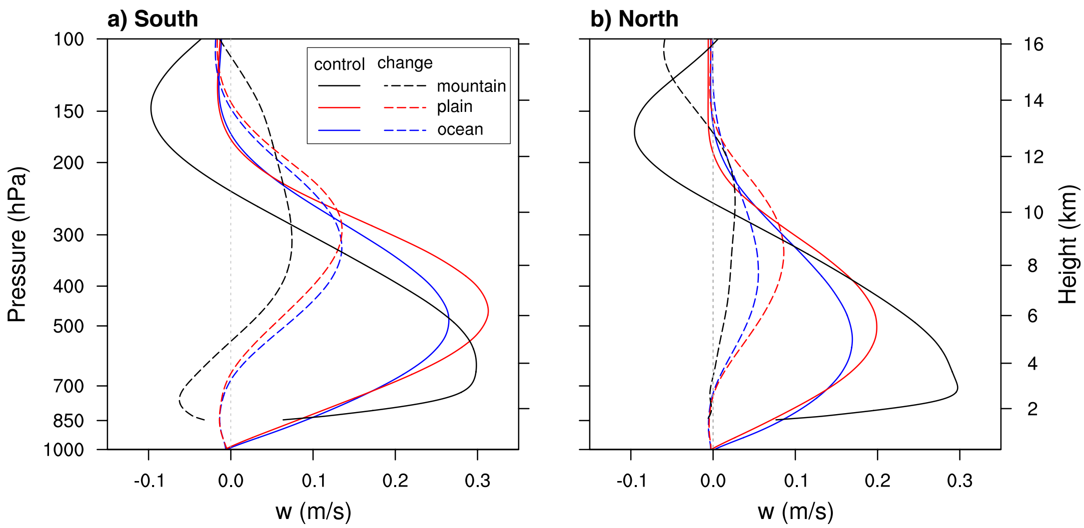

Figure 3.3: Mean vertical velocity profiles in extreme precipitation events from the control simulation and their changes due to warming. Averages over five latitude bands in the **a**) south **b**) north. For those extreme events over mountains, profiles beginning at different surface elevations are scaled to begin at the height of middle of the mountain slope before computing the average.

The differences in dynamic sensitivities for the extreme precipitation events shown in Fig. 3.2c suggests there are significant differences in the global-warming-induced changes in the vertical velocities over the mountains, oceans and plains. Fig. 3.3 compares vertical profiles of w during the extreme events over each region the reference climate. Over the oceans and the plains, a deep region of ascent extends from the surface to at least 200 hPa, the peak ascent near 500 hPa is stronger and at a somewhat higher level in the south half of the analysis region Fig. 3.3a, than in the north Fig. 3.3b. In contrast, the vertical velocity over the mountains, which is dominated by mountain-wave dynamics, is similar in the south and north, peaks at much lower levels (near 700 hPa), reverses sign around 250 hPa, and becomes strongly negative aloft.

Also shown in Fig. 3.3 are δw, the changes in w in the warmer world. In the north

(Fig. 3.3b) all three δw profiles are very slightly negative below 700 hPa and become positive further aloft where δw for the oceans exceeds that for the plains, which in turn exceeds the δw for the mountains. The relative strength of the positive δw account for the average differences in the dynamical sensitivity over the five northern latitude bands in Fig. 3.2c. The changes in δw in the south also account for the dynamical sensitivities in the southern latitude bands, but the character of those changes is different. In the south (Fig. 3.3a), the δw over the mountains is strongly negative between mountain-top height and about 550 hPa, and its extreme is roughly four times more negative than that for the weak low-level negatives that occur for δw over the oceans and the plains. Since the moisture content of the atmosphere decreases rapidly with height, the dynamical sensitivity is most strongly affected by changes in the ascent at low levels, where the negative values of δw are responsible for the negative sensitivities apparent in the southern latitude bands in Fig. 3.2c.

3.4 Why the vertical velocity changes over mountains

Recent studies using a three-layer model of linear hydrostatic mountain waves(Klemp and Lilly, 1975) demonstrate that gravity waves play a key role in regulating the intensity of orographic precipitation under stable or low-level moist neutral conditions(Siler and Durran, 2015; Shi and Durran, 2015). Here I use the same three-layer model to determine the factors responsible for the changes in the vertical velocities that give rise to the dynamic sensitivities shown in Fig. 3.2c.

A representative value $\alpha_i = 4 \times 10^{-3}\,\mathrm{s}^{-1}$ is used for the wind shears in the lowest two layers of the linear model, for both the control and warmed climate. I computed the mean zonal wind speed at the level above boundary layer top, $\sim$800 hPa, with simulation data, and used it as the wind speed (U) at the bottom of the linear model. The static stability in the stratosphere is set to $2 \times 10^{-2}\,\mathrm{s}^{-1}$, representative for both the control and warmed climate. The boundary between the lowest layer and the middle layer of the linear model is assumed to be at one half of tropopause height (H). Although in some events middle-level air can become saturated, the small amount of moisture in the upper troposphere make the moist stability in that layer significantly larger than in the lower troposphere, so I used the mean dry stability between 300 and 500 hPa from simulation data as the stability of the middle layer (N_2) in the linear model, and mean moist static stability between 500–850 hPa as the moist stability of the lowest layer (N_1). The parameters, N_2, U, and H, were evaluated from simulation data upstream of each event, ~100 km to the west of mountains. N_1, which must be calculated in a saturated environment, was evaluated above mountains slopes in the columns producing intense precipitation. The values of those relevant parameters were averaged over the roughly 4,000 extreme orographic precipitation events in each latitude band to obtain a representative mean environment for each band in both the control and doubled-CO_2 climates. Vertical velocities in each band were computed from the linear model using these mean environmental parameters for a location above the middle of the windward slope at an elevation 3 km MSL, which approximates the level where the vertical velocity profiles over the mountains achieve their maximums in Fig. 3.3.

The sensitivities $\delta w/w$ obtained with the linear model are compared to those for the vertical velocity at the same elevation from the full climate simulations in Fig. 3.4a. Although it uses linearized dynamics and a simplified environment averaged across all the extreme events in a given latitude band, the three-layer model provides reasonable approximations to the vertical-velocity sensitivities obtained directly from the full climate simulation, both of which vary between $-6\%\ \mathrm{K}^{-1}$ in the south to about $1\%\ \mathrm{K}^{-1}$ in the north. Based on its agreement with the sensitivity of the vertical velocities computed by the climate model, the linear mountain-wave model may be used to estimate the contributions to $\delta w/w$ from each individual environmental parameter by holding all other parameters at their mean values and evaluating the change δw generated by the simulated global-warming-induced changes in that parameter.

Figure 3.4b suggests the changes in wind speed U and upper troposphere dry static stability N_2 exert the most influence on the response of windward slope ascent during extreme orographic precipitation. Decreases in zonal wind speed in the southern latitudes weaken the ascending motions there by roughly $-4\%\ \mathrm{K}^{-1}$, while increases in the winds in the north

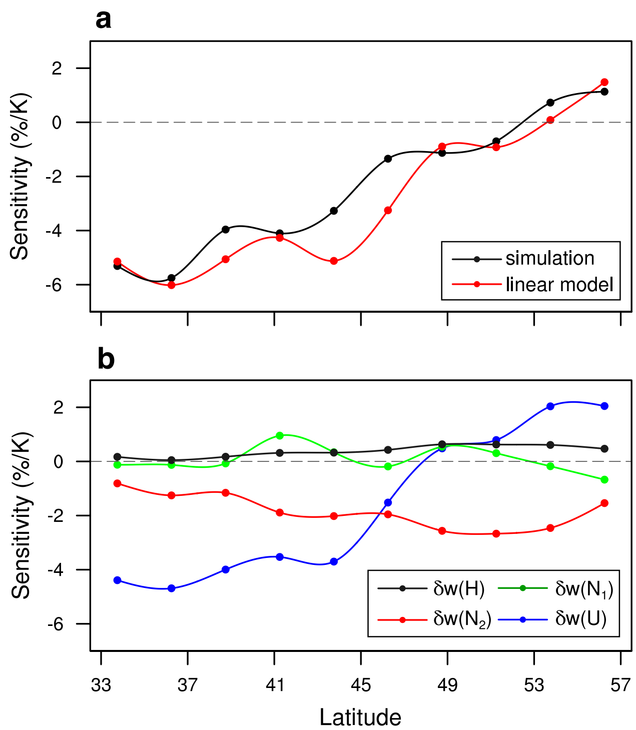

Figure 3.4: Sensitivities in the vertical velocities over mountains to surface global warming as predicted by the linear model. **a** comparison of vertical velocity sensitivities from the linear model and full simulation at the 3-km level; **b** Factors responsible for the linear model sensitivities: tropopause height (H), lower troposphere moist static stability (N_1), upper troposphere dry static stability (N_2), and zonal wind (U).

produce a modest strengthening of 2% K^{-1}. These changes in the zonal winds are consistent with a poleward shift of the jet stream similar to that found in previous studies(Vallis et al., 2014). The dry static stability increases under global warming, and the increase in N_2 weakens the orographic ascent at all latitudes. This stabilization of the atmosphere is a robust change in atmospheric structure that is not limited to just the extreme events (Vallis et al., 2014).

As also evident in Fig. 3.4b, the changes in the other mountain-wave-model parameters have only a minimal influence on the vertical velocities. The low-level moist static stability

N_1 does not change much under warming. The tropopause height rises about 1 km in the northern latitude bands, but does not significantly modify the vertical velocity. Care must be taken if one wishes to generalize the influence exerted by the individual parameters shown in Fig. 3.4b to other flow regimes; for example, changes in H can be more important when U is smaller, as may be the case during extreme orographic precipitation events on the eastern side of the mountain barriers(Shi and Durran, 2015).

3.5 Why the vertical velocity changes over the oceans and plains

What drives the changes in vertical velocities producing extreme precipitation over the oceans and the plains? Most of these events occur just to the northwest of the low pressure center in mid-latitude cyclones as shown by the composites in of surface pressure and 850-

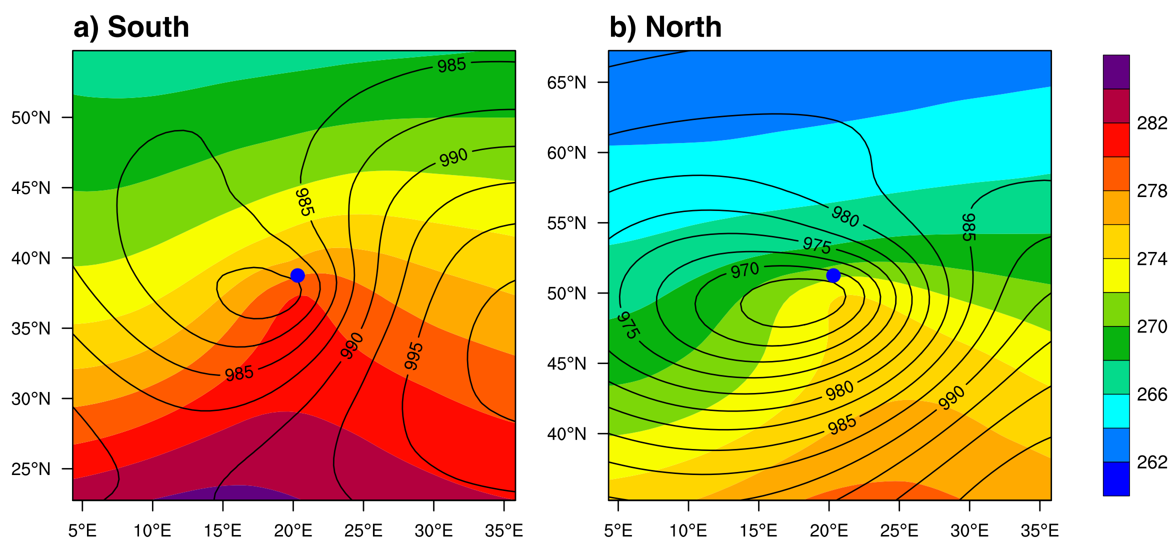

Figure 3.5: Composite surface isobars (hPa) and 850 hPa temperatures (K) for heavy precipitation events over the oceans. Blue dot locates the center of the precipitation event. Composites include all extreme oceanic events more than 15° west of the mountains in the latitude bands centered at **a** 38.75° S and **b** 51.25° N.

hPa temperatures for oceanic extreme events plotted in Fig. 3.5. The location of the heavy precipitation event anchoring the composite is shown by the blue dot, the composited pressure and temperature fields are the instantaneous fields centered in time for each 6-hr event. Fig. 3.5a is computed using data over the oceans from the central latitude band in the south (centered on 38.75° N); Fig. 3.5b shows the same information for the north (centered on 51.25° N). In both cases, those events within 15° latitude of the west-coast mountain ranges are omitted to keep the mountain-induced perturbations from appearing in the domains shown in Fig. 3.5. The heavy precipitation is located in the region of strongest temperature gradient where heavy rainfall associated with warm or occluded fronts is observed in marine cyclones(Chang et al., 1993).

The key factors responsible for the increase in vertical velocities during these events can be determined from the thermodynamic equation, which may be expressed in terms of the potential temperature θ as

$$\frac{\partial \theta}{\partial t} + \boldsymbol{V} \cdot \nabla \theta + w \frac{\partial \theta}{\partial z} = F_\theta \,, \tag{3.3}$$

where $\boldsymbol{V}$ is horizontal wind vector, and F_θ is the sum of diabatic forcing due to latent heating and radiation. Letting the material derivative of θ in a parcel following the horizontal flow be denoted as $\mathrm{D_h}\theta \equiv (\partial\theta/\partial t + \boldsymbol{V} \cdot \nabla\theta)$, (3.3) implies

$$w = \frac{F_\theta - \mathrm{D_h}\theta}{\partial\theta/\partial z} \equiv \frac{F}{S} \,, \tag{3.4}$$

where F is the total forcing and S is the stratification.

Letting w_a, F_a and S_a denote the averages of w, F and S between the control and warmer climates. The changes δw, δF and δS between the control and warmer climates may be estimated from (3.4) as

$$w_a + \delta w/2 = \frac{F_a + \delta F/2}{S_a + \delta S/2}, \tag{3.5}$$

which, without further approximation, implies

$$\frac{\delta w}{w_a} = \frac{\delta F/F_a - \delta S/S_a}{1 + \delta S/(2S_a)}. \tag{3.6}$$

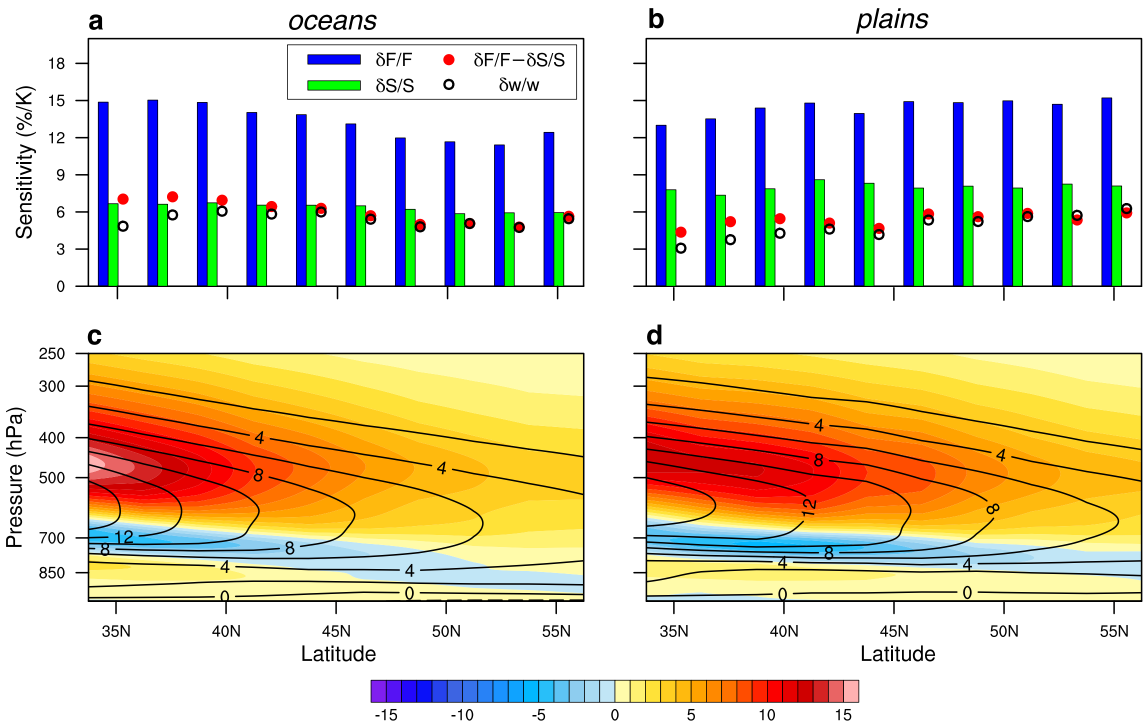

Figure 3.6: Factors governing warming-induced changes in the vertical velocity during extreme events over the oceans and plains as a function of latitude. The sensitivity of the zonally averaged total forcing ($\delta F/F$), stratification ($\delta S/S$), vertical velocity ($\delta w/w$), and diagnosed vertical velocity $(\delta F/F_a - \delta S/S_a)/[1 + \delta S/(2S_a)]$ (labeled as $\delta F/F - \delta S/S$) at 500 hPa for extreme events over the **a** oceans and **b** plains. **c** and **d** show the averaged diabatic forcing (F_l) in the control climate (contours) and the change due to warming (color shading).

Values of w, F, and S were computed at the model level closest to 500 hPa for all extreme events in the reference and doubled-CO_2 climates. These values were used to estimate the average of each term in (3.6) over the oceans and the plains in each latitude band. The results, expressed as sensitivities with respect to the global mean surface temperature, are plotted in Fig. 3.6a,b. Except in the two southernmost bands, the average sensitivity computed from (3.6) (red dot) provides a very good estimate of the average $\delta w/w_a$ evaluated directly

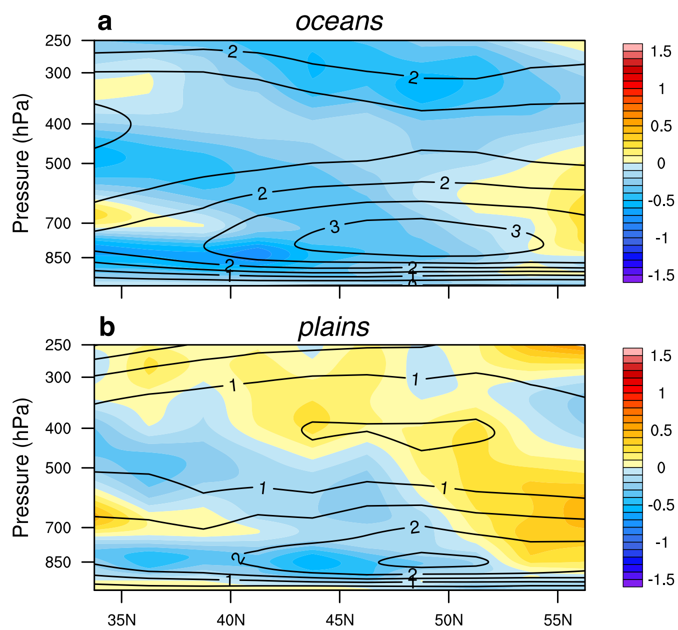

Figure 3.7: The adiabatic forcing to vertical motion in the control climate (contours) and changes due to warming (color shading) for extreme events over oceans and plains.

from the vertical velocities output by the model (open circles). The errors in the south arise because the residual, by which our estimate of the terms in (3.3) fails to match the exact calculation in the model, is larger in warmer regions. The residual exists because the evaluation of terms in (3.3) used centered difference, which is not the same as the calculation in the finite volume climate model. Particularly, the evaluation of $\partial\theta/\partial t$ used 6-hourly data.

As shown by the vertical bars in Fig. 3.6a,b, $\delta F/F_a$ tends to produce an 11–14% K^{-1} increase in $\delta w/w_a$ that is partially offset by a 4–7% K^{-1} increase in $\delta S/S_a$ arising from the stabilization of the atmosphere under global warming. The forcing F may be separated into additive contributions from latent heat released by condensation F_l, radiation F_r, and the changes in θ due to adiabatic horizontal transport, $-\mathrm{D_h}\theta$. The dominant contribution is from latent heating, F_l. Meridional cross-sections of F_l in the control climate and of

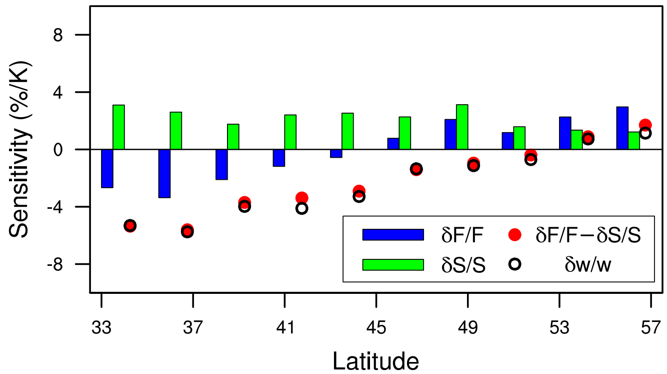

Figure 3.8: Same as Fig. 3.6a and b except that extreme events over mountains are analyzed here.

δF_l, both averaged over all extreme events, are shown for the oceans and the plains in Fig. 3.6c,d. The increased forcing due to latent heating δF_l is largest in the south, and in the mid-troposphere, and accounts for almost all of the mid-tropospheric increase in the vertical velocities over the oceans and plains evident in Fig. 3.3. The contribution to F from radiation is trivial, that from adiabatic transport is small, but not completely insignificant in the north. However, changes in dry cyclone dynamics play only a minor role in the intensification of the precipitation from these extreme events (Fig. 3.7).

The same thermodynamic-equation analysis can of course be applied to the vertical velocities during extreme precipitation events over the mountains. The strongest vertical velocities during extreme precipitation events over the mountains occur near the 700 hPa level (Fig. 3.3), and the thermodynamic-equation analysis at that level is presented in Fig. 3.8. The agreement between the vertical-velocity sensitivity computed from (3.6) again provides a very good estimate of $\delta w/w_a$, but the actual sensitivities over the mountains are very different from those over the oceans and the plains. In particular, the values of $\delta F/F_a$ are negative in the southern latitude bands, due primarily to the decrease in the zonal winds.

3.6 Summary and discussion

The results here demonstrate that mid-latitude extreme precipitation over flat areas intensifies more rapidly than that over mountains under global warming. The thermodynamic sensitivity of extreme precipitation is around $6\,\%\mathrm{K}^{-1}$ over all types of underlying surfaces. However, the upward velocities in orographic extreme event decrease or stay constant at most latitudes, whereas the extreme events over flat areas have enhanced ascent, due to the stronger diabatic forcing from moist processes in the warming climate.

Admittedly, the response of ascent over mountains depends on the prevailing conditions under which orographic extreme precipitation occurs. The extreme precipitation over eastern slopes of mountains, for example, may also gain some dynamical enhancement under climate change in its particular parameter regime (Shi and Durran, 2015). The extreme precipitation over flat areas, however, does not seem to be sensitive to latitude, and responds to warming similarly over land and ocean.

The simple idealized shapes of the mountains and the continents used in our simulations precludes the direct quantitative application of our results to specific locations on the earth, yet the fundamental dynamical drivers of actual extreme events are likely to be subject to the same basic sensitivities identified in our simulations. Mountain-wave induced ascent should occur throughout a shallower vertical layer than the lifting near warm and occluded fronts in mid-latitude cyclones. Ascent over mountains is sensitive to the change in horizontal wind speed and stability because those factor change the amplitude and wavelength of mountain waves directly, and the global-warming induced change in those variable could affect orographic ascent through mountain wave dynamics. The ascending motion in extreme events over oceans and plains, on the other hand, is strongly affected by diabatic forcing, and ought to become stronger as temperature rises.

This rapid intensification of precipitation extreme, in addition to other problems such as sea level rise (Rahmstorf, 2007) and threatened biomes (Peterson, 2003; Loarie et al., 2009), implies the population in flat regions would need to put more economic and social efforts for their adaptation to global warming. Our finding also provides additional motivation for using higher resolutions in anthropogenic warming simulations. Because larger effects from diabatic heating can be expected with higher resolutions when mesoscale structures are well resolved (Willison et al., 2013). Besides, a significant fraction of the world's population do not live on simple plains or mountain slopes, instead they live on complex terrain, such as the vicinity of mountains or in valleys. The exact response of extreme precipitation in those places might be influenced by both gravity waves and diabatic forcings, and thus requires models with sufficiently high resolution in relevant investigations.

Chapter 4

Variability in the Spatial Structure of the Northern Annular Mode

4.1 Introduction

The accurate prediction of future climate under different emission scenarios of greenhouse gases is vital for human's adaptation to and mitigation of climate change. Yet natural variability in the atmosphere could easily obscure the signal from anthropogenic warming on timescales of a few decades and spatial scales smaller than continental (Deser et al., 2012a; Hawkins and Sutton, 2012). By formally partitioning the cold-season surface air temperature trends into dynamically induced and radiatively forced components, Wallace et al. (2012) demonstrated that much of the enhanced wintertime warming over high northern latitudes from 1965 to 2000 was induced by the internal variability of the coupled climate system. Deser et al. (2012b), through comparing individual members of a 40-member ensemble, found that the dominant source of uncertainty in the simulated climate response at middle and high latitudes is internal atmospheric variability associated with the annular modes.

The persistence of annular modes can be explained as a result from the interaction between baroclinic eddies and a barotropic jet (Robinson, 2000; Lorenz and Hartmann, 2001). Gerber and Vallis (2009) studied how the existence of stationary waves leads to zonal localization of storm tracks and annular modes of variability in an idealized general circulation model. They found that both the termination of the storm track and the localization of the intraseasonal variability in their model occurs within difluent regions of weak upper-level flow in the stationary waves, where the eddies break and dissipate. Thus they argued that the North Atlantic storm track and the North Atlantic Oscillation (NAO) are two manifestations of the same phenomenon. Following their interpretation, one could argue it is the same case for the North Pacific storm track and the localized atmospheric variability over the North Pacific. Indeed, the Northern Hemisphere annular mode (NAM) has a strong influence on wintertime climate, over both the Euro-Atlantic half and the Pacific half of the hemisphere (Thompson and Wallace, 2001). Yet whether the North Pacific center of action of NAM is real has been contested (Wallace, 2000; Ambaum et al., 2001; Wallace and Thompson, 2002). The outcome of this debate is inconclusive.

By examining historical data, Quadrelli and Wallace (2002) showed that the structure of NAM is significantly different during warm and cold winters of the ENSO cycle in the historical record. The Community Earth System Model (CESM) Large Ensemble (CESM-LE) project (Kay et al., 2014) provides a unique opportunity to quantify the variability in NAM's structure under the same historical or anthropogenic warming forcings, using a much larger dataset. As will be demonstrated in the following sections, the NAM's centers of action and the coupling between them exhibit significant variations among the individual realizations in CESM-LE. The variations are partly a manifestation of natural variability on the multidecadal time scale and partly due to external forcings.

4.2 Data and analysis techniques

Most of our analysis used monthly and daily averaged data from 30 ensemble members in the CESM-LE project. Those simulations have a 1-degree resolution, running from 1920 to 2100 using historical forcing (1920–2005) and RCP8.5 forcing (2006–2100). Ensemble spread is generated using round-off differences in the initial *atmospheric* state. I discard data between 1920 and 1950 because the unperturbed initial oceanic state might limit the growth of ensemble spread in the first few decades. The remaining 150-year sequence of each ensemble member is divided into three 50-year segments, yielding a total of 90 half-century segments. One could reach the same conclusions about the natural variability in NAM's structure without doing this division, but as will be shown Section 4.6, the NAM's structure exhibits a trend under global warming, which would not be discernible if one only compared differences between the 30 150-year-long ensemble members.

This study focus on the atmosphere in winter months, December through February (DJF). The mean and least squares quadratic trend of each grid point's monthly SLP in each of the three winter months are removed to obtain monthly SLP anomalies, denoted SLP*, and this is done individually for each ensemble member. Whether the data are detrended or not would not change any of our conclusions, but we prefer to do so in order to ensure that the trend in NAM's structure shown in Section 4.6 has nothing to with the long-term trend in wintertime SLP.

The NAM is defined as the leading empirical orthogonal function (EOF) of the SLP* field poleward of 20°N, which was weighted by the square root of the cosine of latitude in the EOF analysis. In this way I obtained 90 spatial patterns for the NAM: one for each of the 90 half-century segments. In order to quantify the variability in the spatial structure of those 90 NAMs, I perform EOF analysis again on the spatial patterns of those NAMs. The resulting leading EOF is called NAM Variability Pattern (NAM-VP), because it explains the largest fraction of variability in NAM's spatial structure, and the corresponding expansion coefficients (i.e. principle components) of NAM-VP are named as NAM-VP Index, since they indicate how the spatial structure of the NAM varies from one 50-year segment of one ensemble member to the same 50-year segment of the next or between different 50-year segments.

Daily SLP data are used in Section 4.4 for evaluating the link between NAM's spatial structure and local intraseasonal variability. For this purpose, the mean SLP of each winter is removed from the corresponding daily data to get daily SLP anomalies, SLP$'$, which reflects variability due to "weather". When calculating the mean spectrum of SLP$'$, the spectrum of each winter's SLP$'$ is calculated with 10% of the data tapered, and then the spectra from multiple winters are averaged. In the calculation of the probability density function (PDF) of SLP′, time series from multiple winters are partitioned into 0.5 hPa-spaced bins, and the resulting PDF is smoothed by a 10-bin running average.

To test whether some of the conclusions drawn from CESM-EL are applicable other models, data from a smaller (10-member) ensemble of climate simulations using the Geophysical Fluid Dynamics Laboratory's (GFDL) climate model CM2.1 are analyzed in Section 4.7. The GFDL simulations were run between 1861–2040 using historical forcing (1861–2006) and RCP4.5 forcing (2006–2040). The last 150 years of data were used for analysis, using the same methodology as described above for the CESM-EL data.

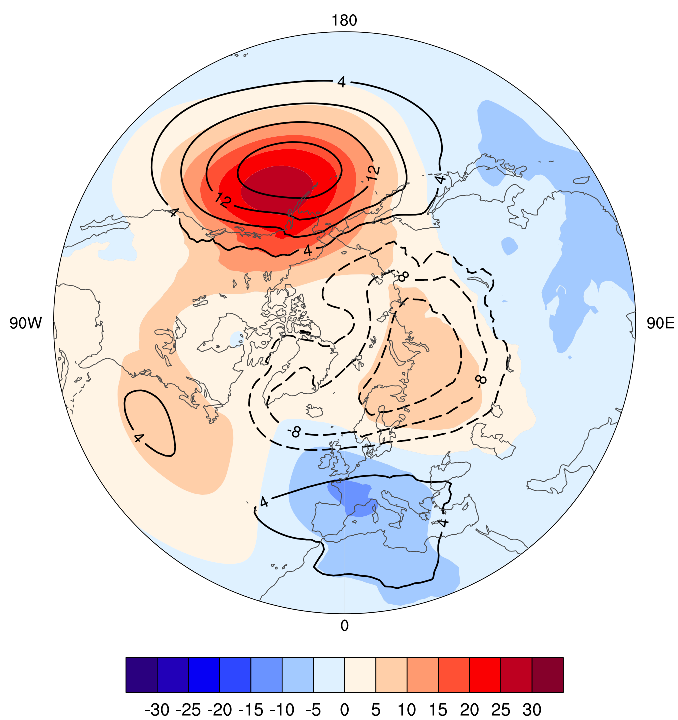

Figure 4.1: The averaged pattern of the NAMs in the 90 50-year samples (contours) and their leading EOF (color shading). Values are multiplied by 10^3 for making contour labels more legible.

4.3 Variability in NAM

The average spatial structure of NAM in the 90 half-century segments is shown in Fig. 4.1 with contours. It features negative correlations between the Arctic region and the extratropics. The Arctic center of action of NAM extends into Siberia, and its positive center of action over the North Pacific is much stronger than its positive center over Europe.

The color shading in Fig. 4.1 shows the NAM-VP, which explains 57% of the variance in the spatial structure of the 90 NAMs in the areas poleward of 20°N. The major center of action of NAM-VP is over the North Pacific, in the Gulf of Alaska, and it is accompanied by a weak negative center of action over Europe. This structure of NAM-VP implies that the strength of the NAM's North Pacific center of action is the subject to large sampling variability. The NAMs in some 50-year segments exhibit a strong North Pacific center and a relatively weak center of action over Europe, whereas those in other 50-year segments, NAMs

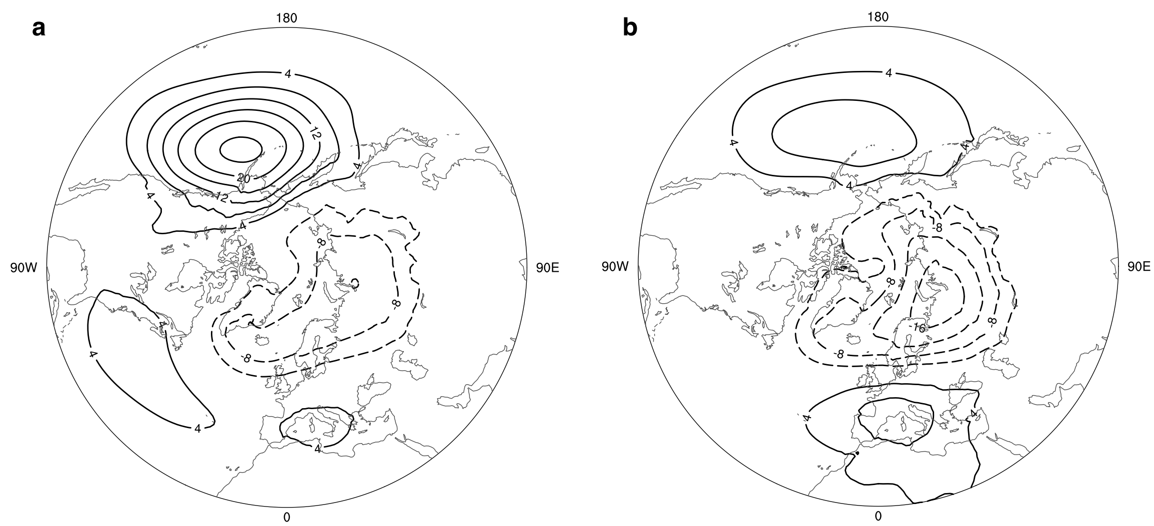

Figure 4.2: The average pattern of the NAM in the 15 samples with the highest values of the NAM-VP Index (a) and in the 15 samples with the lowest values (b). In both panels values are multiplied by 10^3.

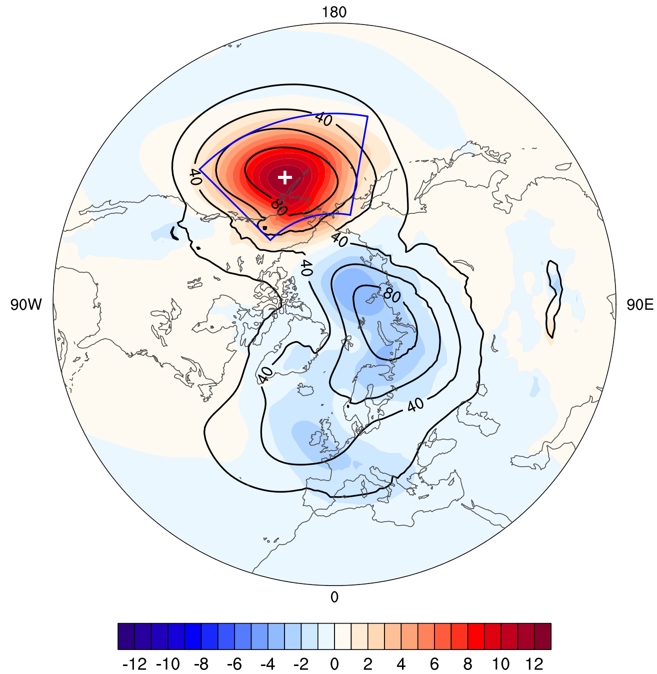

Figure 4.3: The average distribution of SLP variance (hPa^2) in the 90 50-year samples (contours) and the regression coefficients of variance onto standardized NAM-VP index (color shading).

exhibit a relatively weaker North Pacific center and a relatively stronger European center.

The average spatial structures of the NAMs in the 15 samples with the highest values of the NAM-VP Index and the 15 samples with lowest values are plotted in Fig. 4.2 for comparison. As expected, when the NAM-VP Index is high, NAM has a very strong North Pacific center of action and a relatively weak but broad negative center over the Arctic region. The positive centers of action over the Euro-Atlantic region are relatively weak. When the Pattern Index is low, NAM exhibits a more symmetric structure in terms of its extratropical centers of action. The North Pacific and European centers of NAM have similar amplitudes in this case, and the negative Arctic center of action is significantly deeper.

To further explore this dramatic difference between the spatial structure of the NAM in different samples, the variance of SLP* is regressed on the standardized NAM-VP Index (Fig. 4.3). The North Pacific in the Gulf of Alaska and the Arctic region are places with the most variance in SLP*. The regression map of SLP* variance suggests that in the 50-year samples in which the NAM has a strong North Pacific center of action, it also has relatively large amounts of variance in the same area, and somewhat less variance over the Arctic and European regions. A calculation of the area-mean variance in the North Pacific region (the blue box in Fig. 4.3) shows that variance of SLP* over the North Pacific can vary from ∼55 to ∼100 hPa^2 (Fig. 4.8). Thus different spatial configurations of NAM represent statistically different states of the Northern Hemisphere winter circulation.

4.4 Expression of NAM's variability in daily SLP

In this section the link between NAM's spatial pattern and the local weather in the North Pacific is investigated by analyzing SLP′, the daily SLP anomalies. Particularly, I

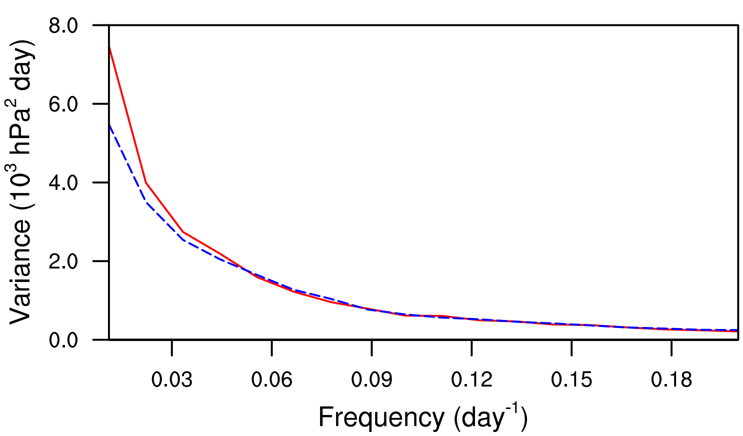

Figure 4.4: The averaged spectrum of daily SLP′ in the winters corresponding to the NAM in the 15 samples with highest values of the NAM-VP index values (red, solid curve) and that corresponding to the NAM in the 15 samples with lowest index values (blue, dashed curve). The spectrum has been normalized such that the area under a curve equals the variance of the corresponding dataset.

examine if the variation in the NAM's structure is related to atmospheric blocking, which has a frequency higher than synoptic eddies. The time series of SLP′ at the point with the largest amount of of regressed SLP* variance (marked by a white cross in Fig. 4.3), denoted as $\mathrm{SLP}'_0(t)$, is used in this the analysis.

Figure 4.4 compares the average spectrum of $\mathrm{SLP}'_0(t)$ in the 15 samples with highest values of the NAM-VP Index and in the 15 samples with lowest index values. When NAM has has a strong North Pacific center, the daily SLP near the Gulf of Alaska has more power at periods longer than 20 days, which is longer than the typical time scale of blocking event

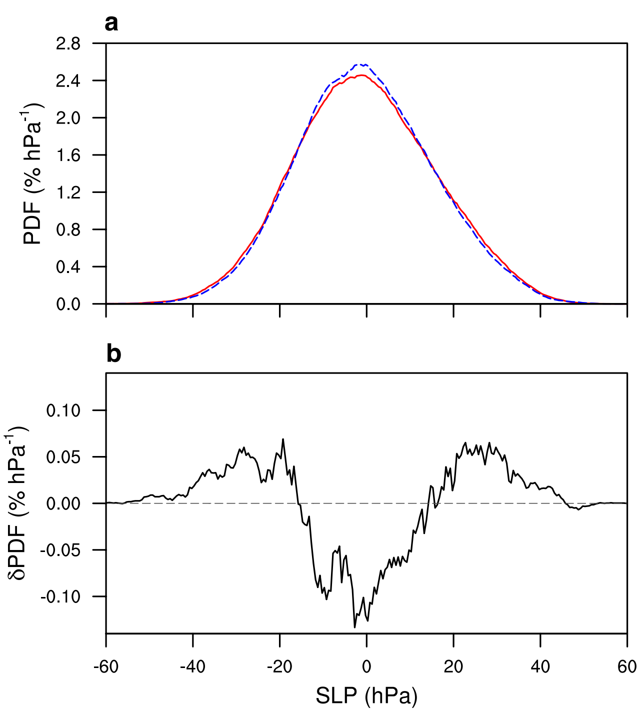

Figure 4.5: a) The averaged PDF of daily SLP anomalies in the winters corresponding to the NAM in the 15 samples with highest NAM-VP Index (red, solid curve) and that corresponding to the NAM in the 15 samples with lowest index values (blue, dashed curve). b) The difference between the red and blue curve in Panel a. Those curves have been normalized so that the area of a curve in Panel a equals 100%.

in the atmosphere. At higher frequencies, two spectra are not distinguishable from each other. This suggests that the differing spatial structures of NAM are not directly related the high frequency disturbances in the atmosphere, such at baroclinic eddies and blocking. Instead, their differences are related to the low frequency perturbations with periods on the order of a month or longer.

Furthermore, the PDFs of $\mathrm{SLP}_0'(t)$ from the 15 half-century segments in which the NAM exhibits a strong North Pacific center and the 15 samples without a strong North Pacific center are compared in Fig. 4.5. Both PDFs are weakly positively skewed. The difference between them, however, is not skewed. In the samples in which the NAM exhibits a strong North Pacific center of action, the corresponding daily SLP has both more positive anomalies and negative anomalies, suggesting the existence of more variability in time. This supports the notion that the variability in NAM's spatial structure is not not related to any special type of weather phenomenon, such as atmospheric blocking.

4.5 NAM's structure and the upper-level jet

Since much of the low-frequency variability of the Northern Hemisphere wintertime circulation is associated with disturbances that derive their energy from the basic state (Simmons et al., 1983), this section examines variations in the mean climatology that affect the structure of the leading pattern of low frequency, planetary wave variability, the NAM.

The time-mean SLP fields of each 50-year sample was regressed onto the NAM-VP Index first, but no consistent regression pattern was found. The regression maps based on different time periods, e.g. the first, middle, and third 50 years, each show different patterns, and when all periods are mixed in the regression, the resulting map is another different pattern that resembles the global warming-induced trend in mean SLP field. However, there does appear to be a consistent relationship between NAM-VP and the background flow at the jet stream level.

Figure 4.6 shows regression maps of time mean 200-hPa zonal wind onto the NAM-VP Index for different periods, along with the corresponding ensemble mean climatology in

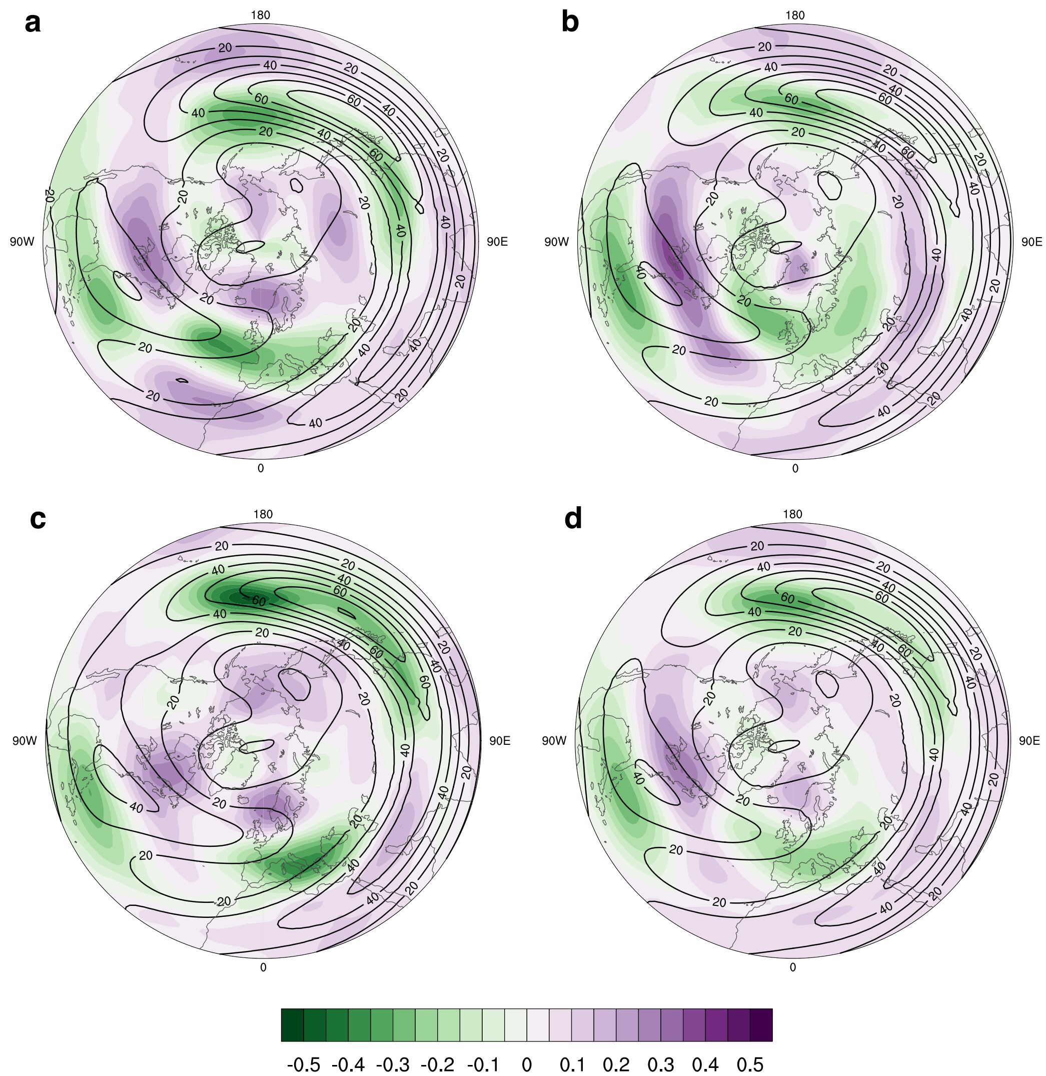

Figure 4.6: Regression coefficients of mean 200-hPa zonal wind (m/s) onto the NAM-VP Index (color shading) for the 50-year samples of a) 1951–2000, b) 2001-2050, c) 2051–2100, and d) 1951–2100. Contours show the ensemble mean time mean zonal wind at 200 hPa of the corresponding samples.

contours. Consistently, those regression maps suggest that when the NAM has a strong North Pacific center of action, the Pacific jet stream is anomalously weak and shifted southward of its mean position, especially in the jet exit region. This weakening is upstream and slightly equatorward of the NAM's North Pacific center of action (Fig. 4.1). In contrast, in the North American sector, the jet stream exhibits a northward shift when the NAM exhibits a stronger North Pacific center. Whether this variation in the jet stream is tightly related to the variability in the NAM's spatial pattern is in need of further investigation with simplified models, such as a global barotropic model (Simmons et al., 1983).

4.6 The trend in the NAM under global warming

In this section I evaluate how the anthropogenic warming affects the spatial structure of NAM in the CESM-LE. Fig. 4.7 compares the NAM-VP Index (expansion coefficients corresponding to the NAM Variability Pattern in the EOF analysis of 90 50-year samples). As shown in the figure, most ensemble members exhibit negative or near-zero index values for

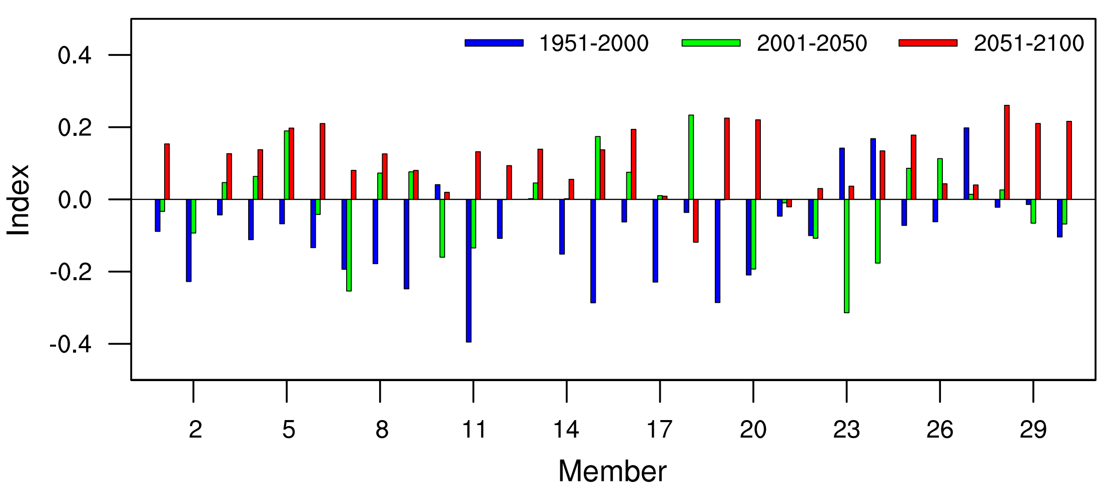

Figure 4.7: Expansion coefficients of the leading EOF of the NAM in the 90 50-year samples, i.e. the NAM-VP Index. For each ensemble member, different time periods are marked with different colors.

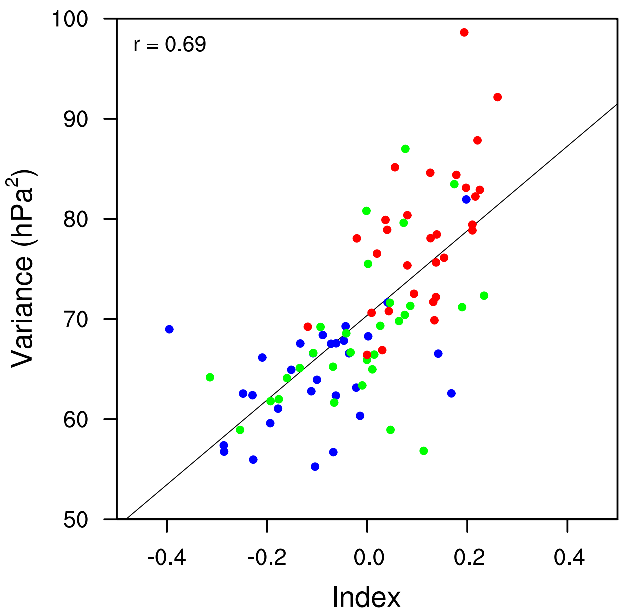

Figure 4.8: Expansion coefficients of the leading EOF of the NAM in the 90 samples (NAM-VP Index) versus the corresponding mean variance of monthly SLP anomalies in the North Pacific (the region indicated by a blue box in Fig. 4.3). As in Fig. 4.7, different time periods are marked with different colors. Blue indicates 1951–2000, green indicates 2001-2050, and red is 2051–2100. Correlation of those two variables in display is 0.69 .

the period 1951–2000, whereas for the period 2051-2100, most members exhibit positive index values. In the period of 2001–2050, positive and negative index values have a comparable frequency of occurrence.

This systematic trend in the NAM Pattern Index suggests that as global temperature rises, the North Pacific center of action of NAM becomes more prominent than it was in the historical record. However, that strengthening of NAM's Pacific center is only in the sense of increased probability. Notably, a few ensemble members exhibit a near-zero index in the period 2051–2100, and one ensemble member even exhibits a negative index.

To test whether this trend in NAM Pattern Index has a physical meaning, I compared

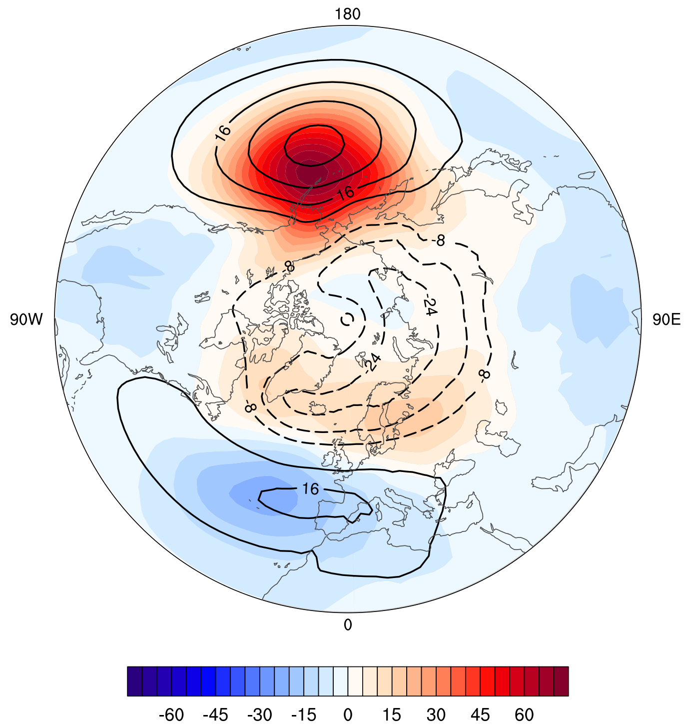

Figure 4.9: Same as Fig. 4.1 except that data from GFDL ensemble are used in the analysis.

the area-mean variance in the North Pacific (the region indicated by the blue box in Fig. 4.3) and the pattern index in Fig. 4.8, in which colors of those dots indicate different time periods. The variance of SLP* exhibits a robust correlation of 0.69 with the NAM Pattern Index, and the corresponding p-value against the hypothesis of zero-correlation is 4×10^{-14}. Clearly, when a NAM has a stronger North Pacific center of action, the corresponding variance in wintertime monthly SLP also become higher than average. More importantly, most ensemble members' variance of the period of 2051-2100 is larger than the variance of 1951–2000. Thus global warming indeed leads to more atmospheric variability in the North Pacific region.

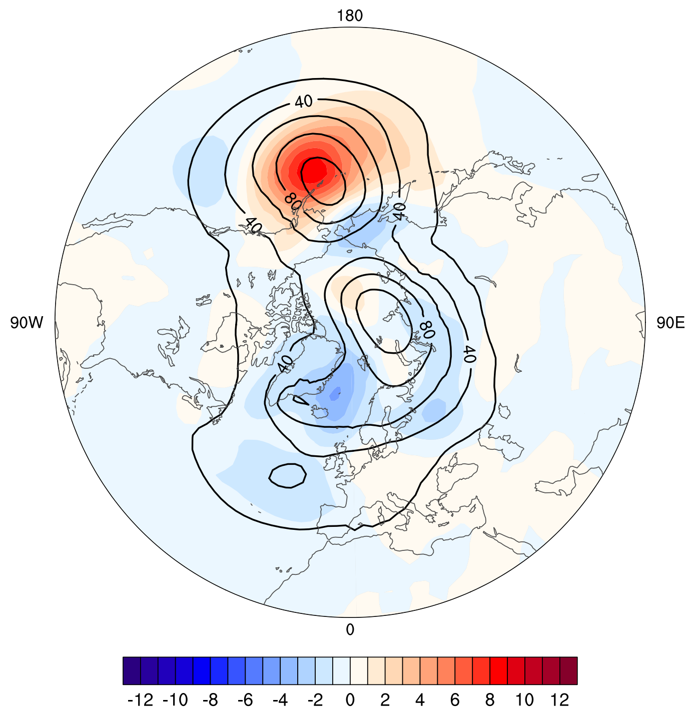

Figure 4.10: Same as Fig. 4.3 except that data from GFDL ensemble are used in the analysis.

4.7 NAM's variability in GFDL ensemble

To determine whether the results shown above are limited only in the CESM-LE simulations, I repeated some of the analysis on the 10-member ensemble based on GFDL's climate model CM2.1. Fig. 4.9 shows the averaged NAM pattern and the NAM Variability Pattern associated with the GFDL ensemble. Consistent with the NAM in CESM-LE, the main variability in NAM's spatial structure is in the North Pacific, and the Euro-Atlantic center of action of NAM slightly weakens as the North Pacific center becomes stronger. 40% of the variance in NAM's spatial structure is explained by the NAM Variability Pattern.

Figure 4.10 shows the regression map of SLP* variance onto the corresponding NAM Pattern Index in GFDL ensemble. Consistent with Fig. 4.3, it suggests that the main center

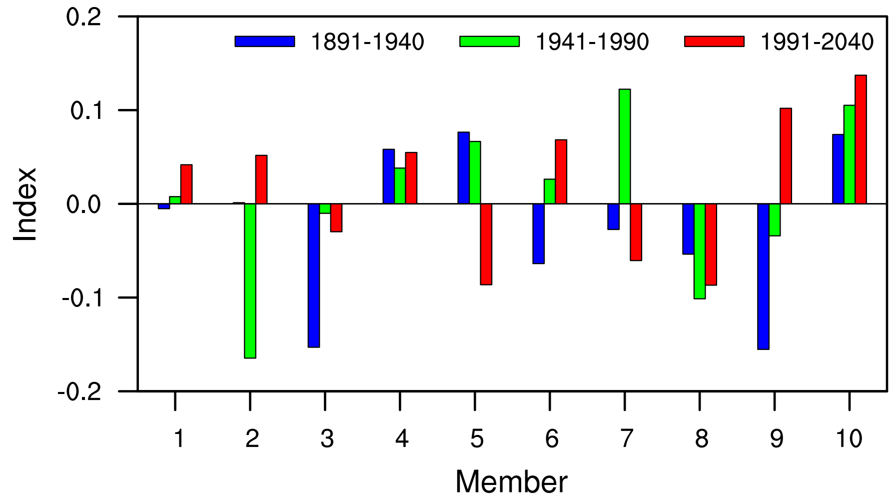

Figure 4.11: Same as Fig. 4.7 except that data from GFDL ensemble are used in the analysis.

of variance in SLP* in the Arctic and the North Pacific region. When NAM has a strong North Pacific center, the variance in the North Pacific is larger than average.

However, the trend in NAM's characteristic pattern due to global warming in the GFDL ensemble is not as prominent as in the CESM-LE simulations. One might still be able to argue that there is a trend in NAM's spatial structure, because there are more ensemble members having positive pattern index in 1991-2040 than those having positive index values in 1891-1940, and similarly, more ensemble members in 1891-1940 have negative index values than those having negative index values in 1991-2040. But these differences are much less impressive than that in the CESM-LE project. This presumably is related the small size of the GFDL ensemble, and the weaker RCP4.5 scenario of warming.

4.8 Summary and discussion

Whether NAM exhibits a real center of action over the North Pacific has been a matter of debate, which may not be resolved because of the relatively short history of hemisphericscale atmospheric data. The CESM large ensemble project provides a unique opportunity to study the atmosphere's natural variability by producing many realizations of the climate system under the same external forcing.

Different realizations and different time periods in CESM-LE exhibit quite different spatial structures in 50-year segments from CESM-LE simulations. In some segments the NAM exhibits a North Pacific center of action that is much stronger than the Euro-Atlantic center of action, whereas in some other segments of data the NAM exhibits a deep Arctic center along with weaker North Pacific and Euro-Atlantic centers that are of similar strength.

The spatial structure of NAM is well correlated with the variance of monthly SLP anomalies. In the 50-year samples in which the NAM's North Pacific center of action is anomalously strong, the variance of SLP in the North Pacific is also stronger than average. This anomalously high variance is reflected both in greater interannual variability in wintertime SLP and in greater variability in daily SLP anomalies. In the 50-year segments in which the North Pacific center of NAM is anomalously strong, the wintertime daily SLP's variance is anomalously high at time scales longer than $\sim$20 days, and stronger positive and negative pressure anomalies are observed in the corresponding PDF of daily SLP anomalies. Both of those facts suggest that the variations in NAM's spatial structure are directly associated with low frequency variability of the atmospheric circulation, which modulates higher frequency phenomena, such as synoptic eddies and blocking, rather than by directly modulating those high frequency phenomena themselves.

The variability in NAM's spatial structure exhibits a strong correlation with the position and strength of upper-level jet streams. When the NAM exhibits a strong North Pacific center of action, the upper-level jet at the North Pacific exhibits a weakening and southward shift in the region upstream of NAM's North Pacific center of action, and the jet stream over North America exhibits a northward shift meanwhile. Regression based on different time periods gives qualitatively consistent results about the relation between upper-level jet and NAM's spatial structure. However, whether there is a robust dynamical connection between them is subject to further investigations.

A puzzling result in this study is that NAM's spatial structure exhibits a significant trend under global warming in a probabilistic sense. Under RCP8.5 forcing, NAM's North Pacific center of action becomes more prominent in the data segments for 2051–2100 than in the segments for 1951-2000. However there still exist a few realizations with near-zero and negative NAM-VP Index in 2051-2100. This puzzling trend and the natural variability in NAM's spatial structure means that, if the NAM is defined on the basis of samples as short as 50 years, its pattern will be constantly changing with time as a result of internal low frequency variability and external forcing. Even in the absence of external forcing, a period of record much longer than 50 years would be required to obtain a robust definition of the NAM.

Chapter 5

Large Scale Character of an Atmosphere in Rotating Radiative-Convective Equilibrium

5.1 Introduction

As stated by Bretherton et al. (2005), radiative-convective equilibrium (RCE) in a non-rotating, horizontally homogeneous environment is a time-honored idealization for understanding the tropical atmosphere and its sensitivity to relevant forcings. Its history can be traced back to the early work by Manabe and Strickler (1964) with single column models. Modern RCE simulations employ cloud-resolving models to study a wide number of issues, including controls on the hydrological cycle (Romps, 2011), the distribution of convective mass fluxes (Tompkins and Craig, 1998), scaling laws for moist convection (Robe and Emanuel, 1996), etc.

Recently, Held and Zhao (2008) proposed RCE in a rotating environment, simulated using general circulation models (GCMs), as a useful framework for studying the tropical cyclones (TCs) produced by global models. Recent studies suggest that atmospheric resolutions in the range of 20–100 km may be sufficient to study many aspects of TCs (Zhao et al., 2009). Idealized experiments can illuminate the influence of external parameters and model assumptions on TC simulations. Rotating RCE simulations described by Held and Zhao (2008) used the column physics of GFDL's Atmospheric Model 2 (AM2) and a hydrostatic dynamical core in a doubly-periodic box. In their large 2×10^4 km square horizontally homogeneous domain with fixed sea surface temperature (SST) and uniform Coriolis parameter f, multiple TCs coexist in the equilibria reached by their simulations. Increasing SST made the number of TCs decrease in their simulations while the average intensity increased. The spacing between TCs was found to be inversely proportional to f.

A new variant of rotating RCE was developed by Khairoutdinov and Emanuel (2013) using a cloud-resolving model in a small 2300 km square domain. In order to allow multiple TCs to coexist in their small domain, they artificially increased the Coriolis parameter from typical values in the tropics by about one order of magnitude. Besides finding similar dependence of TC size and intensity on SST, they also found that the outflow temperature of TC's remains relatively invariant with SST, consistent with the Fixed Anvil Temperature (FAT) hypothesis proposed by Hartmann and Larson (2002) for tropical deep convection.

However, for realistic values of the Coriolis parameter, cloud resolving resolution simulations in a small domain usually only allow one TC to develop (e.g. Nolan et al., 2007; Nolan and Rappin, 2008). The small domain size is a strong constraint on simulated TCs and the horizontal-mean equilibrium state they help to create. Indeed, Zhou et al. (2013) explored the dependence of the equilibrium state upon domain size using a model similar to Held and Zhao (2008). They found that as domain size increases, the equilibrium evolves through four regimes: a single tropical depression, an intermittent tropical cyclone with widely varying intensity, a single sustained storm, and finally multiple storms.

In this paper I document the major characteristics of the large scale flow in rotating RCE using a model similar to that of Held and Zhao (2008), but on a spherical earth. Such experiments help bridge between the TCs in even more idealized simulations and real world simulations.

Our simulation is not the first to explore RCE on a rotating sphere, but probably due to inadequate horizontal resolution, TCs were absent in earlier simulations of rotating RCE on a sphere. Previous work focused on an ITCZ that forms spontaneously in rotating RCE on a sphere. Sumi (1992) described how the ITCZ forms with particular emphasis on the evolution of convective activity. Kirtman and Schneider (2000) provided more detailed analysis of the general circulation in similar experiments, pointing out that the easterlies within the ITCZ and westerlies in the subtropics of the aquaplanet in rotating RCE implied poleward transport of angular momentum in those simulations. Such an ITCZ also exists in our simulations and will be discussed later in the paper.

Our analysis and discussion will primarily focus on the characteristics of atmospheric dynamics associated with TC-like vortices (TCLVs) in rotating RCE. General circulation features of the simulated ITCZ will also be discussed and compared with the previous literature, so as to provide a complete picture of the atmospheric motions in rotating RCE on a sphere.

5.2 Model information

The GCM used in this study is the global atmosphere model AM2.1, developed by the Geophysical Fluid Dynamics Laboratory (GFDL) (GFDL Global Atmospheric Model Development Team, 2004). Standard physics schemes and parameters of AM2.1 are adopted in our simulations unless otherwise specified in the following text. A brief description of AM2.1 model components is given below. Readers interested in details of AM2.1 physics schemes or dynamics are referred to GFDL Global Atmospheric Model Development Team (2004) and references therein.

AM2.1 has a finite-volume dynamical core on a latitude-longitude grid (Lin, 2004), which in our simulations has a resolution of 1° latitude by 1.25° longitude, with 24 vertical levels. The whole planet is covered by ocean with a fixed uniform sea surface temperature (SST) of 300 K.

As detailed in GFDL Global Atmospheric Model Development Team (2004), grid-resolved clouds and precipitation in AM2.1 are parameterized with the aid of prognostic variables for the cloud fraction and the specific humidities of cloud liquid water and cloud ice. Grid-scale fluxes of rain and snow are computed diagnostically from these prognostic fields (Rotstayn, 1997; Rotstayn et al., 2000). Cumulus convection is represented by the Relaxed Arakawa-Schubert formulation of Moorthi and Suarez (1992).

The longwave radiation code of AM2.1 accounts for the absorption and emission by the principal gases in the atmosphere, including H_2O, CO_2, O_3, N_2O, CH_4, and halocarbons. The concentrations of those gases are fixed at climatological means, and the radiative effects of aerosols are not included in these simulations. Solar radiation is also eliminated.

I first run a simulation starting from the observed atmospheric state of the Earth on a random day for 3 years, during which an equilibrium state is already achieved. Yet in order to make sure this equilibrium state is not directly influenced by its particular initial condition, I take the last month's globally averaged profiles of temperature and moisture and global mean surface pressure to create a new initial condition, in which wind velocity is set to zero everywhere. Then I run the model for another 3 years, and discard the first two years as spinup. As expected, this new simulation reaches the same equilibrium state as before in less than one year. Our analysis below uses averages over the last year's data of this simulation unless otherwise specified.

5.3 TC-like vortices

The most prominent feature of the atmospheric motions in the rotating-RCE state is the existence of many TC-like vortices (TCLVs) throughout the extratropical atmosphere, at latitudes roughly poleward of 10° (Fig. 5.1). The vortices in the northern (southern) hemisphere in general move slowly northwestward (southwestward), and many of them have very long lifetimes.

I identify and track individual TCLVs in the simulation using 6 hourly data of the 850 hPa relative vorticity field. All data are smoothed horizontally with a Gaussian filter first to remove small scale "noise". Each individual TC-like vortex in the northern (southern) hemisphere is defined as a continuous region with positive (negative) vorticity and minimum value greater than $3\times10^{-5}\,\mathrm{s}^{-1}$ (less than $-3\times10^{-5}\,\mathrm{s}^{-1}$). By this standard, the temporally averaged number of TCLVs on each hemisphere is about 36. The center of each vortex is calculated as the vorticity-weighted mean coordinate of this positive (negative) vorticity patch, while its "radius" r is defined as the maximum distance between its center and border. Finally if

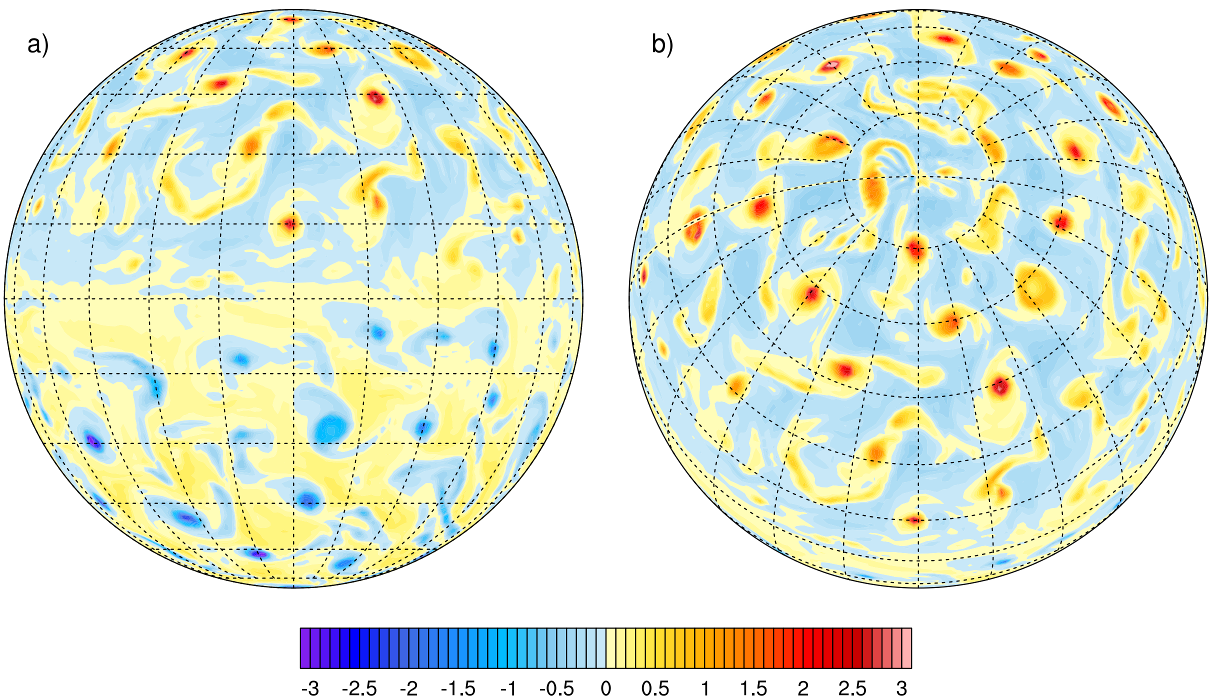

Figure 5.1: Instantaneous distribution of relative vorticity ($10^{-4}\,\mathrm{s}^{-1}$) at 850 hPa level. a) and b) show the same field viewed from different angles.

vortex j among all vortices at time step $n+1$ is closest to vortex i at the 6-hour earlier time step n, and if the distance between their centers is less than both their diameters $2r_i$ and $2r_j$, I merge vortex j and i into a single vortex, which I track at later time steps.

In the Northern Hemisphere, most of the trajectories found by the above procedure show a southeast-northwest orientation, especially the longer ones. Fig. 5.2 shows the trajectories of vortices that moved more than 45° latitude in the meridional direction. While some of those trajectories are wobbling or cycloidal, they all move poleward and westward in the end. There are 176 such long trajectories globally in the one year simulation data. Their average duration is 60 days, and the longest one is 120 days. Fig. 5.3 shows the averaged trajectory of 57 TCLVs from both hemispheres starting from latitudes lower than 15° and

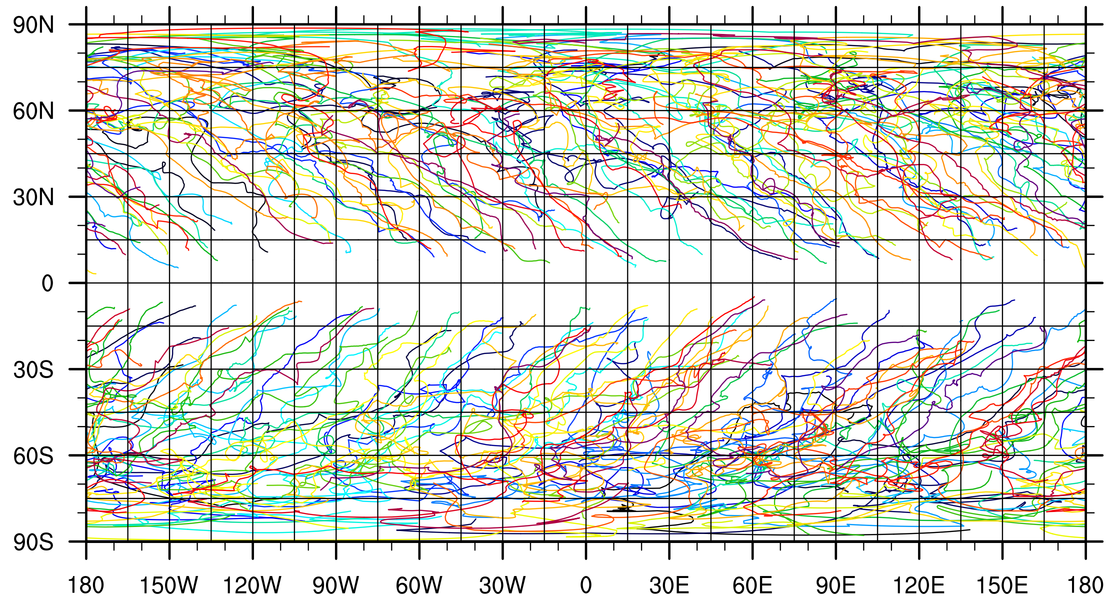

Figure 5.2: Trajectories of vortices that moved more than 45° latitude in the meridional direction.

ending at least 60° poleward of their initial positions. Shorter trajectories are discarded for ease in calculating the mean trajectory. At its poleward edge, the mean trajectory breaks up into little pieces, because TCLVs tend to swirl in place when they are near the pole and thus lose consistency in their direction of motion.

The poleward and westward movement of TCLVs can be explained by the beta effect on tropical cyclone motion (beta drift) (e.g. Chan and Williams, 1987; Wang and Li, 1992; Li and Wang, 1994; Wang and Holland, 1996). An initially symmetric vortex in the Earth's vorticity gradient will develop a pair of counter-rotating gyres due to Rossby wave dispersion. These asymmetric gyres induce a relative flow across the vortex core causing it to propagate poleward and westward (Wang and Holland, 1996). Li and Wang (1994) found that depending on initial vortex structure, the vortex may follow a variety of tracks ranging from a quasi-steady displacement to a wobbling or a cycloidal track due to the evolution of

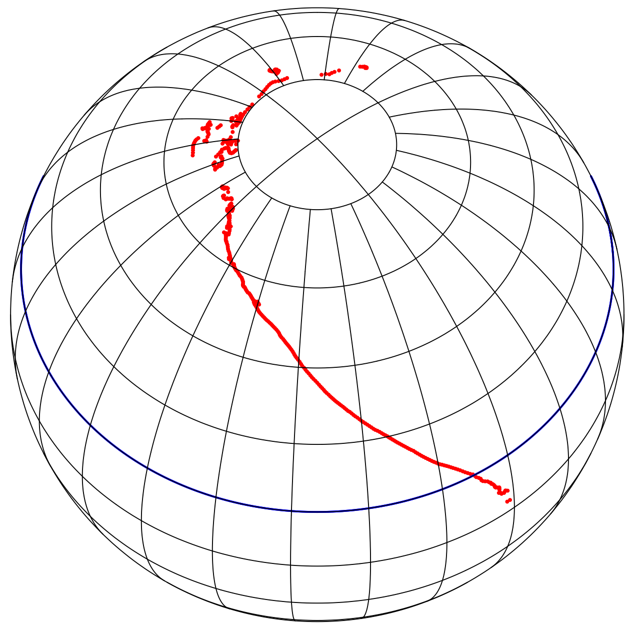

Figure 5.3: Averaged trajectory of long-lived vortices starting from latitudes lower than 15° and ending at least 60° poleward of their initial positions. The latitude circle in blue indicates 15°N.

the asymmetric gyres. This is consistent with the complex details of the TCLV tracks in Fig. 5.2.

5.4 Energy spectrum

Driven by convective instability and constrained by the rotation of the planet, the large scale circulation in rotating RCE is ultimately a problem in geostrophic turbulence. In this section, I examine the energy spectrum in this light. In our simulation, the barotropic circulation, which is defined as the vertically averaged component of atmospheric motions, contains about 80% of the total available potential energy (APE) and about 75% of the total kinetic energy (KE) of the circulation. Hence, I will focus hereafter on the barotropic energy spectrum.

Our calculation of KE and APE spectra follow the formulation of Augier and Lindborg (2013). The globally integrated barotropic KE and APE are:

$$E_K = \frac{p_s - p_t}{g} \int \left(\frac{u_m^2 + v_m^2}{2} \right) a^2 d\Omega \,, \tag{5.1}$$

$$E_A = \frac{p_s - p_t}{g} \int \left(\gamma \frac{\theta'^2_m}{2} \right) a^2 d\Omega \,, \tag{5.2}$$

respectively. These are areal integrals around the globe, where $d\Omega$ is an infinitesimal element of solid angle and a is the radius of the Earth. p_s and p_t are the mean surface and tropopause pressure, where $p_t \approx 250\,\mathrm{hPa}$ in our simulations. u_m and v_m are the barotropic velocity components, while θ'_m is the barotropic component of the deviation of potential temperature from its mean profile. Strictly speaking, γ, which is related to the mean stratification, is a function of pressure. But in our simulations, it is nearly a constant in the free troposphere, thus I use its mean value, $8\,\mathrm{J\,kg^{-1}\,K^{-2}}$, in our calculation. The globally integrated barotropic KE and APE are 7.2×10^{19} J and 5.2×10^{19} J respectively in our simulation.

Similar to Augier and Lindborg (2013), I calculate the energy spectrum of the global atmosphere using spherical harmonics Y_{lm}. The spectral components of KE and APE are defined as follows,

$$E_K^{lm} = \frac{a^4}{2l(l+1)} \left(\hat{\zeta}_{lm} \hat{\zeta}^*_{lm} + \hat{\mathcal{D}}_{lm} \hat{\mathcal{D}}^*_{lm} \right) \,, \tag{5.3}$$

$$E_A^{lm} = \frac{a^2 \gamma}{2} \hat{\theta}_{lm} \hat{\theta}^*_{lm} \,, \tag{5.4}$$

where $\hat{\zeta}_{lm}$, $\hat{\mathcal{D}}_{lm}$, $\hat{\theta}_{lm}$ are the spectral coefficients of vorticity, divergence, and potential temperature disturbance respectively. Since the total wavenumber of spherical harmonics is $k = \sqrt{l(l+1)}/a$, I further sum up spectral functions with respect to zonal wavenumber to obtain the energy spectra with respect to total wave number:

$$E_K^l = \sum_{|m| \le l} E_K^{lm} \,, \tag{5.5}$$

$$E_A^l = \sum_{|m| \le l} E_A^{lm} \,. \tag{5.6}$$

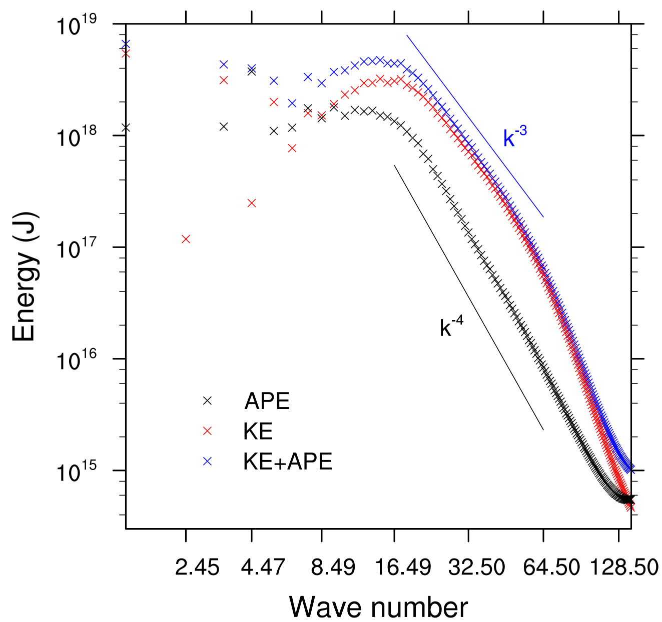

Figure 5.4: Energy spectrum of globally integrated barotropic KE, APE, and KE+APE.

Figure 5.4 shows the spectrum of KE, APE, and KE + APE. The spectrum of total energy (KE + APE) has a k^{-3} spectral slope in intermediate wavenumbers, and drops off more steeply at large wavenumbers. Throughout this range, it is dominated by KE. The APE spectrum, which is roughly only 1/5 of the KE spectrum in strength at intermediate wavenumbers, has a k^{-4} spectral slope. The spectrum of both KE and APE is flat for $l \leq 16$ ($k < k_c = 16.5/a$). This cutoff scale corresponds to a half-wavelength of 1200 km, which is approximately equal to the midlatitude dry deformation radius, $L_d = NH/f_0 \approx 1100\,\mathrm{km}$, where $N^2 = 1.25 \times 10^{-4}\,\mathrm{s}^{-2}$, $H = 10\,\mathrm{km}$ for our simulation.

Held and Zhao (2008) suggested that the spacing between vortices may scale with L_d, consistent with the cutoff wavenumber in our energy spectra. In our simulations, N and H are nearly uniform around the globe so L_d is proportional to $1/f$. The TCLV spacing in each latitude band based on the number of vortices per unit area can be calculated. I divide the

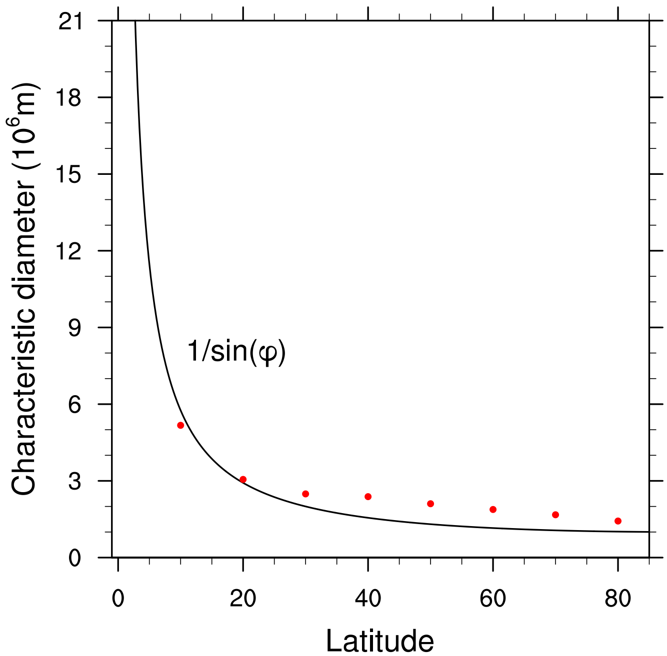

Figure 5.5: Characteristic diameters of influence of vortices *vs* latitude.

whole planet into 15° wide latitude bands, and denote the time mean of TC numbers in a given band by $\overline{N}$. The characteristic diameter of influence of TCLVs in each band is defined by $L_v = 2\sqrt{S_\varphi/(\pi\overline{N})}$, where S_φ is the area of the latitude band centered at latitude φ.

The characteristic diameters of influence of TCLVs at different latitude bands are plotted in Fig. 5.5 as red dots. They are roughly proportional to the change in $1/f$ and hence L_d with respect to latitude. In the extratropics, L_v is approximately $2L_d$.

5.5 Scale of energy production

The above characteristics of the atmosphere in rotating RCE, namely the k^{-3} spectral slope and the spectral peak at the scale of the deformation radius, are surprisingly similar to observations of the Earth's atmosphere. At scales smaller than the deformation radius, the energy spectrum of the Earth's atmosphere follows an approximate -3 law (e.g. Gage and Nastrom, 1986); At scales larger than the deformation radius the spectrum is somewhat flat and uneven, with no distinct slope (e.g. Augier and Lindborg, 2013).

In the case of the Earth's atmosphere, the spectral slope changes near the scale of the deformation radius because L_d is the scale at which energy is injected into the barotropic mode through processes associated with baroclinic instability (Salmon, 1978, 1980; Zurita-Gotor and Vallis, 2009). A k^{-3} spectral slope forms at scales smaller than L_d as a result of the downscale enstrophy cascade in two dimensional geostrophic turbulence.

In rotating RCE, energy is also injected into barotropic eddy motions at the scale L_d, but via a totally different mechanism involving latent heating, as I now show. I calculate the power spectrum of APE generation rate due to diabatic heating in our simulation. The

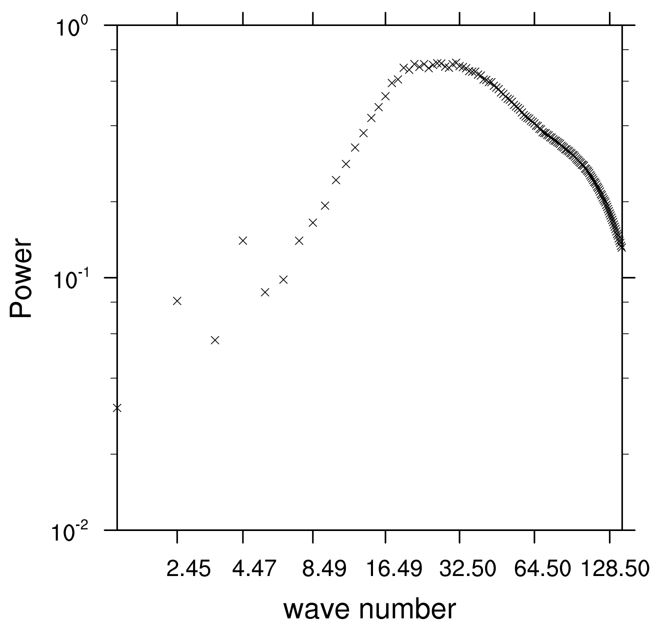

Figure 5.6: Power spectrum of vertically integrated APE generation rate due to diabatic heating.

APE generated by diabatic heating at a grid point is (Augier and Lindborg, 2013),

$$G(p, \varphi, \lambda) = \gamma \overline{\theta' Q'_\theta}\,, \tag{5.7}$$

where θ' is potential temperature fluctuation; Q_θ is the tendency of potential temperature due to diabatic heating (radiation and latent heat release), and Q'_θ is the deviation from its time mean; p, φ, λ are pressure, latitude, and longitude respectively. By integrating G vertically and using spherical harmonics, I get the power spectrum of APE generation rate due to diabatic heating (Fig. 5.6).

Comparison of Fig. 5.5 and Fig. 5.6 tells us that most of the diabatic heating term, which

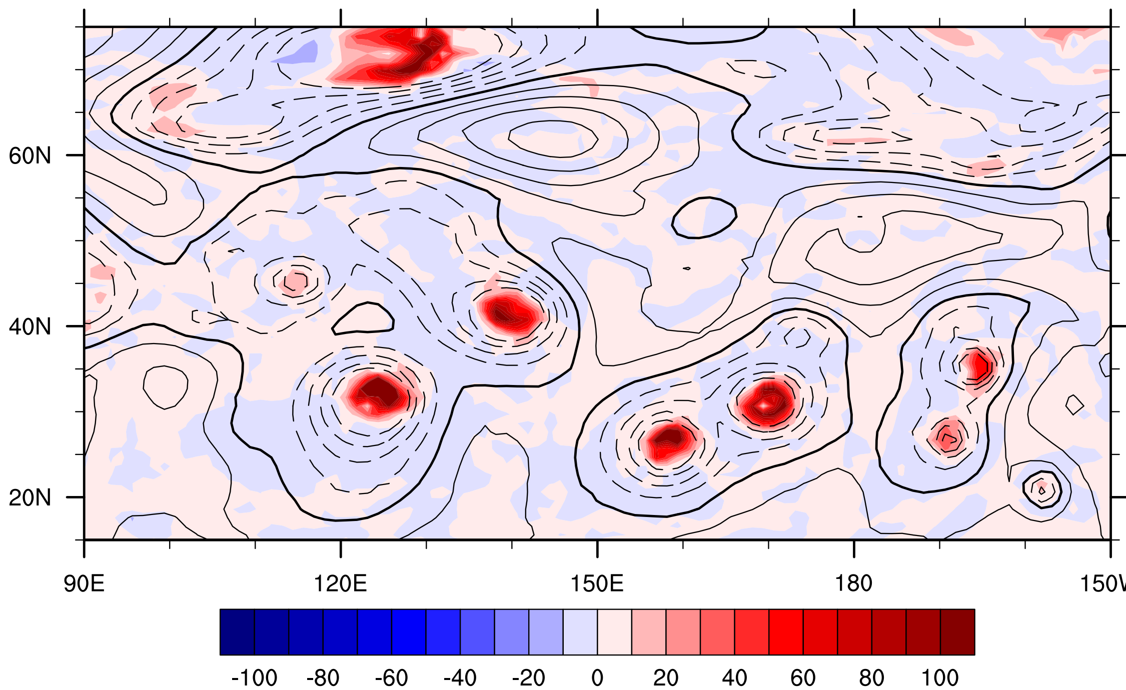

Figure 5.7: A snapshot of vertically integrated APE generation rate (color, in $\mathrm{W\,m^{-2}}$) due to diabatic heating, and the corresponding surface pressure anomaly (contours with 2 hPa intervals). The thick solid contour is indicating zero, negative pressure anomaly is contoured in dash lines, and positive values are in solid thin lines.

is mainly due to latent heat release, concentrates at scales slightly smaller than the scale of vortices, which is not surprising, since the diabatic heating perturbations are concentrated in the cores of the vortices. APE generation in the simulations is stronger in the upper troposphere than at lower levels, and maximizes near the 300 hPa pressure level.

Figure 5.7 shows an instantaneous distribution of vertically integrated G, overlaid with contours of surface pressure anomaly. A mature TCLV has strong production of APE by diabatic heating right above its surface low pressure center, collocated with the surface vorticity maximum, and a broader region of very weak APE dissipation surrounds it.

Therefore, the atmosphere in rotating RCE has maximum energy production at scales comparable to the deformation radius, and this is why it has an energy spectrum similar to that of the Earth's atmosphere.

One may ask why the spacing of TCLVs, and thus the scale of its energy production, is not significantly smaller, or larger, than the scale of the deformation radius. The growth of TCLVs at small scales may be explained by the self-aggregation of convection (Bretherton et al., 2005; Muller and Held, 2012). Three-dimensional cloud-resolving simulations by Bretherton et al. (2005) show that an upgradient transport of moist static energy exists in the aggregated state, with moist static energy transported from low-energy (dry) to high-energy (moist) regions.

Figure 5.8 shows the development of precipitation and water vapor path (WVP) in the first 16 days of our simulation. One can find two initial growth modes in Fig. 5.8. One originates from a few strong WVP anomalies that are already apparent at Day 2, the other develops from random convection that becomes prominent a few days later. Both modes grow upscale with time, and the overall distribution of WVP and precipitation becomes better organized at Day 16. The evolution of the second mode suggests that random convection initially at very small scales can self-aggregate to the deformation radius, hence in the equilibrium of rotating RCE, TCLVs will grow to at least this scale.

The strong initial WVP anomalies of the first mode grow to large vortices at Day 10. But at Day 13 and 16, those large vortices split into smaller ones, suggesting that TCLVs of

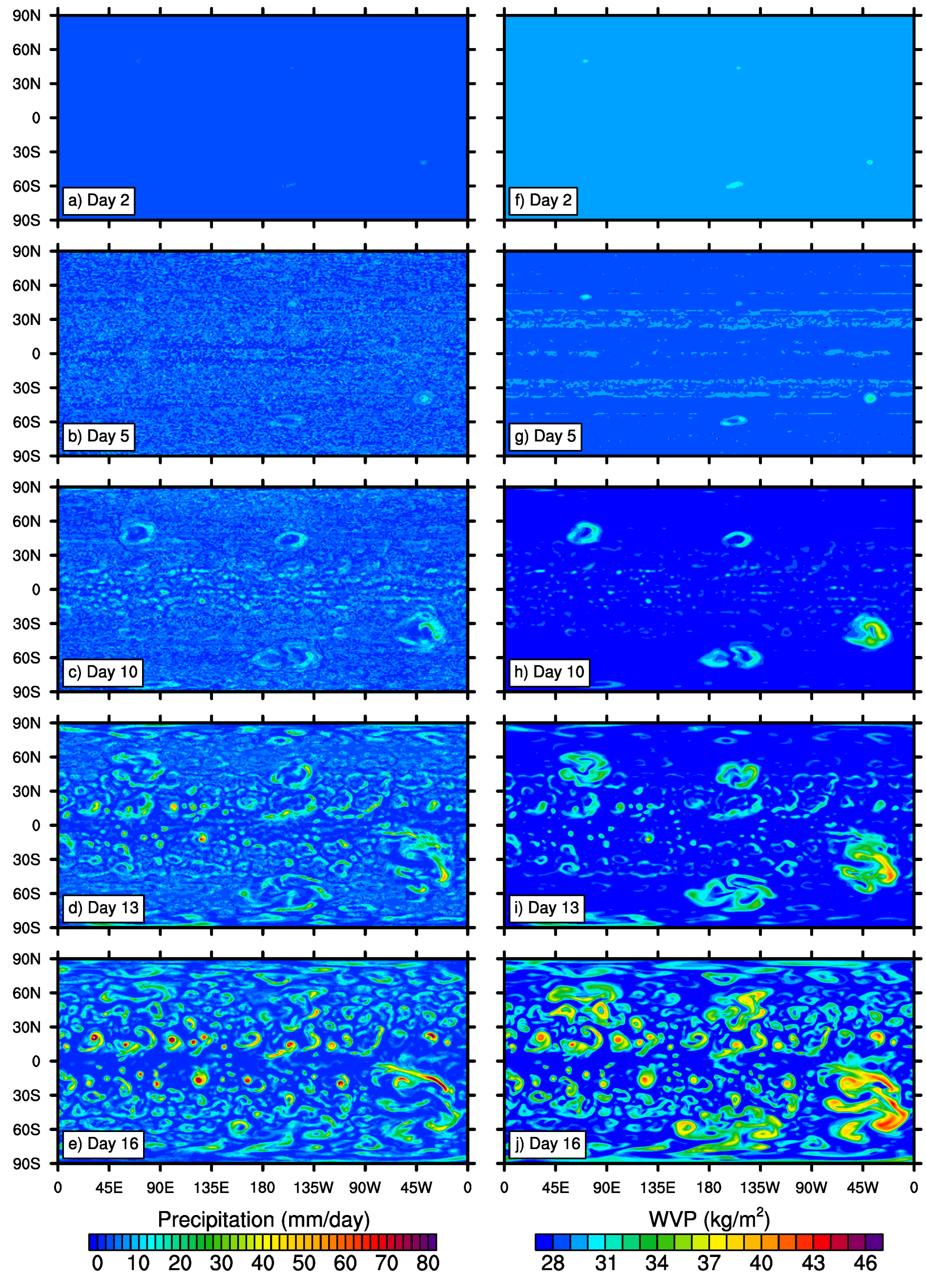

Figure 5.8: Development of daily mean precipitation (left panel a–e) and water vapor path (WVP, right panel f–j) in the first 16 days of the simulation.

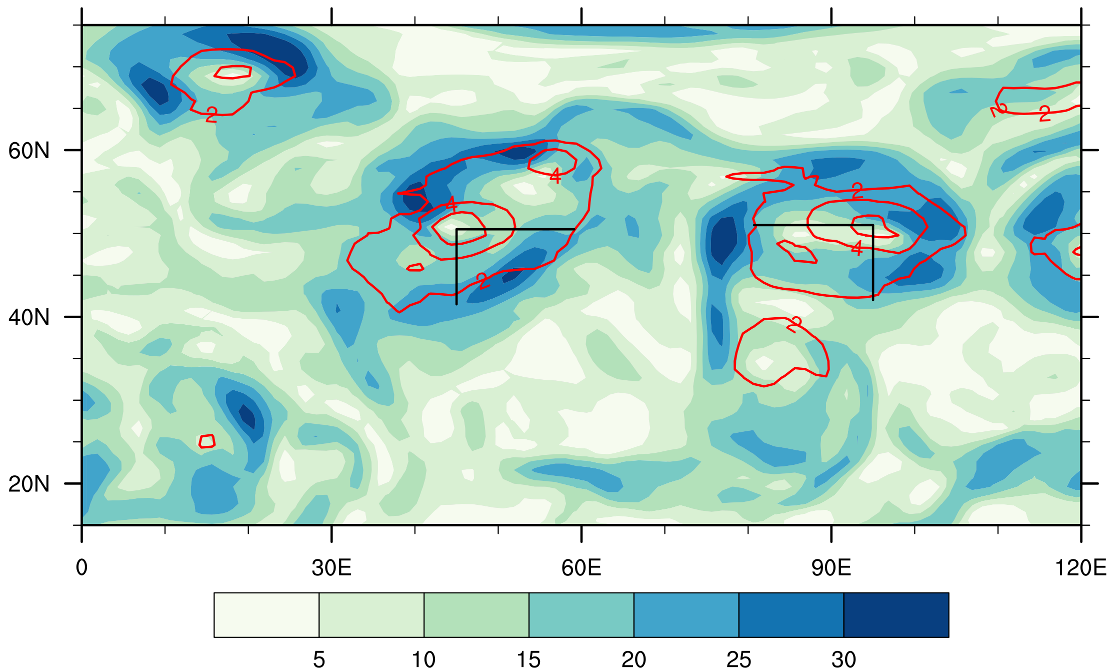

Figure 5.9: A snapshot of the differential wind speed between 250 hPa and 850 hPa (color, in $\mathrm{m\,s^{-1}}$) and anomalously temperature field at 500 hPa (contours with 2 K intervals). Black lines are 1000 km long, drawn for indicating the length scale in north-south or east-west direction of the map.

their size are not stable. I now argue that baroclinic instability may be the cause.

Figure 5.9 shows an instantaneous distribution of the differential wind speed between 250 hPa and 850 hPa, $|\mathbf{V}_{250} - \mathbf{V}_{850}|$, and the anomalous temperature field at 500 hPa. The horizontal temperature gradient between the warm cores of TCLVs and the surrounding regions is $\sim$ 5 K per 10° of longitude/latitude, which is comparable with the meridional temperature gradient of Earth's atmosphere. The temperature gradient is weaker at lower levels, but at 850 hPa level, it is still greater than 3 K per 10° of longitude/latitude. Thermal wind balance requires a vertical wind shear between upper and lower troposphere levels that can exceed $20\,\mathrm{m\,s^{-1}}$, which is also of comparable size to vertical wind shear at midlatitudes of the Earth.

Therefore, it is plausible to think baroclinic instability could occur in rotating RCE *if* there were TCLVs of size significantly larger than the deformation radius L_d. Baroclinic instability has a shortwave cutoff near the deformation radius, which is $2.6L_d$ in the classic Eady problem (Vallis, 2006, Ch. 6). Baroclinic instability does not disturb the growth of TCLVs of scales smaller than L_d due to self-aggregation of convection. But further growth of TCLVs past scales around L_d could be constrained by baroclinic instability.

5.6 Tropical circulation in rotating RCE

Another interesting aspect of the large scale flow in rotating RCE is the existence of a pair of weak "Hadley cells" in the mass stream function of the zonal mean circulation (Fig. 5.10),

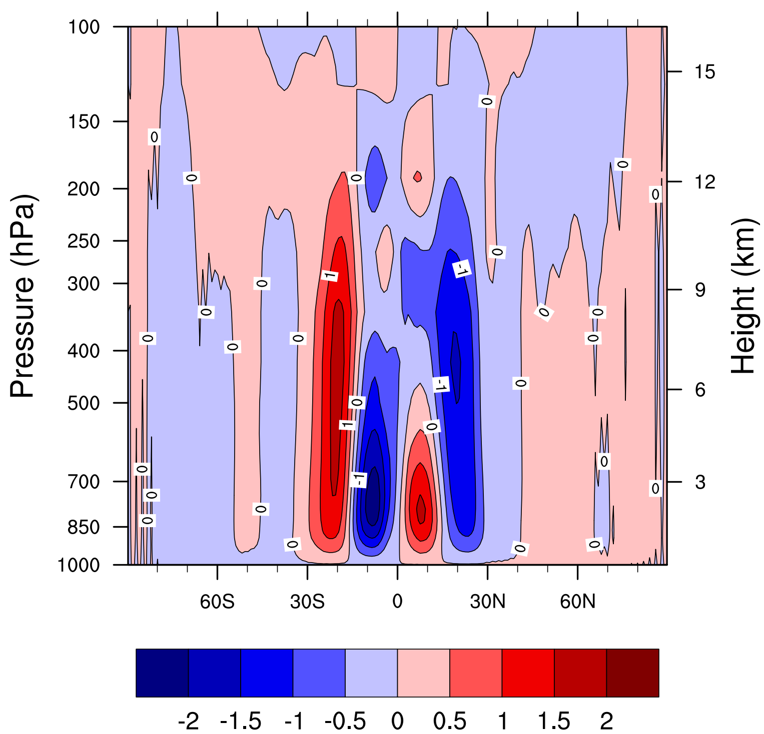

Figure 5.10: Mass stream function of the zonal mean circulation. The unit of contours is $10^{10}\,\mathrm{kg\,s^{-1}}$.

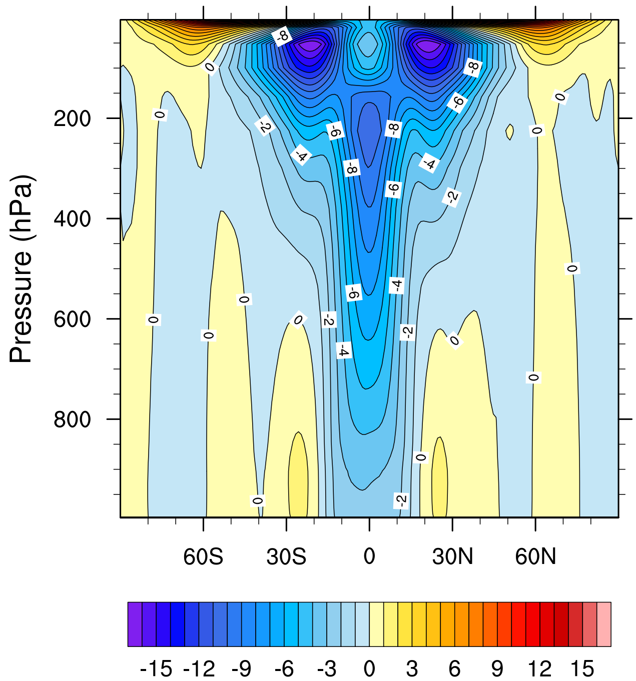

Figure 5.11: Zonal mean zonal wind in $\mathrm{m\,s^{-1}}$.

accompanied by Ferrel cell-like circulations in the subtropical region. The zonal wind field (Fig. 5.11) is dominated by upper tropospheric easterlies extending into the subtropics in the stratosphere, with weak subtropical westerlies near the surface.

Previous GCM simulations of rotating RCE have also been found to develop a Hadley circulation. The weak Hadley circulation in our simulation is very similar to the one found in one experiment of Kirtman and Schneider (2000) (see their Fig. 7), in which an AGCM is coupled to a mixed layer ocean model of constant 50 m depth, and the incident solar flux is prescribed to be constant globally. This similarity suggests that the absence of incident solar radiation and a coupled mixed layer ocean are not crucial in determining the general characteristics of the large scale circulation in a rotating RCE state.

The zonal-mean precipitation (not shown) has weak minima of about 4.7 mm/day in the

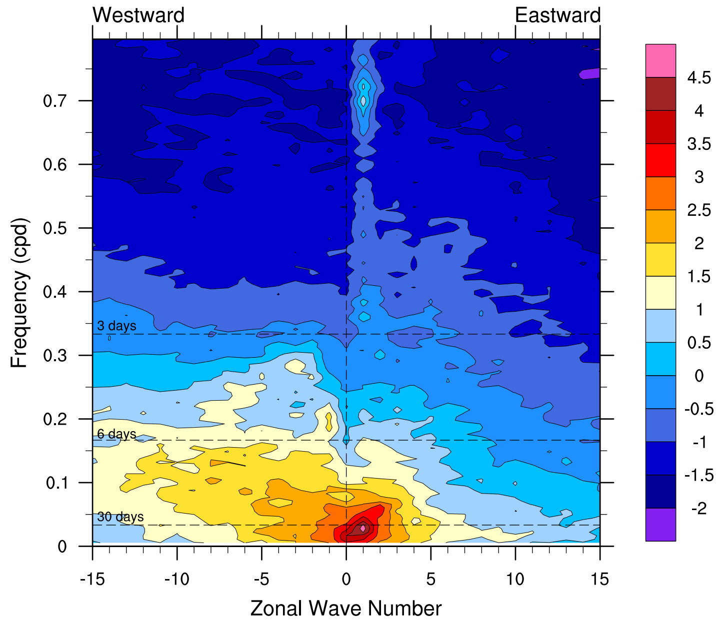

Figure 5.12: The symmetric component of the wavenumber-frequency power spectrum of surface pressure between 15°S and 15°N.

10 degree bands around 15°N and 15°S, compared to about 5.7 mm/day poleward to 25° latitude and near the equator. This contrast is similar to the aforementioned simulation by Kirtman and Schneider, but the overall precipitation is higher because the radiative cooling of the atmosphere is stronger due to the lack of shortwave absorption in our nocturnal simulations.

An eastward propagating convectively-coupled equatorial Kelvin wave develops at the equator. The signal is most prominent in surface pressure field, which shows slowly eastward propagating high and low anomalies tied to anomalously low and high precipitation, respectively. Fig. 5.12 plots the symmetric component of the power spectrum of surface pressure between 15°S and 15°N in wavenumber-frequency domain, following the approach described by Wheeler and Kiladis (1999). A Kelvin wave-like mode with wavenumber 1 and a period of about 30 days is prominent. I did not normalize the spectrum by its “background power spectrum", although doing so would not undermine the importance of this wavenumber-1 signal. This eastward propagating wavenumber-1 mode shares a similar period with the Madden-Julian Oscillation (MJO) (Madden and Julian, 1972, 1994), though it may be simply a convectively coupled Kelvin wave signal. Perhaps somewhat surprisingly, if one keeps the deep tropical SST with zero gradient and add realistic extratropical meridional gradient in SST, the MJO-like mode still exists and share similar large scale structures with this one in rotating RCE.

5.7 Momentum transport and the Hadley circulation

As Kirtman and Schneider (2000) documented, the formation of tropical easterlies and subtropical westerlies implies a net poleward transport of angular momentum in rotating RCE. They speculated that the poleward transport of angular momentum was accomplished by large-scale zonally asymmetric convective events, and tested that by conducting a simulation with their GCM truncated to be zonally symmetric. However, in the zonally symmetric model, they still got an ITCZ, which transited between 20°N and 20°S with a 22-month period, and the angular momentum transport associated with this ITCZ was accomplished by eddies rather than the mean flow.

The results of Kirtman and Schneider (2000) highlighted the role of eddies in maintaining the Hadley circulation in rotating RCE. The zonally averaged and vertically integrated zonal momentum equation may be written as

$$\begin{aligned}\int \frac{\partial [u]}{\partial t}\frac{dp}{g} &= \int [v]\left(f+[\zeta]\right)\frac{dp}{g} - \int \frac{1}{a\cos^2\theta}\frac{\partial}{\partial\theta}\left(\cos^2\theta[u'v']\right)\frac{dp}{g} + \tau_x \\ &= \int [v]f\frac{dp}{g} + \int [v][\zeta]\frac{dp}{g} + \int M\frac{dp}{g} + \tau_x,\end{aligned} \tag{5.8}$$

where the square brackets represent zonal averages, and prime denotes the deviation from zonal means. M denotes the convergence of zonal momentum transport of eddies. τ_x is surface wind stress in zonal direction.

In (5.8), the $[v]f$ integral disappears if I average the equation in time, because of mass conservation with every latitude circle in the steady state. So in rotating RCE, only the last three term can contribute to the meridional transport of momentum. Taking simulation data between 5°S and 5°N, I can calculate each term in (5.8) and their time averages, so as to estimate the importance of each term in maintaining the Hadley circulation in rotating RCE. Normalizing them by surface pressure, the time averages are -1.8×10^{-4}, -1.1×10^{-2}, -0.19, $0.20\,\mathrm{m\,s^{-1}\,day^{-1}}$ for each of the four terms on the right side of (5.8) respectively. This confirms that the easterlies of the Hadley circulation in rotating RCE are driven by eddies. The contribution from mean circulation due to the integral of $[v][\zeta]$ is much smaller than eddy contribution since u' and v' are often significantly larger than $[u]$ and $[v]$.

Why do spontaneously generated convective vortices generate a momentum flux diverging away from the equator? This may be understood as a result of the strong vorticity stirring in the extratropics, but not near the equator, due to TCLVs, following Ch. 12.1.2.III of Vallis (2006), which produces net wave activity flux into the tropics, and momentum flux out of it. Since the horizontal winds in TCLVs have a strong barotropic component, and (5.8) is vertically-averaged, I idealize the flow to be barotropic. Kinematically, the momentum flux convergence is equal to the northward vorticity flux,

$$M = -\frac{1}{a\cos^2\theta}\frac{\partial}{\partial\theta}\left(\cos^2\theta[u'v']\right) = [v'\zeta']\,. \tag{5.9}$$

Using a barotropic vorticity equation with sources F_ζ and sinks D_ζ, linearized about a mean flow with a positive meridional absolute vorticity gradient, $\Lambda = \beta - \partial^2[u]/\partial y^2$, Vallis formulates an pseudomomentum equation for Rossby wave activity density (which is proportional to vorticity variance). In steady state, it takes the following form,

$$[v'\zeta'] = \frac{1}{\Lambda}\left([\zeta' F'_\zeta] - [\zeta' D'_\zeta]\right)\,. \tag{5.10}$$

The eddy vorticity flux $[v'\zeta']$ is determined by the right-hand side of (5.10), which vanishes if the equation is integrated over latitude. Since there is stronger vorticity stirring by TCLVs in the extratropics than near the equator, the vorticity variance source should be larger there, while the sink due to dissipation may extend further into the equatorial belt. Hence, $[v'\zeta']$ is positive in the extratropics and negative within the tropics, which means there must be momentum flux convergence in the extratropics and divergence near the equator. This argument also applies to the eddy momentum transport into the eddy-driven jets on the real Earth. Its validity for the rotating RCE case is still somewhat uncertain, since it relies on linear wave arguments based on excitation of Rossby waves in the vorticity stirring region, which propagate into the equatorial region before they dissipate, while highly nonlinear TCLVs dominate the flow at all latitudes in rotating RCE. Hence, a northward flux of vorticity variance in the TCLVs could also contribute to (5.10).

The role of eddy momentum fluxes in inducing the Hadley circulation can be clearly seen

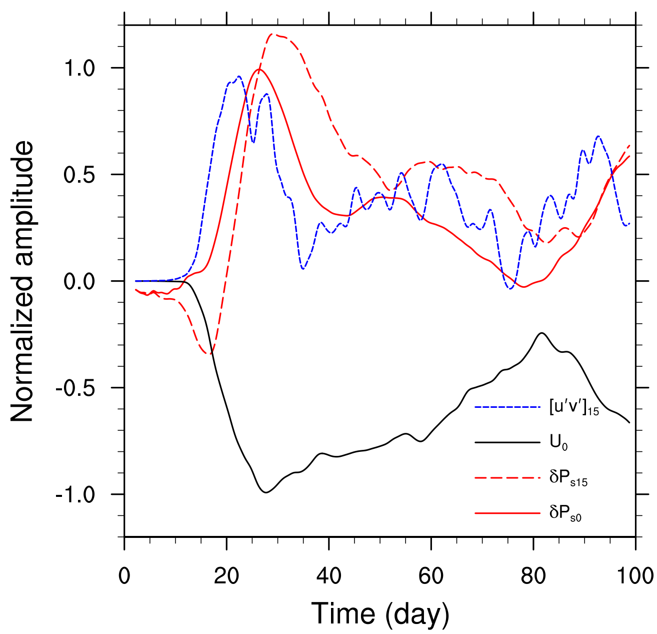

Figure 5.13: Vertically averaged zonal mean zonal wind (U_0) at the equator, and zonal mean surface pressure anomalies (δP_{s0} and δP_{s15}) at the equator and 15°N. The vertically averaged zonal mean eddy momentum flux at 15°N ($[u'v']_{15}$) is also plotted. The numbers in subscripts indicate latitudes. Surface pressure anomaly is the deviation of surface pressure from the globally uniform initial value. U_0 is normalized by $\max(|U_0|) = 9.2\,\mathrm{m\,s^{-1}}$, and δP_{s0} and δP_{s15} are normalized by $\max(\delta P_{s0}) = 4.0\,\mathrm{hPa}$ for the purpose of plotting.

from the initial spinup of rotating RCE from a state of rest. Fig. 5.13 shows the time series of vertically averaged zonal mean zonal wind and zonal mean surface pressure fluctuation at 0° and 15°N, together with that of the vertically averaged zonal mean eddy momentum flux at 15°N, in the first 100 days of the simulation.

Prior to about Day 10, the zonal mean variables have not yet changed much. In this stage eddies are developing but are not yet well formed. At about Day 10, eddy momentum flux at 15°N starts to increase. Momentum flux divergence accelerates equatorial easterly. The momentum fluxes maximize at 20 days before settling back down to an irregular statistical steady state, and the equatorial zonal winds maximize about five days later. The surface pressure field gestrophically adjusts to support the evolving wind field. The pressure rises over the tropics and lowers over the poles to support the developing subtropical westerlies being accelerated by eddy stirring. Initially, these westerlies extend equatorward of 15°N/S and the surface pressure at 15°N/S drops, but then the Hadley circulation broadens as it strengthens and after day 25, the pressure is higher at 15°N/S than at the equator. Once an equatorial low forms, low level convergence develops and finally leads to the emergence of Hadley cells.

Therefore, the emergence of Hadley cell in rotating RCE starts with a quiescent atmosphere followed by eddy transport of zonal momentum, which sets up tropical easterlies and subtropical westerlies. The simultaneous geostrophic adjustment away from the equator results in a meridional gradient in the pressure field, which in turn promotes the formation of Hadley cells.

How strong is this eddy-driven Hadley cell compared with the Hadley circulation on Earth? To answer this question, I conducted a series of simulations with increasing equator-to-pole SST gradient. The SST field is set by the following expression:

$$\mathrm{SST} = 300 - \Delta T \frac{\cos(\varphi) - 1}{2}\,, \tag{5.11}$$

where ΔT in K is the temperature difference between the equator and the pole. I conducted simulations with $\Delta T = 2, 4, 8, 16\,\mathrm{K}$. The intensity of Hadley cells is measured by the max-

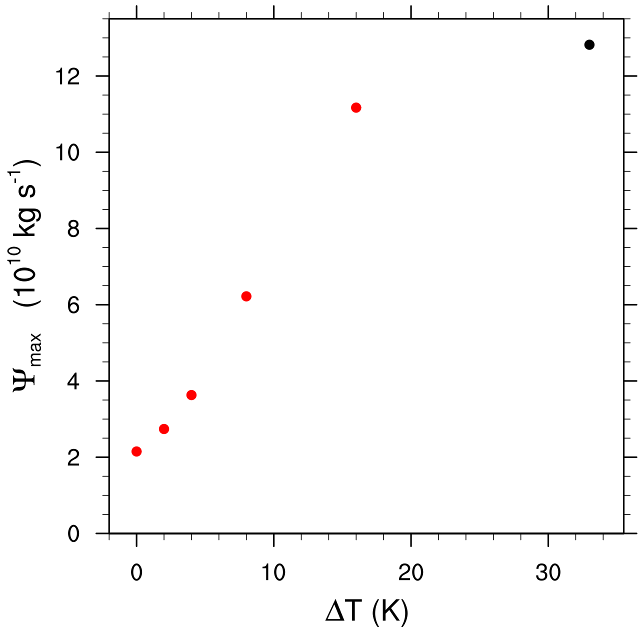

Figure 5.14: Hadley circulation intensity of simulations with different equator-to-pole temperature difference. The black dot indicates an aquaplanet simulation with observed zonal mean SST profile.

imum of the mass stream function (Ψ_{max}) of the zonally averaged flow between 30°S and 30°N. The calculation result is shown in Fig. 5.14, in which the result from an aquaplanet simulation with observed zonal mean SST profile is also compared.

As the equator-to-pole temperature difference increases, the Hadley cells become stronger and wider. The intensity of the Hadley circulation in rotating RCE is roughly 1/5 of its counterpart in the real world. Thus while the Hadley cells are generally weak, they are not weak enough to be neglected.

The simple angular momentum conserving model developed by Held and Hou (1980) is a special approximate idealized model of the Hadley circulation that ignores the effects of eddies. It predicts that the intensity of the Hadley circulation is proportional to $\Delta\theta^{5/2}$, where

$\Delta\theta$ is the change in vertically averaged potential temperature from pole to the equator. By comparing the simulations with $\Delta T = 2, 4, 8, 16\,\mathrm{K}$, which is roughly the same as $\Delta\theta$ in our simulations, I find that the intensity of Hadley circulations in Fig. 5.14 does not increase as fast as the Held and Hou model predicts. Furthermore, the Hadley circulation does not vanish when ΔT becomes zero. These discrepancies underscore the fundamental role of eddies in the formation of Hadley cells, consistent with what Walker and Schneider (2005) suggested in their study on the response of Hadley circulation to seasonally varying heating.

5.8 Conclusions

Building on simulations by Held and Zhao (2008) of RCE on a large doubly periodic f-plane, a slightly more complicated rotating RCE simulation on a sphere is achieved by prescribing globally uniform SST and eliminating incident solar radiation in a global atmospheric model. In this rotating RCE on a sphere, as in Held and Zhao's simulations, moist convection aggregates into a population of long-lived tropical cyclone-like vortices.

TCLVs are generated in the subtropical region, then move poleward and westward, due to the effect of beta drift. Many of those TCLVs can travel to high latitudes near the pole, in an average time of about two months. The mean spacing of mature TCLVs in the extratropics is approximately two times the deformation radius L_d.

The energy spectrum of atmosphere in rotating RCE is quite similar to that of the Earth's atmosphere, with a k^{-3} spectral slope at scales smaller than the deformation radius, and relatively flat spectrum at scale larger than the deformation radius. In both cases, these spectral features result from the concentration of APE production near the scale of the deformation radius, but the production mechanism in rotating RCE is the latent heating in the warm cores of the TCLVs, while on the real earth, it is baroclinic instability ultimately driven by equator-to-pole temperature differences.

An inspection of the temperature gradient between the warm cores of TCLVs and surrounding regions and the associated vertical wind shear suggests that baroclinic instability can break up TCLVs of size significantly larger than the deformation radius L_d. The combination of self-aggregation and baroclinic instability helps limit the spacing of TCLVs to about $2L_d$ in rotating RCE.

A weak eddy-driven Hadley circulation develops in our simulation of rotating RCE, similar to previous studies. Its strength is about 1/5 that of its real world counterpart. A Kelvin wave-like mode with wavenumber 1 and a period of 30 to 40 days is found at the equator.

The presence of a weak Hadley circulation and the beta drift of TCLVs enrich the dynamics of rotating RCE on a sphere, yet do not appear to increase the complexity in an overwhelming way. Such a rotating RCE simulation with spherical geometry, together with other variants of rotating RCE, may help us understand how the TCs simulated in GCMs depends upon environment parameters and parameterization schemes in an idealized manner, in addition to allowing us to understand the minimal set of factors needed to support related dynamical phenomena in the real atmosphere.

Bibliography

Allen, M., and W. Ingram, 2002: Constraints on future changes in climate and the hydrologic cycle. *Nature*, **419 (6903)**, 224–232, doi:10.1038/nature01092.

Ambaum, M. H. P., B. J. Hoskins, and D. B. Stephenson, 2001: Arctic Oscillation or North Atlantic Oscillation? *J. Climate*, **14 (16)**, 3495–3507, doi:10.1175/1520-0442(2001)014⟨3495:AOONAO⟩2.0.CO;2.

Attema, J. J., J. M. Loriaux, and G. Lenderink, 2014: Extreme precipitation response to climate perturbations in an atmospheric mesoscale model. *Environ. Res. Lett.*, **9 (1)**, 014 003, doi:10.1088/1748-9326/9/1/014003.

Augier, P., and E. Lindborg, 2013: A New Formulation of the Spectral Energy Budget of the Atmosphere, with Application to Two High-Resolution General Circulation Models. *J. Atmos. Sci.*, **70 (7)**, 2293–2308, doi:10.1175/JAS-D-12-0281.1.

Beniston, M., 2005: Mountain climates and climatic change: an overview of processes focusing on the european alps. *Pure Appl. Geophys.*, **162 (8)**, 1587–1606, doi:10.1007/s00024-005-2684-9.

Bretherton, C. S., P. N. Blossey, and M. Khairoutdinov, 2005: An Energy-Balance Analysis of Deep Convective Self-Aggregation above Uniform SST. *J. Atmos. Sci.*, **62 (12)**, 4273–4292, doi:10.1175/JAS3614.1.

Cannon, D. J., D. J. Kirshbaum, and S. L. Gray, 2011: Under what conditions does embedded convection enhance orographic precipitation? *Q.J.R. Meteorol. Soc.*, **138**, 391–406.

Chan, J. C. L., and R. T. Williams, 1987: Analytical and Numerical Studies of the Beta-Effect in Tropical Cyclone Motion. Part I: Zero Mean Flow. *J. Atmos. Sci.*, **44 (9)**, 1257–1265, doi:10.1175/1520-0469(1987)044⟨1257:AANSOT⟩2.0.CO;2.

Chang, S. W., R. J. Alliss, and S. Raman, 1993: SSM/I observations of ERICA IOP 4 marine cyclone: A comparison with in situ observations and model simulation. *Mon. Wea. Rev.*, **121**, 2452–2464.

Deser, C., R. Knutti, S. Solomon, and A. S. Phillips, 2012a: Communication of the role of natural variability in future North American climate. *Nat. Climate Change*, **2**, 775–780, doi:10.1038/nclimate1562.

Deser, C., A. Phillips, V. Bourdette, and H. Teng, 2012b: Uncertainty in climate change projections: the role of internal variability. *Climate Dyn.*, **38 (3-4)**, 527–546, doi:10.1007/s00382-010-0977-x.

Diffenbaugh, N. S., J. S. Pal, R. J. Trapp, and F. Giorgi, 2005: Fine-scale processes regulate the response of extreme events to global climate change. *Proc. Natl. Acad. Sci. USA*, **102 (44)**, 15 774–15 778, doi:10.1073/pnas.0506042102.

Dominguez, F., E. Rivera, D. Lettenmaier, and C. Castro, 2012: Changes in winter precipitation extremes for the western united states under a warmer climate as simulated by regional climate models. *Geophys. Res. Lett.*, **39 (5)**.

Durran, D. R., 1992: Two-layer solutions to Long's equation for vertically propagating mountain waves: wow good is linear theory? *Quart. J. Roy. Meteor. Soc.*, **118 (505)**, 415–433, doi:10.1002/qj.49711850502.

Emori, S., and S. Brown, 2005: Dynamic and thermodynamic changes in mean and extreme precipitation under changed climate. *Geophys. Res. Lett.*, **32**, L17 706, doi:10.1029/2005GL023272.

Frierson, F. M. W., 2006: Robust increases in midlatitude static stability in simulations of global warming. *Geophys. Res. Lett.*, **33 (24)**, L24 816, doi:10.1029/2006GL027504.

Gage, K. S., and G. D. Nastrom, 1986: Theoretical interpretation of atmospheric wavenumber spectra of wind and temperature observed by commercial aircraft during gasp. *J. Atmos. Sci.*, **43 (7)**, 729–740.

GFDL Global Atmospheric Model Development Team, 2004: The new GFDL global atmosphere and land model AM2–LM2: Evaluation with prescribed SST simulations. *J. Climate*, **17 (24)**, 4641–4673, doi:10.1175/JCLI-3223.1.

Gochis, D., and Coauthors, 2015: The great Colorado flood of September 2013. *Bull. Amer. Meteor. Soc.*, doi:10.1175/BAMS-D-13-00241.1.

Hamlet, A. F., and D. P. Lettenmaier, 2007: Effects of 20th century warming and climate variability on flood risk in the western U.S. *Water Resour. Res.*, **43**, W06 427, doi:10.1029/2006WR005099.

Hartmann, D. L., and K. Larson, 2002: An important constraint on tropical cloud - climate feedback. *Geophys. Res. Lett.*, **29 (20)**, 1951, doi:10.1029/2002GL015835.

Hawkins, E., and R. Sutton, 2012: Time of emergence of climate signals. *Geophys. Res. Lett.*, **39 (1)**, L01 702, doi:10.1029/2011GL050087.

Held, I. M., and A. Y. Hou, 1980: Nonlinear Axially Symmetric Circulations in a Nearly Inviscid Atmosphere. *J. Atmos. Sci.*, **37 (3)**, 515–533, doi:10.1175/1520-0469(1980)037⟨0515:NASCIA⟩2.0.CO;2.

Held, I. M., and B. Soden, 2006: Robust responses of the hydrological cycle to global warming. *J. Climate*, **19 (21)**, 5686–5699, doi:10.1175/JCLI3990.1.

Held, I. M., and M. Zhao, 2008: Horizontally homogeneous rotating radiative-convective equilibria at gcm resolution. *J. Atmos. Sci.*, **65 (6)**, 2003–2013, doi:10.1175/2007JAS2604.1.

Jiang, Q., 2003: Moist dynamics and orographic precipitation. *Tellus*, **55A**, 301–316.

Kay, J. E., and Coauthors, 2014: The Community Earth System Model (CESM) Large Ensemble Project: A Community Resource for Studying Climate Change in the Presence of Internal Climate Variability. *Bull. Amer. Meteor. Soc.*, doi:10.1175/BAMS-D-13-00255.1.

Khairoutdinov, M., and K. Emanuel, 2013: Rotating radiative-convective equilibrium simulated by a cloud-resolving model. *J. Adv. Model. Earth Syst.*, **5 (4)**, 816–825, doi:10.1002/2013MS000253.

Kharin, V. V., F. W. Zwiers, X. Zhang, and G. C. Hegerl, 2007: Changes in temperature and precipitation extremes in the IPCC ensemble of global coupled model simulations. *J. Climate*, **20 (8)**, doi:10.1175/JCLI4066.1.

Kirshbaum, D. J., and R. B. Smith, 2008: Temperature and moist-stability effects on midlatitude orographic precipitation. *Quart. J. Roy. Meteor. Soc.*, **134 (634)**, 1183–1199, doi:10.1002/qj.274.

Kirtman, B. P., and E. K. Schneider, 2000: A Spontaneously Generated Tropical Atmospheric General Circulation. *J. Atmos. Sci.*, **57 (13)**, 2080–2093, doi:10.1175/1520-0469(2000)057⟨2080:ASGTAG⟩2.0.CO;2.

Klemp, J. B., and D. R. Lilly, 1975: The dynamics of wave-induced downslope winds. *J. Atmos. Sci.*, **32 (2)**, 320–339, doi:10.1175/1520-0469(1975)032⟨0320:TDOWID⟩2.0.CO;2.

Kushner, P. J., I. M. Held, and T. L. Delworth, 2001: Southern Hemisphere Atmospheric Circulation Response to Global Warming. *J. Climate*, **14 (10)**, 2238–2249, doi:10.1175/1520-0442(2001)014⟨0001:SHACRT⟩2.0.CO;2.

Lavers, D. A., and G. Villarini, 2013: The nexus between atmospheric rivers and extreme precipitation across Europe. *Geophys. Res. Lett.*, **40 (12)**, 3259–3264, doi:10.1002/grl.50636.

Lavers, D. A., G. Villarini, R. P. Allan, E. F. Wood, and A. J. Wade, 2012: The detection of atmospheric rivers in atmospheric reanalyses and their links to British winter floods and the large-scale climatic circulation. *J. Geophys. Res.*, **117**, D20 106, doi:10.1029/2012JD018027.

Li, X., and B. Wang, 1994: Barotropic dynamics of the beta gyres and beta drift. *J. Atmos. Sci.*, **51 (5)**, 746–756.

Liepert, B., and M. Previdi, 2009: Do models and observations disagree on the rainfall response to global warming? *J. Climate*, **22 (11)**, 3156–3166, doi:10.1175/2008JCLI2472.1.

Lin, S.-J., 2004: A "vertically Lagrangian" finite-volume dynamical core for global models. *Mon. Wea. Rev.*, **132 (10)**, 2293–2307, doi:10.1175/1520-0493(2004)132⟨2293:AVLFDC⟩2.0.CO;2.

Lin, Y.-L., S. Chiao, T.-A. Wang, M. L. Kaplan, and R. P. Weglarz, 2001: Some common ingredients for heavy orographic rainfall. *Wea. Forecasting*, **16 (6)**, 633–660, doi:10.1175/1520-0434(2001)016⟨0633:SCIFHO⟩2.0.CO;2.

Loarie, S. R., P. B. Duffy, H. Hamilton, G. P. Asner, C. B. Field, and D. D. Ackerly, 2009: The velocity of climate change. *Nature*, **462 (7276)**, 1052–5, doi:10.1038/nature08649.

Lorenz, D. J., and D. L. Hartmann, 2001: Eddy-Zonal Flow Feedback in the Southern Hemisphere. *J. Atmos. Sci.*, **58 (21)**, 3312–3327, doi:10.1175/1520-0469(2001)058⟨3312:EZFFIT⟩2.0.CO;2.

Madden, R. A., and P. R. Julian, 1972: Description of Global-Scale Circulation Cells in the Tropics with a 40–50 Day Period. *J. Atmos. Sci.*, **29 (6)**, 1109–1123, doi:10.1175/1520-0469(1972)029⟨1109:DOGSCC⟩2.0.CO;2.

Madden, R. A., and P. R. Julian, 1994: Observations of the 40–50-Day Tropical Oscillation — A Review. *Mon. Wea. Rev.*, **122 (5)**, 814–837, doi:10.1175/1520-0493(1994)122⟨0814:OOTDTO⟩2.0.CO;2.

Maddox, R., L. Hoxit, C. Chappell, and F. Caracena, 1978: Comparison of meteorological aspects of the big thompson and rapid city flash floods. *Mon. Wea. Rev.*, **106**, 375–389, doi:10.1175/1520-0493(1978)106⟨0375:COMAOT⟩2.0.CO;2.

Manabe, S., and R. F. Strickler, 1964: Thermal Equilibrium of the Atmosphere with a Convective Adjustment. *J. Atmos. Sci.*, **21 (4)**, 361–385, doi:10.1175/1520-0469(1964)021⟨0361:TEOTAW⟩2.0.CO;2.

Marsaglia, G., W. W. Tsang, and J. Wang, 2003: Evaluating Kolmogorov's distribution. *J. Stat. Softw.*, **8 (18)**.

Miller, L. H., 1956: Table of percentage points of Kolmogorov statistics. *J. Am. Stat. Assoc.*, **51 (273)**, 111–121, doi:10.1080/01621459.1956.10501314.

Minder, J. R., D. R. Durran, and G. H. Roe, 2011: Mesoscale controls on the mountain-side snow line. *J. Atmos. Sci.*, **68**, 2107–2127, doi:10.1175/JAS-D-10-05006.1.

Moorthi, S., and M. J. Suarez, 1992: Relaxed arakawa-schubert. a parameterization of moist convection for general circulation models. *Monthly Weather Review*, **120 (6)**, 978–1002, doi:10.1175/1520-0493(2000)128⟨1070:ASFCOT⟩2.0.CO;2.

Muller, C. J., and I. M. Held, 2012: Detailed Investigation of the Self-Aggregation of Convection in Cloud-Resolving Simulations. *J. Atmos. Sci.*, **69 (8)**, 2551–2565, doi: 10.1175/JAS-D-11-0257.1.

Nolan, D. S., and E. D. Rappin, 2008: Increased sensitivity of tropical cyclogenesis to wind shear in higher sst environments. *Geophys. Res. Lett.*, **35 (14)**.

Nolan, D. S., E. D. Rappin, and K. A. Emanuel, 2007: Tropical cyclogenesis sensitivity to environmental parameters in radiative–convective equilibrium. *Quart. J. Roy. Meteor. Soc.*, **133 (629)**, 2085–2107.

O'Gorman, P., R. Allan, M. Byrne, and M. Previdi, 2012: Energetic constraints on precipitation under climate change. *Surv. Geophys.*, **33**, 585–608, doi:10.1007/s10712-011-9159-6.

O'Gorman, P. A., 2012: Sensitivity of tropical precipitation extremes to climate change. *Nature Geosci.*, **5 (10)**, 697–700, doi:10.1038/ngeo1568.

O'Gorman, P. A., and T. Schneider, 2009a: The physical basis for increases in precipitation extremes in simulations of 21st-century climate change. *Proc. Natl. Acad. Sci. USA*, **106 (35)**, 14 773–14 777, doi:10.1073/pnas.0907610106.

O'Gorman, P. A., and T. Schneider, 2009b: Scaling of precipitation extremes over a wide range of climates simulated with an idealized GCM. *J. Climate*, **22**, 5676–5685.

Pall, P., T. Aina, D. A. Stone, P. A. Stott, T. Nozawa, A. G. Hilberts, D. Lohmann, and M. R. Allen, 2011: Anthropogenic greenhouse gas contribution to flood risk in england and wales in autumn 2000. *Nature*, **470 (7334)**, 382–385.

Peterson, A. T., 2003: Projected climate change effects on Rocky Mountain and Great Plains birds: generalities of biodiversity consequences. *Global Change Biology*, **9 (5)**, 647–655, doi:10.1046/j.1365-2486.2003.00616.x.

Quadrelli, R., and J. M. Wallace, 2002: Dependence of the structure of the Northern Hemisphere annular mode on the polarity of ENSO. *Geophys. Res. Lett.*, **29 (23)**, 2132, doi: 10.1029/2002GL015807.

Rahmstorf, S., 2007: A semi-empirical approach to projecting future sea-level rise. *Science (New York, N.Y.)*, **315 (5810)**, 368–70, doi:10.1126/science.1135456.

Ralph, F. M., P. J. Neiman, G. A. Wick, S. I. Gutman, M. D. Dettinger, D. R. Cayan, and A. B. White, 2006: Flooding on california's russian river: Role of atmospheric rivers. *Geophys. Res. Lett.*, **33 (13)**, doi:10.1029/2006GL026689.

Rasmussen, K. L., and R. A. Houze, 2012: A flash-flooding storm at the steep edge of high terrain. *Bull. Amer. Meteor. Soc.*, **93 (11)**, 1713–1724, doi:10.1175/BAMS-D-11-00236.1.

Robe, F. R., and K. A. Emanuel, 1996: Moist Convective Scaling: Some Inferences from Three-Dimensional Cloud Ensemble Simulations. *J. Atmos. Sci.*, **53 (22)**, 3265–3275, doi:10.1175/1520-0469(1996)053⟨3265:MCSSIF⟩2.0.CO;2.

Robinson, W. A., 2000: A Baroclinic Mechanism for the Eddy Feedback on the Zonal Index. *J. Atmos. Sci.*, **57 (3)**, 415–422, doi:10.1175/1520-0469(2000)057⟨0415:ABMFTE⟩2.0.CO;2.

Romps, D. M., 2011: Response of Tropical Precipitation to Global Warming. *J. Atmos. Sci.*, **68 (1)**, 123–138, doi:10.1175/2010JAS3542.1.

Rotstayn, L. D., 1997: A physically based scheme for the treatment of stratiform clouds and precipitation in large-scale models. I: Description and evaluation of the microphysical processes. *Quart. J. Roy. Meteor. Soc.*, **123 (541)**, 1227–1282, doi:10.1002/qj.49712354106.

Rotstayn, L. D., B. F. Ryan, and J. J. Katzfey, 2000: A scheme for calculation of the liquid fraction in mixed-phase stratiform clouds in large-scale models. *Mon. Wea. Rev.*, **128 (4)**, 1070–1088, doi:10.1175/1520-0493(2000)128⟨1070:ASFCOT⟩2.0.CO;2.

Salmon, R., 1978: Two-layer quasi-geostrophic turbulence in a simple special case. *Geophys. Astrophys. Fluid Dyn.*, **10 (1)**, 25–52, doi:10.1080/03091927808242628.

Salmon, R., 1980: Baroclinic instability and geostrophic turbulence. *Geophys. Astrophys. Fluid Dyn.*, **15 (1)**, 167–211, doi:10.1080/03091928008241178.

Santer, B. D., and Coauthors, 2003: Contributions of anthropogenic and natural forcing to recent tropopause height changes. *Science*, **301 (5632)**, 479–83, doi:10.1126/science.1084123.

Schwartz, C. S., 2014: Reproducing the September 2013 Record-Breaking Rainfall over the Colorado Front Range with High-Resolution WRF Forecasts. *Wea. Forecasting*, **29 (2)**, 393–402, doi:10.1175/WAF-D-13-00136.1.

Shi, X., and D. Durran, 2015: Estimating the response of extreme precipitation over midlatitude mountains to global warming. *J. Climate*, **28**, 4246–4262.

Shi, X., and D. R. Durran, 2014: The response of orographic precipitation over idealized midlatitude mountains due to global increases in CO_2. *J. Climate*, **27 (11)**, 3938–3956, doi:10.1175/JCLI-D-13-00460.1.

Siler, N., and D. Durran, 2015: Assessing the impact of the tropopause on mountain waves and orographic precipitation using linear theory and numerical simulations. *J. Atmos. Sci.*, **72**, 803–820, doi:10.1175/JAS-D-14-0200.1.

Siler, N., and G. Roe, 2014: How will orographic precipitation respond to surface warming? An idealized thermodynamic perspective. *Geophys. Res. Lett.*, **41 (7)**, 2606–2613, doi:10.1002/2013GL059095.

Simmons, A. J., J. M. Wallace, and G. W. Branstator, 1983: Barotropic Wave Propagation and Instability, and Atmospheric Teleconnection Patterns. *J. Atmos. Sci.*, **40 (6)**, 1363–1392, doi:10.1175/1520-0469(1983)040⟨1363:BWPAIA⟩2.0.CO;2.

Singh, D., M. Tsiang, B. Rajaratnam, and N. S. Diffenbaugh, 2013: Precipitation extremes over the continental united states in a transient, high-resolution, ensemble climate model experiment. *J. Geophys. Res.*, **118 (13)**, 7063–7086, doi:10.1002/jgrd.50543.

Singh, M. S., and P. A. O'Gorman, 2014: Influence of microphysics on the scaling of precipitation extremes with temperature. *Geophys. Res. Lett.*, **41 (16)**, 6037–6044, doi: 10.1002/2014GL061222.

Skamarock, W. C., and Coauthors, 2008: *A description of the Advanced Research WRF version 3*. NCAR Tech. Note NCAR/TN-475+STR, 113 pp.

Sumi, A., 1992: Pattern Formation of Convective Activity over the Aqua-planet with Globally Uniform Sea Surface Temperature (SST). *J. Meteor. Soc. Japan*, **70 (5)**, 855–876.

Takahashi, K., 2009: Radiative constraints on the hydrological cycle in an idealized radiative-convective equilibrium model. *J. Atmos. Sci.*, **66 (1)**, 77–91, doi:10.1175/2008JAS2797.1.

Thompson, D. W., and J. M. Wallace, 2001: Regional climate impacts of the Northern Hemisphere annular mode. *Science*, **293 (5527)**, 85–9, doi:10.1126/science.1058958.

Tompkins, A. M., and G. C. Craig, 1998: Radiative-convective equilibrium in a three-dimensional cloud-ensemble model. *Quart. J. Roy. Meteor. Soc.*, **124 (550)**, 2073–2097, doi:10.1002/qj.49712455013.

Vallis, G. K., 2006: *Atmospheric and oceanic fluid dynamics: fundamentals and large-scale circulation*. Cambridge University Press, 247–287 pp.

Vallis, G. K., P. Zurita-Gotor, C. Cairns, and J. Kidston, 2014: Response of the large-scale structure of the atmosphere to global warming. *Quart. J. Roy. Meteor. Soc.*, doi: 10.1002/qj.2456.

Walker, C. C., and T. Schneider, 2005: Response of idealized hadley circulations to seasonally varying heating. *Geophys. Res. Lett.*, **32 (6)**, L06 813, doi:10.1029/2004GL022304, URL http://dx.doi.org/10.1029/2004GL022304.

Wallace, J. M., 2000: North atlantic oscillatiodannular mode: Two paradigms-one phenomenon. *Quart. J. Roy. Meteor. Soc.*, **126 (564)**, 791–805, doi:10.1002/qj.49712656402.

Wallace, J. M., Q. Fu, B. V. Smoliak, P. Lin, and C. M. Johanson, 2012: Simulated versus observed patterns of warming over the extratropical Northern Hemisphere continents during the cold season. *Proc. Natl. Acad. Sci. USA*, **109 (36)**, 14 337–14 342, doi:10.1073/pnas.1204875109.

Wallace, J. M., and D. W. J. Thompson, 2002: The Pacific Center of Action of the Northern Hemisphere Annular Mode: Real or Artifact? *J. Climate*, **15 (14)**, 1987–1991, doi:10.1175/1520-0442(2002)015⟨1987:TPCOAO⟩2.0.CO;2.

Wang, B., and X. Li, 1992: The beta drift of three-dimensional vortices: A numerical study. *Mon. Wea. Rev.*, **120**, 579–593.

Wang, Y., and G. Holland, 1996: The beta drift of baroclinic vortices. Part I: Adiabatic vortices. *J. Atmos. Sci.*, **53 (3)**, 411–427.

Warner, M. D., C. F. Mass, and E. P. S. Jr., 2012: Wintertime Extreme Precipitation Events along the Pacific Northwest Coast: Climatology and Synoptic Evolution. *Mon. Wea. Rev.*, **140 (7)**, 2021–2043, doi:10.1175/MWR-D-11-00197.1.

Wehner, M. F., 2013: Very extreme seasonal precipitation in the narccap ensemble: model performance and projections. *Climate Dyn.*, **40 (1-2)**, 59–80, doi:10.1007/s00382-012-1393-1.

Wheeler, M., and G. N. Kiladis, 1999: Convectively Coupled Equatorial Waves: Analysis of Clouds and Temperature in the Wavenumber-Frequency Domain. *J. Atmos. Sci.*, **56 (3)**, 374–399, doi:10.1175/1520-0469(1999)056⟨0374:CCEWAO⟩2.0.CO;2.

White, A. B., D. J. Gottas, E. T. Strem, F. M. Ralph, and P. J. Neiman, 2002: An automated brightband height detection algorithm for use with doppler radar spectral moments. *J. Atmos. Oceanic Technol.*, **19**, 687–697.

Willison, J., W. A. Robinson, and G. M. Lackmann, 2013: The importance of resolving mesoscale latent heating in the North Atlantic storm track. *J. Atmos. Sci.*, **70 (7)**, 2234–2250, doi:10.1175/JAS-D-12-0226.1.

Yin, J. H., 2005: A consistent poleward shift of the storm tracks in simulations of 21st century climate. *Geophys. Res. Lett.*, **32 (18)**, L18 701, doi:10.1029/2005GL023684.

Zhao, M., I. M. Held, S.-J. Lin, and G. A. Vecchi, 2009: Simulations of global hurricane climatology, interannual variability, and response to global warming using a 50-km resolution GCM. *J. Climate*, **22 (24)**, 6653–6678, doi:10.1175/2009JCLI3049.1.

Zhou, W., I. M. Held, and S. T. Garner, 2013: Parameter study of tropical cyclones in rotating radiative-convective equilibrium with column physics and resolution of a 25 km GCM. *J. Atmos. Sci.*, doi:10.1175/JAS-D-13-0190.1, in press.

Zhu, Y., and R. E. Newell, 1994: Atmospheric rivers and bombs. *Geophys. Res. Lett.*, **21 (18)**, 1999–2002, doi:10.1029/94GL01710.

Zurita-Gotor, P., and G. K. Vallis, 2009: Equilibration of Baroclinic Turbulence in Primitive Equations and Quasigeostrophic Models. *J. Atmos. Sci.*, **66 (4)**, 837–863, doi:10.1175/2008JAS2848.1.

Vita

Xiaoming Shi was born in the Shanxi Province of China, in 1986. The name Shanxi means "West of the Mountains", a reference to the province's location west of the Taihang Mountains. He earned a bachelor's degree in Atmospheric Sciences from the Lanzhou University (LZU) in China, in 2009. After staying in the graduate school of LZU for a short period, he decided to take an adventure oversea. In 2010, he came to the fabulous city Seattle to pursue a PhD degree in Atmospheric Sciences. He was married to Ruixue Yin at Lanzhou in 2010, and their lovely daughter, Isabella Zihan Shi, was born at Seattle, in 2013. Ironically, after happily living in Seattle for five years, his motherland occasionally appears foreign to him.